

**Spectroscopic study  
on forbidden magnetic dipole transitions  
in LHD**

**Ryuji Katai**

**Doctor of Science**

**Department of Fusion Science  
School of Physical Science  
The Graduate University for Advanced Studies**

**2006 School year**

## Abstract

Forbidden lines arising from magnetic dipole (M1) transitions among fine-structure levels of highly charged ions have been observed for Al, Ar, Ti, Fe, Kr, Mo and Xe in Large Helical Device (LHD). A space-resolved 3m normal incidence VUV spectrometer and newly designed double-structure impurity pellets for an impurity pellet injector have been developed for this purpose. The M1 transitions are identified by analyzing their Doppler broadening, temporal intensity behavior and spatial intensity distribution. Wavelengths of these M1 transitions are determined with high accuracy and compared with previous experimental and calculated values with detailed spectroscopic analysis of C, Ne and Ar emission lines in range of 250 to 2300Å. The M1 transitions from heavy elements observed here are expected to be useful for visible impurity diagnostics of D-T burning plasmas in the future.

The line intensity ratios of the M1 transition to the allowed (E1) transition such as  $2s^2 2p^5 \ ^2P_{3/2} - ^2P_{1/2} / 2s^2 2p^5 \ ^2P_{3/2} - 2s2p^6 \ ^2S_{1/2}$  (ArX 5533Å/165Å, TiXIV 2118Å/122Å and FeXVIII 975Å/94Å) and  $2s2p \ ^3P_1 - ^3P_2 / 2s^2 \ ^1S_0 - 2s2p \ ^1P_1$  (ArXV 5944Å/221Å) are measured as a function of electron density. Results on the ArX and ArXV are compared with a simple level-population calculation. As a result, the density dependence of the ratio is well explained mainly by a competition between two decay processes of the collisional de-excitation and the radiative decay due to the forbidden line emission. The effect of fast ions on the M1 transition is also considered.

# Contents

<b>1. Introduction</b> .....	1
1.1. Importance of impurity study in controlled thermonuclear fusion research .....	1
1.2. Transition probability and selection rules for allowed and forbidden transitions .....	2
1.3. History of forbidden lines study .....	5
1.4. Application of magnetic forbidden dipole transitions to plasma diagnostics .....	8
References .....	10
<b>2. Experimental setup</b> .....	12
2.1. 3m normal incidence spectrometer .....	12
2.1.1. Introduction .....	12
2.1.2. Space-resolved 3m VUV spectrometer .....	13
2.1.3. Radial profile measurement .....	16
2.1.4. Summary .....	22
2.2. Heavy element impurity pellet injection .....	25
References .....	32
<b>3. Observation of spectra</b> .....	34
3.1. High-resolution VUV spectra of carbon, neon and argon .....	34
3.1.1. Introduction .....	34
3.1.2. Line identification of C, Ne and Ar .....	36
3.1.3. Ion temperature from Doppler broadening .....	37
3.1.4. Line profile analysis of absorption spectra .....	39
3.1.5. Summary .....	44
3.2. Identification of M1 lines of Al, Ar, Ti and Fe .....	71
3.2.1. Introduction .....	71
3.2.2. Instrumentation .....	72
3.2.3. Identification of M1 transitions .....	73
3.2.4. Summary .....	78
3.3. M1 lines of high-Z elements (Kr, Mo and Xe) .....	82
3.3.1. Introduction .....	82
3.3.2. Experimental setup .....	83
3.3.3. Results and discussion .....	84
3.3.4. Summary .....	88
References .....	90
<b>4. Intensity analysis on M1 transitions</b> .....	95
4.1. Introduction .....	95
4.2. Analysis of line intensity ratios .....	97
4.3. Line ratio of F-like ions (ArX, TiXIV and FeXVIII) .....	99
4.4. Line ratio of Be-like ion (ArXV) .....	109
4.5. Summary .....	112

References .....	115
<b>5. Summary and conclusions .....</b>	<b>116</b>
Acknowledgements .....	120
List of publications .....	121

## List of figures

1.1	Z dependence of wavelength for F-like E1, F-like, Si-like, Ti-like M1 transitions .....	7
1.2	Z dependence of transition probability for E1 and M1 transitions .....	7
2.1	Schematic view of space-resolved 3m VUV spectrometer system in LHD .....	14
2.2	Optics of space-resolved VUV spectroscopy and Pt-coated mirror arrangement .....	15
2.3	Schematic drawing of magnetic surfaces, external form of ergodic layer and so on .....	16
2.4	Full vertical profiles of impurity emissions .....	18
2.5	Radial profiles of CIV 1548Å emissions .....	19
2.6	Time development of carbon vertical profiles .....	23
2.7	Vertical profile of CIV emission and ion temperature .....	24
2.8	Cylindrical carbon pellet with tin (Sn) coating .....	26
2.9	Co-axial impurity pellet inserted tungsten (W) wire into polystyrene tube .....	26
2.10	Amount of heavy element for three kind of impurity pellets .....	27
2.11	Velocities of impurity pellets shot with 15atm helium gas .....	28
2.12	Temporal behaviors of the electron density and temperature for pellet injections .....	29
2.13	Temporal behavior with cylindrical Sn-coated carbon pellet .....	30
2.14	Temporal behavior with Mo-inserted co-axial impurity pellet .....	31
3.1-1 to 1-7	VUV spectra from neon discharges .....	55-61
3.2-1 to 2-9	VUV spectra from argon discharges .....	62-70
3.3	Ionization potential of carbon, neon and argon ions .....	38
3.4	Ion temperature evaluated from Doppler broadening of neon and argon lines .....	39
3.5	Spectral profiles of CIV and CV with Doppler broadening .....	40
3.6	Line profiles of hydrogen Lyman- $\alpha$ with self-absorption .....	43
3.7	Line profile of hydrogen Lyman- $\beta$ with self-absorption .....	44
3.8	Partial energy level diagram of M1 and E2 transitions .....	73
3.9	VUV spectra from argon plasmas measured with 3m normal incidence spectrometer .....	74
3.10	Spectral profiles of ArVII, ArXII and ArXVI .....	75
3.11	Visible and EUV spectra from argon plasmas .....	77

3.12	VUV spectra from impurity pellet injected plasmas .....	79
3.13	Z dependence of wavelength for Si- and Ti-like M1 transitions .....	82
3.14	Spectrum with KrXXII M1 transition .....	84
3.15	Spectrum with KrXXIII M1 transition .....	86
3.16	Spectrum with MoXXIX M1 transition .....	87
3.17	Spectrum with XeXXXIII M1 transition .....	87
4.1	Temporal behaviors of intensity of argon .....	96
4.2	Calculated electron and proton impact excitation cross sections .....	98
4.3	Vertical distributions of line-integrated argon emissions .....	99
4.4	Partial energy diagram of ArX .....	100
4.5	Electron density dependence of line ratios on F-like ions .....	103
4.6	Ion temperature dependence of line ratios on F-like ions .....	104
4.7	Line ratios of ArX M1/E1 as a function of electron density .....	105
4.8	Line ratios (M1/E1) of F-like ions with fast proton impact excitation .....	106
4.9	Experimental results of line ratios for TiXIV and FeXVIII .....	108
4.10	Partial energy diagram of ArXV .....	109
4.11	Line ratios of ArXV M1/E1 as a function of electron density .....	111

## List of tables

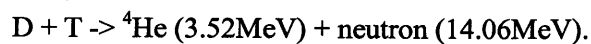
1.1	Selection rules for E1, M1 and E2 transitions .....	5
3.1	Wavelength list of carbon lines .....	45-47
3.2	Wavelength list of neon lines .....	48-50
3.3	Wavelength list of argon lines .....	51-53
3.4	Line lists of carbon, neon and argon lines useful to spectroscopy .....	54
3.5	Wavelength of Ar M1 transitions determined from the present work .....	80
3.6	Wavelength of M1 transitions of Al, Ti and Fe .....	81
3.7	M1 transitions of heavy impurity elements .....	89
4.1	Atomic data of F I isoelectronic sequence ArX, TiXIV and FeXVIII .....	113
4.2	Atomic data of Be I isoelectronic sequence ArXV .....	114

# Chapter 1

## Introduction

### 1.1. Importance of impurity study in controlled thermonuclear fusion research

Fusion reaction between hydrogen isotopes of D and T is expected as the most promising nuclear reaction for alternative electric power source in order to overcome the present encountered energy problems;



In order to realize the fusion reactor a high-temperature and high-density plasma ( $>10\text{keV}$ ) has to be confined for a certain time. The plasma has to be sustained by the  $\alpha$  ( ${}^4\text{He}$ ) heating with satisfying the following condition;

$$n_i T \tau_E > 3 \times 10^{21} \text{ m}^{-3} \text{keVs},$$

where  $n_i$  and  $T$  are the ion density and plasma temperature, and  $\tau_E$  is the energy confinement time expressed as follows;

$$\tau_E = W_p / P_{in},$$

where  $W_p$  is the plasma stored energy and  $P_{in}$  the heating power.

High-temperature fusion plasmas are contaminated by impurities such as carbon, oxygen and metallic elements, because of the existence of plasma facing components. When the impurities exist in the plasma, it gives rise to the increase in the radiation loss in addition to a dilution of the fuel ions. The net input power,  $P_{in\_net}$ , is reduced by the radiation loss as

$$P_{in\_net} = P_{in} - P_{rad}.$$

Then, the impurity control becomes an important issue for realizing the fusion reactor. Especially, the control of heavy impurity elements is essentially required, since the radiation loss from the impurity is much bigger when the nuclear number increases. The radiation loss from a specific impurity element is expressed by

$$P_{rad} = n_e n_{imp} R,$$

where  $R$  is the radiation coefficient as a function of electron temperature. The radiation loss is the sum of line emissions from impurities if the bremsstrahlung is ignored. Thus, it becomes very important to measure the line emission from impurities for the purpose of impurity control in fusion plasmas.

## 1.2. Transition probability and selection rules for allowed and forbidden transitions

The time-dependent Schrödinger equation is written as

$$i\hbar \frac{\partial \Psi}{\partial t} = [H_0 + H'(t)]\Psi, \quad (1.1)$$

where  $H_0$  is the time-independent Hamiltonian in the absence of external fields and

$$H'(t) = -\frac{i\hbar e}{m} \mathbf{A} \cdot \nabla + \frac{e^2}{2m} \mathbf{A}^2, \quad (1.2)$$

is a perturbation of electromagnetic field which explicitly depends on the time through the vector potential  $\mathbf{A}$ . Here, we drop the term of  $\mathbf{A}^2$  in the weak field case, in the following discussions [1].

Using the time-independent eigenfunctions  $\psi_k$  and eigenvalues  $E_k$ , the solution of the time-dependent unperturbed Schrödinger equation

$$i\hbar \frac{\partial \Psi_k}{\partial t} = H_0 \Psi_k, \quad (1.3)$$

can be expressed as

$$\Psi_k = \psi_k(\mathbf{r}) \exp(-iE_k t / \hbar), \quad (1.4)$$

The general solution,  $\Psi$ , of the time-dependent Schrödinger equation eq.(1.1) can be expanded as

$$\Psi = \sum_k c_k(t) \Psi_k(\mathbf{r}, t) = \sum_k c_k(t) \psi_k(\mathbf{r}) \exp(-iE_k t / \hbar), \quad (1.5)$$

where the sum is over the complete set of eigenfunctions,  $\psi_k$ .

The coefficient  $c_k(t)$  of the first order in the perturbation  $H'$  is known to be expressed as

$$c_b^{(1)}(t) = -\frac{e}{m} \int_0^t \langle \psi_b | \mathbf{A} \cdot \nabla | \psi_a \rangle \exp(i\omega_{ba} t') dt', \quad (1.6)$$

where  $a$  and  $b$  stand for the initial and final states of the transition and  $\omega_{ba} = (E_b - E_a) / \hbar$ .

Here, we introduce the classical vector potential of

$$\mathbf{A}(\mathbf{r}, t) = \int_{\Delta\omega} A_0(\omega) \hat{\mathbf{e}} \{ \exp(i\mathbf{k} \cdot \mathbf{r} - i\omega t) + \exp(-i\mathbf{k} \cdot \mathbf{r} + i\omega t) \} d\omega, \quad (1.7)$$

where  $\hat{\mathbf{e}}$  is the unit vector for polarization of radiation and  $\mathbf{k}$  is the propagation vector of radiation. Eq.(1.7) is substituted for eq.(1.6) as follows;

$$c_b^{(1)}(t) = -\frac{e}{m} \int_{\Delta\omega} d\omega A_0(\omega) \left[ \langle \psi_b | \exp(i\mathbf{k} \cdot \mathbf{r}) \hat{\mathbf{e}} \cdot \nabla | \psi_a \rangle \int_0^t \exp(i\omega_{ba} t' - i\omega t') dt' \right. \\ \left. + \langle \psi_b | \exp(-i\mathbf{k} \cdot \mathbf{r}) \hat{\mathbf{e}} \cdot \nabla | \psi_a \rangle \int_0^t \exp(i\omega_{ba} t' + i\omega t') dt' \right], \quad (1.8)$$

When the duration of the pulse  $t$  is much larger than the periodic time  $2\pi/\omega_{ba}$ , the integral

over  $t'$  in eq.(1.8) will be negligible. The first integral over  $t'$  in eq.(1.8) will be not negligible if  $\omega_{ba} \approx \omega$  (when  $E_b > E_a$ ,  $\omega_{ba} > 0$  and  $E_b \approx E_a + \hbar\omega_{ba}$ ). In this case the final state of the atom has greater energy than the initial state and one photon of energy  $\hbar\omega$  has been absorbed from the radiation. On the other hand, the second integral over  $t'$  in eq.(1.8) will be not negligible if  $\omega_{ba} \approx -\omega$  (when  $E_b < E_a$ ,  $\omega_{ba} < 0$  and  $E_b \approx E_a - \hbar\omega_{ba}$ ). In this case the initial state of the atom has greater energy than the final state and one photon of energy  $\hbar\omega$  is emitted by de-excitation.

We start with the first term eq.(1.8), describing absorption. We obtain

$$|c_b^{(1)}(t)|^2 = 2\pi \left[ \frac{eA_0(\omega_{ba})}{m} \right]^2 |\langle \psi_b | \exp(i\mathbf{k} \cdot \mathbf{r}) \hat{\mathbf{e}} \cdot \nabla | \psi_a \rangle|^2 t, \quad (1.9).$$

Thus the probability  $|c_b(t)|^2$  increases linearly with time and a *transition probability* for absorption  $W_{ba}$  can be defined as

$$W_{ba} = \frac{d}{dt} |c_b^{(1)}(t)|^2 = 2\pi \left[ \frac{eA_0(\omega_{ba})}{m} \right]^2 |\langle \psi_b | \exp(i\mathbf{k} \cdot \mathbf{r}) \hat{\mathbf{e}} \cdot \nabla | \psi_a \rangle|^2, \quad (1.10)$$

and the transition rate for stimulated emission  $W_{ab}$  is given by

$$W_{ab} = W_{ba}, \quad (1.11).$$

We need quantum electrodynamics to explain the spontaneous emission. Therefore, we note only the result of the spontaneous emission of a photon  $W_{ab}^s$ , is given by

$$W_{ab}^s = \frac{4\pi^2}{m^2} \left( \frac{e^2}{4\pi\epsilon_0} \right) \frac{\hbar}{V\omega_{ba}} |\langle \psi_b | \exp(i\mathbf{k} \cdot \mathbf{r}) \hat{\mathbf{e}} \cdot \nabla | \psi_a \rangle|^2 \delta(\omega - \omega_{ba}), \quad (1.12).$$

The matrix element defined as  $\langle \psi_b | \exp(i\mathbf{k} \cdot \mathbf{r}) \hat{\mathbf{e}} \cdot \nabla | \psi_a \rangle$  can be simplified by expanding the exponential  $\exp(i\mathbf{k} \cdot \mathbf{r})$  as

$$\exp(i\mathbf{k} \cdot \mathbf{r}) = 1 + (i\mathbf{k} \cdot \mathbf{r}) + \frac{1}{2!} (i\mathbf{k} \cdot \mathbf{r})^2 + \dots, \quad (1.13).$$

If the quantity  $(kr)$  is small ( $k=2\pi/\lambda_{ab}$ , the  $\lambda_{ab}$  ranges 4000-8000Å in visible and the distance from nucleus  $r < 10\text{Å}$  in general atom), we can replace  $\exp(i\mathbf{k} \cdot \mathbf{r})$  by unity in eq. (1.10) and (1.12). This is known as the electronic dipole (allowed, E1) transitions. When the transition is forbidden, higher terms in the series (1.13), which correspond to magnetic dipole (M1), electric quadrupole (E2) transitions, may not be vanished, although the

transition rate is generally much smaller than for allowed transitions. In general, the magnetic interaction is smaller than the electronic interaction in the fine structure constant, 137. Exact understanding of such higher terms in eq.(1.13) is very important to establish a complete atomic structure model for all elements, especially for heavy elements. Thus, the study of the M1 transition in heavy elements becomes also important and can give valuable information to build a complete set of the atomic structure calculation.

The electron transitions which are not E1 transitions are called 'forbidden transitions'. The kind of the transitions is distinguished by selection rules. The selection rules for E1 (allowed, electronic dipole), M1 (forbidden, magnetic dipole) and E2 (forbidden, electronic quadrupole) transitions are listed in Table 1.1.

**Table 1.1** Selection rules of E1, M1 and E2 transitions

Transition	E1	M1	E2
with negligible configuration interaction (like hydrogen)	One electron jumping with; $\Delta n$ arbitrary, $\Delta \ell = \pm 1$	in the same configuration; $\Delta n = 0$ , $\Delta \ell = 0$	jumping or in the same; $\Delta n$ arbitrary, $\Delta \ell = 0, \pm 2$
$\Delta S$ for LS coupling only	0	0	0
$\Delta L$ for LS coupling only	0, $\pm 1$ (except $L=0 \leftrightarrow 0$ )	0, with $\Delta J = \pm 1$	0, $\pm 1, \pm 2$ (except $L=0 \leftrightarrow 0$ , $0 \leftrightarrow 1$ )
$\Delta J$	0, $\pm 1$ (except $J=0 \leftrightarrow 0$ )	0, $\pm 1$ (except $J=0 \leftrightarrow 0$ )	0, $\pm 1, \pm 2$ (except $J=0 \leftrightarrow 0$ , $1/2 \leftrightarrow 1/2, 0 \leftrightarrow 1$ )
$\Delta M$	0, $\pm 1$ (except $J=0 \leftrightarrow 0$ when $\Delta J = 0$ )	0, $\pm 1$ (except $J=0 \leftrightarrow 0$ when $\Delta J = 0$ )	0, $\pm 1, \pm 2$
Parity	Change (even $\leftrightarrow$ odd)	No change	No change

### 1.3. History of forbidden lines study

Line emissions from highly charged ions present important materials for studies in laboratory and astrophysical plasmas [2-4]. For the purpose resonance lines from such highly charged ions are generally used because of the high brightness, and those exist in the X-ray and VUV regions. On the other hand, forbidden transitions from highly charged ions frequently appear in the visible range (see Fig.1.1). Compared to conventional X-ray and VUV techniques, standard optical methods offer several advantage such as higher spectral resolution and easy access to spatial resolution, larger solid angles for visible light collection and existence of several detectors. For astrophysics, the visible spectroscopy becomes more important, i.e., low absorption by the interstellar medium and long-distance accessibility for observation of stellar objects.

Earth-based telescopes can be used to detect the visible radiation from highly charged ions without the need of space-based instruments in the X-ray and EUV-VUV regions. In 1927, Bowen first identified the forbidden line in several prominent lines from galactic nebulae spectra as transitions between levels belonging to the normal configurations of various atoms and ions, e.g. NII 6584Å and OIII 4959, 5007Å [5]. However, those had previously been conjectured as transitions in an extraterrestrial element, *nebulium* in 1864. Forbidden optical transitions from highly charged ions had been detected in the Sun before X-rays measurements were performed. So-called coronal visible lines thus gave the first evidence for the presence of such highly charged ions in the Sun. A well-known example is the FeXIV forbidden lines at 5303Å in 1939 as the first observation of this strong line in the solar corona. In 1869, however, those had been also conjectured as an extraterrestrial element, *coronium* [6].

Forbidden lines arising from magnetic dipole (M1) transitions in highly charged ions have been thus observed not only in astrophysical sources, but also in magnetically confined plasmas and in electron beam ion trap (EBIT) [7, 13]. In the fusion plasmas the M1 transitions from highly charged iron was observed in PLT tokamak by Hinnov et al., for the first time [14]. After that the M1 transitions have been observed in tokamaks [8, 15-28].

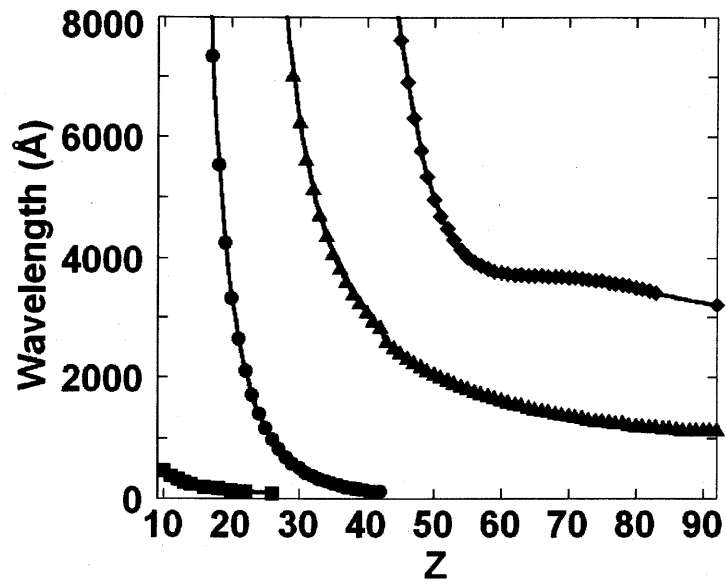


**Fig. 1.1** Z dependence of wavelengths for F-like E1 ( $2s^2 2p^5 \ ^2P_{3/2} - 2s 2p^6 \ ^2S_{1/2}$ : solid squares) [7], F-like ( $2s^2 2p^5 \ ^2P_{3/2} - ^2P_{1/2}$ : solid circles) [8], Si-like ( $3s^2 3p^2 \ ^3P_1 - ^3P_2$ : solid triangles) [8, 9] and Ti-like ( $3d^4 \ ^5D_3 - ^5D_2$ : solid diamonds) [10-12] M1 transitions.

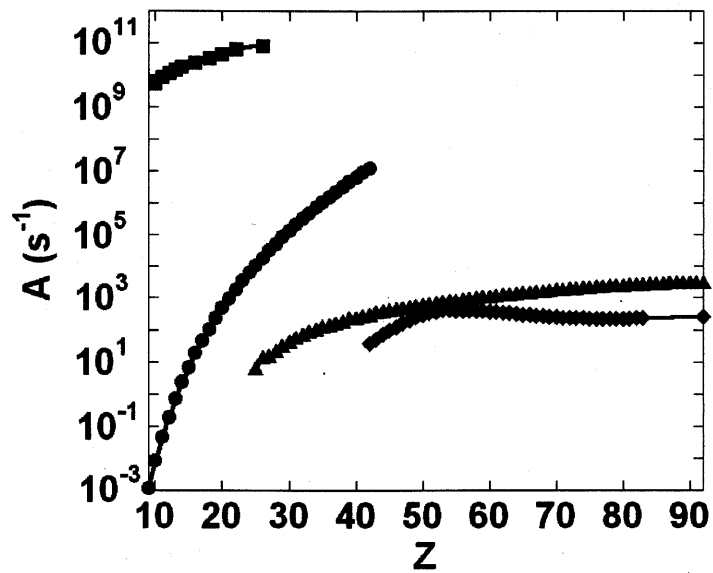


**Fig.1.2** Z dependence of transition probability for F-like E1 (solid squares) [7], F-like (solid circles) [8], Si-like (solid triangles) [8, 9] and Ti-like (solid diamonds) [10-12] M1 transitions.

Morgan et al., identified experimentally some predicted lines [10] in Ti-like ion XeXXXIII ( $\text{Xe}^{32+}$ ) from the EBIT at the National Institute of Science and Technology (NIST) in 1995 [29]. They showed for the first time the possibilities of the EBIT for the study of visible transitions from ions in extremely high charge states. The study of the M1 transitions have been energetically continued also in EBIT up to this day [11, 12] (see section 3.3.1).

#### **1.4. Application of magnetic forbidden dipole transitions to plasma diagnostics**

Wavelengths of spectral lines from impurities in fusion plasmas move from visible range to VUV or x-ray range when the ionization stage of the impurity increases. Therefore, the x-ray line emission is mainly dominant in the central column of the high-temperature fusion plasmas. The visible spectroscopy has been limited to the plasma edge diagnostics if charge exchange spectroscopy is excluded. On the other hand, the M1 line has a transition among the ground state of highly charged impurity ions. The wavelength of the M1 transition moves toward longer wavelength side as compared to allowed lines (E1) usually measured in EUV and x-ray ranges, and then, the M1 transition is mainly emitted in the visible range (see Fig.1.1). The transition probability of the M1 transition is quickly increases with nuclear number as shown in Fig.1.2. Therefore, the M1 transition becomes very bright for high-Z elements.

The high-Z elements such as Ne, Ar, Kr, Xe, Mo and W recently become important in fusion research. In the next-generation fusion device the element of Mo or W is a candidate of the plasma facing material [30]. The elements of Ar and Kr are planned for diagnostic use and the elements of Ne and Ar are used for divertor cooling. The impurity spectroscopy of such high-Z elements is thus important in the next-generation fusion device. The VUV and EUV spectroscopy usually used for the impurity diagnostics requires the vacuum and the instruments have to be directly connected to the fusion device. If the D-T operation is carried out, the grating and detector will be damaged by the neutrons and the

detector itself will be influenced by the tritium. Therefore, if the line emissions from the high-Z elements are measured in the visible range using optical fibers, the difficulty of the impurity spectroscopy in burning plasmas can be much reduced. The M1 transition is a possible candidate to overcome the present situation of the VUV spectroscopy in the next-generation fusion device. The search of the M1 transitions from such heavy elements for plasma diagnostics is one of the motivation of this thesis in addition to spectroscopic study on the M1 transition and VUV line emissions and contribution to atomic physics.

## References

- [1] B. H. Bransden and C. J. Joachain, *Physics of atoms and molecules*, Longman 1983.
- [2] R. C. Isler, *Nucl. Fusion* **24**, 1599-1678 (1984).
- [3] C. De Michelis and M. Mattioli, *Rep. Prog. Phys.* **47**, 1233-1346 (1984).
- [4] B. Denne and E. Hinnov, *Phys. Scr.* **35**, 811-818 (1987).
- [5] I. S. Bowen, *Nature (London)* **120** (1927).
- [6] B. Edlén, *Arkiv. Matem. Astr. och Fys.* **28**, B No.1 (1941).
- [7] K. T. Cheng and Y.-K. Kim, *At. Data Nucl. Data. Tables* **24**, 111-189 (1979).
- [8] V. Kaufman and J. Sugar, *J. Phys. Chem. Ref. Data* **15**, 321-387 (1986).
- [9] K.-N. Huang, *At. Data Nucl. Data. Tables* **32**, 503-566 (1985).
- [10] U. Feldman, P. Indelicato and J. Sugar, *J. Opt. Soc. Am. B* **8**, 3-5 (1991).
- [11] E. Biemont, E Träbert and C. J. Zeippen, *J. Phys. B* **34**, 1941-1951 (2001).
- [12] S. B. Utter, P. Beiersdorfer and E Träbert, *Phys. Rev. A* **67**, 012508-1-5 (2003).
- [13] M. H. Prior, *J. Opt. Soc. Am. B* **4**, 144-147 (1987).
- [14] S. Suckewer and E. Hinnov, *Phys. Rev. Lett.* **41**, 756-759 (1978).
- [15] S. Suckewer, H. P. Eubank, *et al*, *Phys. Rev. Lett.* **43**, 207-210 (1979).
- [16] S. Suckewer, J. Cecchi, *et al*, *Phys. Lett.* **80A**, 259-261 (1980).
- [17] S. Suckewer, R. Fonck and E. Hinnov, *Phys Rev A* **21**, 924-927 (1980).
- [18] S. Suckewer, R. Fonck and E. Hinnov, *Phys Rev A* **22**, 2278 (1980).
- [19] S. Suckewer, E. Hinnov, *et al*, *Phys Rev A* **26**, 1161-1163 (1982).
- [20] B. Denne, E. Hinnov, *et al*, *Phys Rev A* **28**, 206-208 (1983).
- [21] N. J. Peacock, M. F. Stamp and J. D. Silver, *Phys. Scr.* **T8**, 10-20 (1984).
- [22] S. Suckewer, *et al*, *Nucl. Fusion* **24**, 815-826 (1984).
- [23] K. H. Burrell, R. J. Groebner, *et al*, *Phys Rev A* **29**, 1343-1347 (1984).
- [24] B. Denne and E. Hinnov, *Phys Rev A* **29**, 3442-3443 (1984).
- [25] U. Feldman, J. F. Seely, *et al*, *J. Opt. Soc. Am. B* **3**, 1605-1608 (1986).
- [26] J. Reader, C. M. Brown, *et al*, *J. Opt. Soc. Am. B* **3**, 1609-1611 (1986).
- [27] B. Denne, E. Hinnov, *et al*, *Phys Rev A* **40**, 1488-1496 (1989).

- [28] U. Feldman, J. O. Ekberg, *et al.*, J. Opt. Soc. Am. B **6**, 1652-1655 (1989).
- [29] C. A. Morgan, *et al.*, Phys Rev. Lett. **74**, 1716-1719 (1995).
- [30] T. Pütterich, IPP-Report 10/29 (2006).

## **Chapter 2**

### **Experimental setup**

#### **2.1. 3m normal incidence spectrometer**

##### **2.1.1. Introduction**

Magnetic field topology in LHD is characterized by the presence of ergodic layer surrounding the closed magnetic surfaces. Magnetic field line structures are stochastic in such an ergodic layer, having no poloidal uniformity. The thickness of the ergodic layer typically ranges from 3 to 50cm, which largely changes according to each poloidal and toroidal position of the LHD edge plasmas. The ergodic layer plays an important role for confinement properties in LHD, because the ergodic layer is much thicker than ionization lengths of neutrals and the connection lengths of magnetic field lines are much longer than the ion-ion collision mean free path. Then, it becomes important for LHD to study the particle/impurity behaviors in the ergodic layer. Since electron temperatures are high enough at Last Closed Flux Surface (LCFS), typically 100-500eV, spectral lines of impurity ions stayed in the ergodic layer are mainly radiated in VUV region. VUV spectroscopy has been thus developed in LHD to measure the impurity distribution in the ergodic layer.

A space-resolved VUV spectroscopy was originally developed in the Compact Helical System (CHS) using a 1m normal incidence VUV monochromator equipped with a secondary electron multiplier and eight concave mirrors [1, 9]. Radial profiles of VUV

lines emitted in a wavelength range of 400-1600Å were measured by rotating an octagonal disk mounted on the eight concave mirrors with a time interval of 20ms. In the ASDEX-U, a similar system was constructed using a rotating mirror, a 1m normal incidence spectrometer with an ellipsoidal mirror and MCP-intensified photodiode detectors [2-3]. Radial profiles of the ion temperature were measured in the Advanced Toroidal Facility (ATF) from Doppler broadening of carbon, oxygen and nitrogen lines using a 1m vacuum Czerny-Turner spectrometer [4]. In LHD, a space-resolved 3m normal incidence spectrometer system has been constructed to observe vertical profiles of impurity lines emitted in a wavelength range of 500-3100Å in addition to radial profiles of the ion temperature and poloidal rotation [5]. A final goal of this system is to observe a three-dimensional distribution of impurity radiation in the ergodic layer by scanning a toroidal slit during a discharge. Recently, the vertical profiles of impurity emissions have been successfully obtained with the ion temperature profiles. In this chapter, the preliminary results are presented with an explanation on the space-resolved VUV spectroscopy in LHD.

### **2.1.2. Space-resolved 3m VUV spectrometer**

Figure 2.1 shows a schematic view of the space-resolved 3m VUV spectrometer system in LHD. A back-illuminated CCD detector (Andor model 435) is set at the exit slit position. The size of the CCD exposure area is  $13.3 \times 13.3 \text{mm}^2$  ( $13 \times 13 \mu\text{m}^2/\text{pixel}$ ) and the total number of channels are  $1024 \times 1024$ . The CCD is operated at a moderate temperature of  $-20^\circ\text{C}$  to reduce the thermal noise, which can be reduced to a negligible level. The frame transfer mode is used as a CCD operation method to reduce the transfer time of electric charges and to take clearer images. Using the frame transfer mode, a radial profile with 51 radial points can be recorded in a time interval of 125ms. Two gratings (1200grooves/mm,  $65 \times 150 \text{mm}^2$ , 1400Å blaze with Pt-coating and 3000Å blaze with Al-MgF<sub>2</sub>-coating) are installed in the 3m VUV normal incidence spectrometer (Mcpherson model 2253). The grating with 1400Å

blaze is used in the present study. The spectral resolution is  $0.05\text{\AA}$  at an entrance slit width of  $20\mu\text{m}$  and the reciprocal linear dispersion is  $2.75\text{\AA}/\text{mm}$ . This resolution is high enough to measure the Doppler width of impurity lines. When more precise spectral profiles are required for the Doppler temperature measurement, the second or third order light is used.

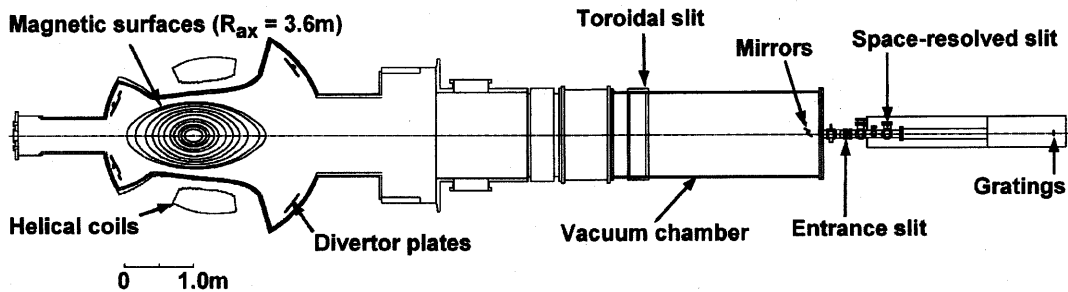


Fig. 2.1 Schematic view of space-resolved 3m VUV spectrometer system in LHD.

A space-resolved slit is placed between the entrance slit and the grating of the spectrometer to observe a vertical image of VUV emissions. The space-resolved slit with the width of  $267\mu\text{m}$  is used in most of the cases, which gives vertical resolution of  $20\text{mm}$ . The brightness of the spectral image decreased to  $1/60$  in comparison with the fully opened case. Therefore, the entrance slit is opened up to  $2\text{mm}$  in order to increase the signal intensity. Changing the entrance slit width from  $20\mu\text{m}$  to  $2\text{mm}$ , the signal intensity of spectral lines increases up to 100 times.

Two platinum-coated mirrors for view-angle adjustment are set in front of the entrance slit with an incidence angle of  $60^\circ$ . The minimum limit of observable wavelength range is determined by the reflection efficiency of the VUV emissions on the mirrors. The practical limit was  $500\text{\AA}$  whereas it was originally  $300\text{\AA}$  when the two mirrors were removed. The signal intensity is decreased by 10% when the mirrors are used. The optics is traced with flat and convex cylindrical mirrors in Fig. 2.2. The view-angle is essentially determined by the grating and CCD vertical sizes, the focal length of the spectrometer and the distance between the spectrometer and plasma positions in addition to the curvature of the convex cylindrical mirror. Three convex cylindrical mirrors with curvatures of  $R = 500, 750$  and

1050mm have been tested so far. We confirmed that the view-angle and the vertical image were adjustable by changing the curvatures. The observable vertical range is 1200mm at the plasma center when the cylindrical mirror of  $R = 750\text{m}$  is used. This curvature of the cylindrical mirror is good enough for the present profile observation.

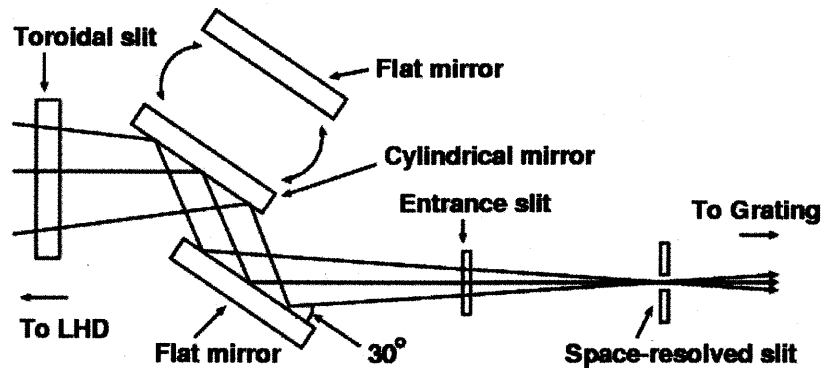


Fig. 2.2 Optics of space-resolved VUV spectroscopy and Pt-coated mirror arrangement.

A flat mirror is used for high-spatial-resolution measurement of edge plasmas, although the vertical observation area is limited to 200mm. By replacing the cylindrical mirror to the flat mirror with a rotary holder, the spatial resolution increases up to 4mm. The brightness of spectral lines also increases up to ten times compared with the cylindrical mirror case.

A toroidal slit is set at a diagnostic port between the spectrometer and the plasma. A three-dimensional measurement of impurity line emissions becomes possible by moving the toroidal slit during a single discharge. The vertical profile integrated toroidally over a length of 30mm is obtained when the toroidal slit width is fixed to 10mm. The elliptical LHD plasma rotates five times during a single toroidal turn. Then, a small extension of the toroidal view area easily reduces the vertical spatial resolution, especially at the edge region. The full toroidal observation length is 300mm.

All the parts including the wavelength scan of the spectrometer can be externally controlled by a desktop computer located in the LHD diagnostic room. The optical modem is used for the linkage between the experimental room and the diagnostic room using an

optical fiber of 200m in length. An interactional communication is provided by the RS-232C system. A computer for the CCD operation is located in the LHD experimental room and remotely accessed by a keyboard-video-mouse (KVM) extender from the diagnostic room with a LAN-cable of 200m in length. Data of the CCD are also transferred by the LAN-cable to a data-server set in the diagnostic room.

### 2.1.3. Radial profile measurement

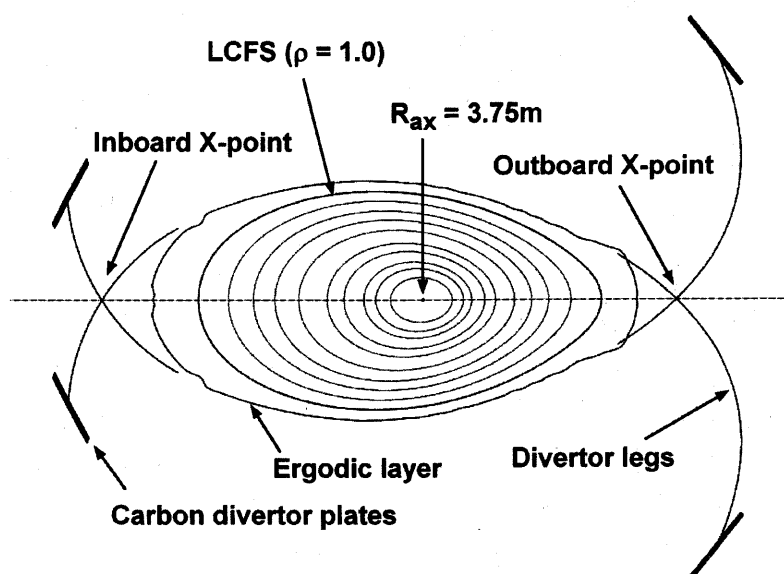


**Fig. 2.3** Schematic drawing of magnetic surfaces ( $R_{ax}=3.75m$ ), external form of ergodic layer, divertor legs and carbon divertor plates.

Figure 2.3 shows a poloidal cross-section at horizontally elongated plasma position of LHD ( $R_{ax}=3.75m$  case). Ten magnetic surfaces are traced in the figure as a function of normalized plasma radius,  $\rho (=r/a)$ . Here,  $r$  and  $a$  are the radial position and the plasma radius, respectively. The LCFS locates at the  $\rho=1.0$  position. The contour surrounding

the LCFS traces an outside boundary of the ergodic layer. The outside boundary of the ergodic layer in the present expression is defined by a region where the connection length of magnetic field lines to the vacuum wall is  $\sim 50\text{m}$ . This region does not form a clear magnetic surface, but has a considerably high temperature because of those long connection lengths. Typical electron temperature of the ergodic layer ranges between 10 and 500eV, depending on electron density, magnetic field strength and input heating power. The electron density of the ergodic layer is high enough and has normally a similar value to the central electron density. The divertor legs directly connect the edge plasma to the carbon divertor plates, which is a unique route for plasma particles coming out of the core plasma.

Typical examples on full vertical profiles of externally injected aluminum, argon and neon are shown in Fig. 2.4, where  $Z$  denotes the vertical distance from the equatorial plane. A cylindrical aluminum pellet with a size of 0.8mm in diameter and 0.8mm in length is injected by an impurity pellet injector [6]. The velocity of the impurity pellet accelerated by pressurized helium gas (15atoms) is 100-300m/s. The injected pellet is fully ablated within a few milliseconds and ionized toward higher ionization stages. The aluminum ions are confined in the core plasma of LHD with a particle confinement time of  $\sim 0.5\text{s}$ , which is much longer than the CCD exposure time (125ms). The rare gases of argon and neon are puffed by a piezoelectric valve during a discharge to maintain the amount of 1% to the electron density of  $2.5 \times 10^{13} \text{cm}^{-3}$ . The AlXI profile in Fig. 2.4(a) is taken in  $R_{\text{ax}}=3.60\text{m}$  configuration having a maximum plasma size in LHD, and the ArVIII and NeVIII are recorded in  $R_{\text{ax}}=3.70\text{m}$  configuration as shown in Fig. 2.4(b) and (c). Then, the AlXI profile is wider than the other two profiles. It is clearly seen that the vertical profiles have a symmetric feature at upper and lower positions, indicating no existence of a vertical asymmetry as seen in tokamaks [7, 10-16]. These symmetric profiles suggest that all such spectra are emitted inside the LCFS. If the emissions are located in the ergodic layer at  $\rho > 1.0$ , the profiles change to a complicated shape as will be shown later. The locations where the AlXI, ArVIII and NeVIII exist are compared with the electron temperature profiles. The result shows that these ions are located at a radial position where  $1 \leq T_e / \chi_i \leq 2$  ( $\chi_i$ : ionization potential).

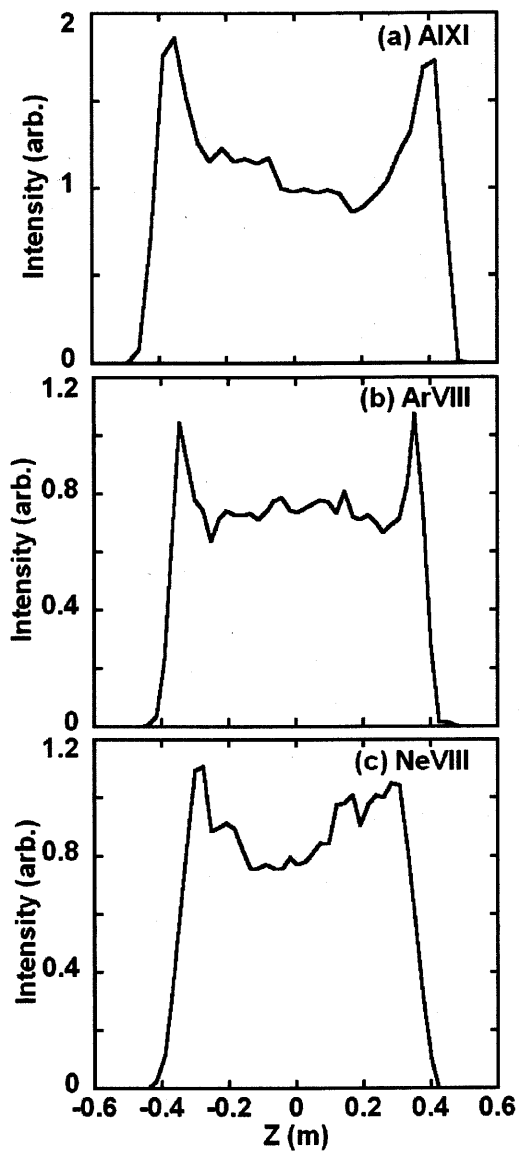


**Fig. 2.4** Full vertical profiles of impurity emissions: (a) AlXI 550Å ( $R_{ax}=3.60m$ ), (b) ArVIII 700Å ( $R_{ax}=3.70m$ ) and (c) NeVIII 770Å ( $R_{ax}=3.70m$ )

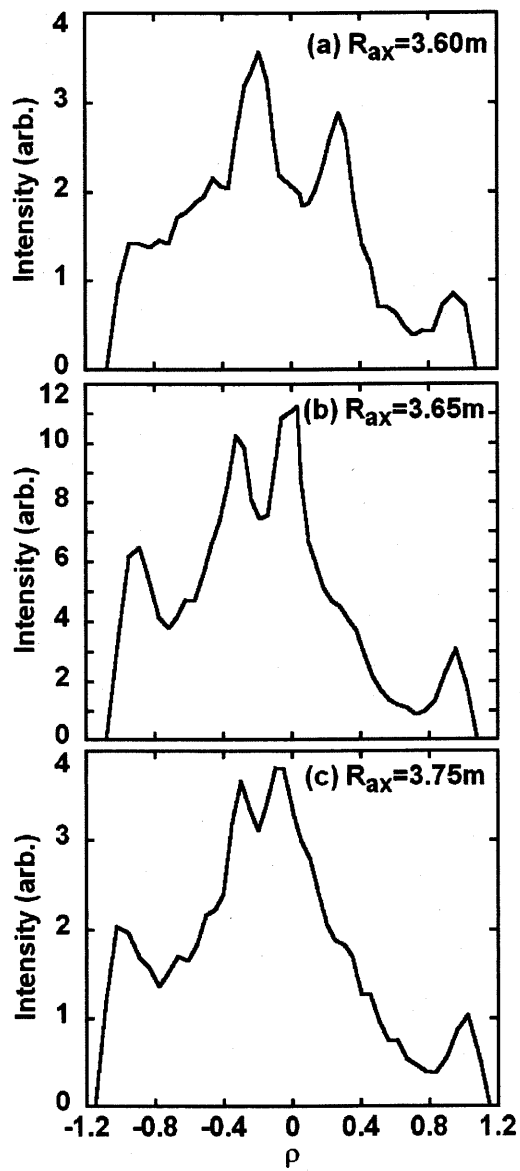


**Fig. 2.5** Radial profiles of CIV 1548Å emissions from (a)  $R_{ax}=3.60m$ , (b)  $R_{ax}=3.65m$  and (c)  $R_{ax}=3.75m$ .

Vertical profiles of CIV (1548Å) are measured in plasmas with three different magnetic axes ( $R_{ax}=3.60, 3.65$  and  $3.75\text{m}$ ), as shown in Fig. 2.5. The vertical positions of the profiles are converted into  $\rho$  for the comparison. The profiles are much different from the case of Fig. 2.4. In total four peaks (two weak edge peaks and two strong central peaks) appeared in the profiles. Two small peaks at the plasma edge near  $\rho=1.0$  and  $\rho=-1.0$  are formed by the chord integration of edge CIV emissions at the top and bottom edges of the elliptical plasma (see Fig. 2.3). However, two other strong peaks are seen near  $\rho=0$  originating from a different reason. In LHD, the particle recycling is enhanced at the inboard side [8]. The particles coming from the core plasma are collected on the carbon divertor plates through the inboard X-point and the carbon atoms are sputtered by such plasma particles at the inboard side. Thus, the carbon source is localized only at the inboard side divertor plates. However, the carbon emissions are weak at the inboard X-point where enough density cannot build up, since the connection length between the divertor plates and the inboard X-point is 2m. The density of CIV then increases at the area surrounding the inboard X-point and the resultant chord-integrated CIV profile is split into two peaks. The structures of carbon emissions at the inboard side change when the magnetic axis is moved as seen in Fig. 2.5. This change of the CIV profile reflects the simulated result that the poloidal location of the particle coming from the core plasma changes to upper side X-point at vertically elongated plasma position when the magnetic axis shifts outside. However, the detailed mechanism is not clear at present, because the magnetic field line structure and the related particle motion are very complicated in the ergodic layer. In order to understand these emission structures in detail, the three-dimensional image of the emissions is really required in addition to more detailed edge particle simulation in the ergodic layer.

Radial profiles of CIII-CV are measured from discharges with a Local Island Divertor (LID) as shown in Fig. 2.6. In the LID experiment, a carbon plate ( $1\text{m}^2$  in size) with crescent surface structure is inserted into a large  $m/n=1/1$  island which is created by external resonant coils. The amount of carbon impurity in such discharges becomes high, then, it leads to a large improvement of signal-to-noise ratio in the present diagnostics. The profile

of CIII in Fig. 2.6(a) indicates that the carbon source is located at some poloidal position, also suggesting an interaction with the LID carbon plate. The toroidal location of the 3m normal incidence spectrometer is  $180^\circ$  from the LID position. Therefore, the image of the carbon source is shaded off by the poloidal transport during the half toroidal turn of carbon ions. The profile of the CIII, of course, does not reflect the magnetic surface information. The CIV profile shown in Fig. 2.6(b) becomes much different from the CIII profile. The major emission of the CIV is located on the top side of the plasma edge and the asymmetric feature is still in the profile. On the other hand, this asymmetric feature completely disappears in the profile of the next ionization stage of CV, as shown in Fig. 2.6(c). The location of the CV moves considerably inside the LCFS because of its high ionization potential of 392eV, and the profile becomes a function of magnetic surface. From the CIV profile measurement it is made clear that the carbon source location moves to the opposite position when the magnetic field direction is inverted, as shown in Fig. 2.6(d). The beam orbit of tangentially injected neutral beams with an energy of 180keV is very sensitive to the direction of the magnetic field because of the different direction of grad-B drift. The difference in the interaction between the beam and the LID plate is considered to be a possible reason.

Vertical profiles of the ion temperature are also measured simultaneously with the emission profile [17-20]. A typical result on the CIV is shown in Fig. 2.7. The entrance slit width of the spectrometer is  $20\mu\text{m}$  and the second order light of CIV ( $2\times 1548\text{\AA}$ ) is used for the low ion temperature measurement. It can expand the lower limit of the ion temperature measurement down to a few eV. The CIV profile shown in Fig. 2.7 is obtained from a high-density ( $> 5\text{-}10\times 10^{19}\text{m}^{-3}$ ) discharge with a repetitive hydrogen pellet injection. The plasma size shrinks a little because of the low edge temperature. The ion temperature profile is plotted at steady phase of the discharge ( $t=0.675\text{s}$ ) and at decay phase after several pellet injections ( $t=1.05\text{s}$ ). The edge ion temperature during the steady phase has a complicated structure, suggesting a three-dimensional structure of plasma parameters in the ergodic layer of LHD. In the decay phase after the pellets, the ion temperature becomes low because of the rapidly increased density. The three-dimensional distribution of the ion

temperature is also necessary in order to understand the structure of the ergodic layer in LHD.

#### **2.1.4. Summary**

Radial profile measurement of impurity line emissions has been developed in LHD using a space-resolved 3m VUV spectrometer for the study of edge plasma behavior, especially the impurity behavior in the ergodic layer having no magnetic surface. Full vertical profiles and time behaviors of an intrinsic impurity of carbon and externally injected impurities of neon, aluminum and argon are successfully obtained. Vertical profiles of CIII and CIV show asymmetric features reflecting a structure of the ergodic layer plasma. Vertical profiles of the ion temperature are also measured from the CIV line with a complicated structure. Three-dimensional image of VUV line emissions, which are really required for understanding the structure of the ergodic layer plasma, has been measured preliminarily by scanning a toroidal slit. However, there remain a few technical problems such as VUV reflection from the facing vacuum wall, precise adjustment of optical axis and uniformity of diffraction efficiency on the grating. In the near future, the three-dimensional image of VUV line emissions will be well observed and such a result will be greatly helpful for understanding the ergodic layer plasma in LHD.

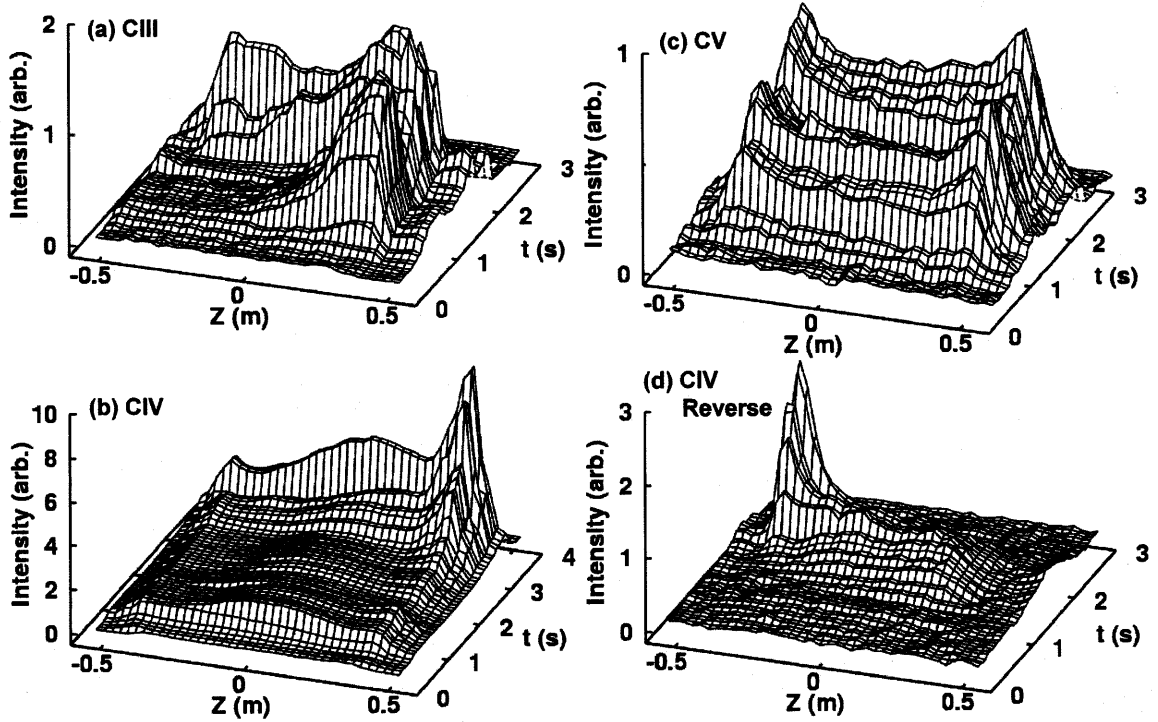


Fig. 2.6 Time developments of carbon vertical profiles of (a) CIII 977Å (Ionization Potential  $\chi_i=48\text{eV}$ ), (b) and (d) CIV 1548Å ( $\chi_i=65\text{eV}$ ) and (c) CV 2270Å ( $\chi_i=392\text{eV}$ ). Data are taken from NBI discharges with LID configuration and direction of toroidal magnetic field is inverted in the case of (d).

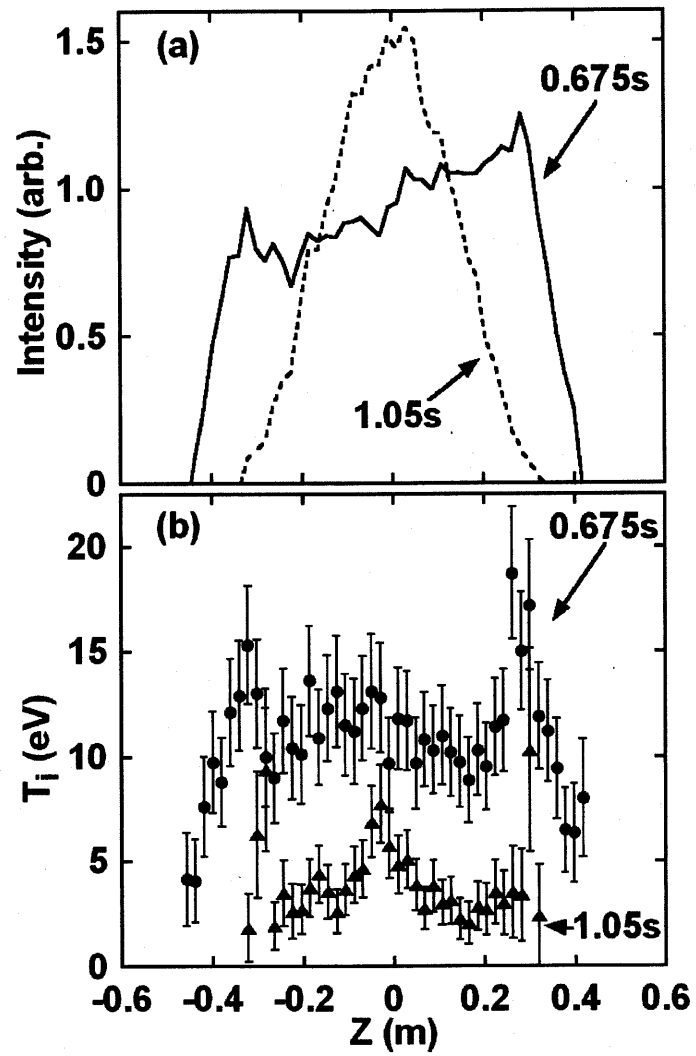


Fig. 2.7 Vertical profiles of (a) CIV emission (solid line: 0.675s and dashed line: 1.05s) and (b) ion temperature (solid circles: 0.675s and solid triangles: 1.05s).

## 2.2. Heavy element impurity pellet injection

A variety of emissions from many kinds of elements are necessary for development of high-temperature plasma spectroscopy. Impurities which do not intrinsically exist in plasmas are generally used for this purpose. The use of rare gas is one of the methods. In case of the rare gas, however, the source term of the injected gas can not be defined clearly due to the high-recycling rate of the rare gas. The laser blow-off technique, which is a method to inject metallic impurities into the plasma by focusing a pulse laser beam on a thin metallic layer deposited on a glass substrate [21], is widely used for impurity transport study and spectroscopic use because of the well defined source term and the easy method for observing metallic elements. It is possible to adjust the impurity amount by selecting the thickness of the metallic layer and the laser condition. However, it is difficult for plasmas with thick scrape-off-layer or ergodic layer to use the method, since the ablated impurity cloud is easily shielded by the outside layer surrounding the core plasma and does not penetrate into the plasma core. This effect becomes very typical in Large Helical Device (LHD). Therefore, an impurity pellet injector has been developed for spectroscopy of LHD [22].

The impurity pellet injection has been successfully operated for various purposes of the study. The cylindrical impurity pellet made of pure material such as carbon and aluminum has been generally used for the study. The size of the usually used impurity pellet ranges between 0.4-0.8mm. The pellet with size smaller than 0.4mm is not used because the treatment and injection are not easy technically. Therefore, an alternative design is required for the present impurity pellet in order to avoid the thermal collapse of discharges.

Two kinds of double-structural designs have been developed for the heavy element pellet injection. One of the designs is a cylindrical pure carbon pellet coated by heavy elements. The thickness of the coating is 5-15 $\mu$ m and the carbon pellet size is 0.5-0.8mm. A photograph of the Sn-coated carbon pellet is shown in Fig.2.8 as an example. The surface

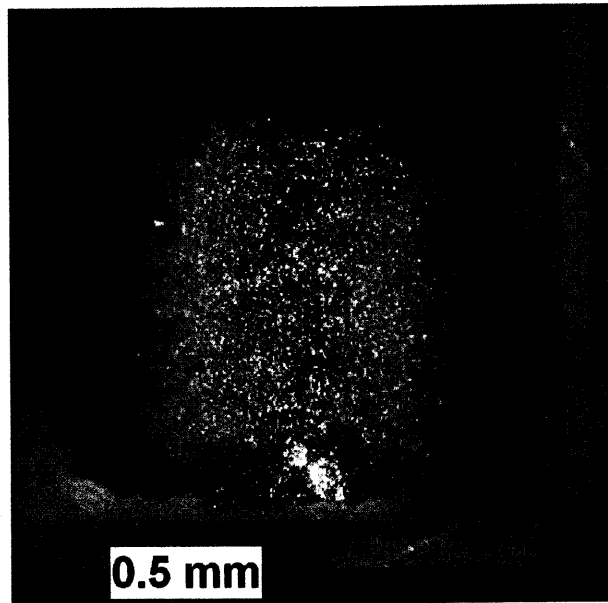


**Fig. 2.8** Cylindrical carbon pellet with tin (Sn) coating. Total size of the pellet is 0.9mm in diameter and 0.8mm in length.

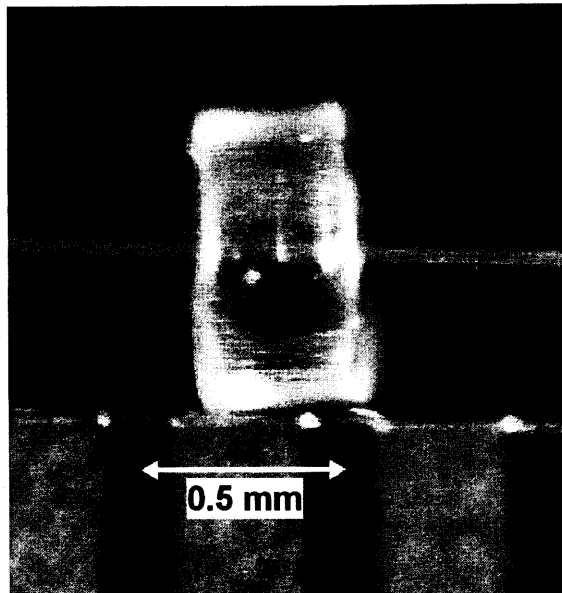


**Fig. 2.9** Co-axial impurity pellet inserted tungsten (W) wire into polystyrene tube. Diameter of wire is 150 $\mu$ m and diameter of the tube is 0.8mm. Division of scale is 0.5mm.

roughness originates in substrate carbon but not in the coating inhomogeneity. This pellet is fully fabricated in Institute of Laser Engineering at Osaka University by applying the electroplating technique [23]. The electrolyte and other electrochemical conditions are shown in the paper. Another design of the pellet is a carbon or polyethylene tube pellet inserted a thin heavy element wire. A photograph of the polystyrene tube pellet is shown in Fig.2.9. The inserted tungsten wire with a diameter of 150 $\mu\text{m}$  is not cut in the photograph for better understanding of the pellet structure. Since the wire is tightly inserted in the tube, it does not separate from the tube even when the pellet is shot by He gas pressurized to 15atoms.

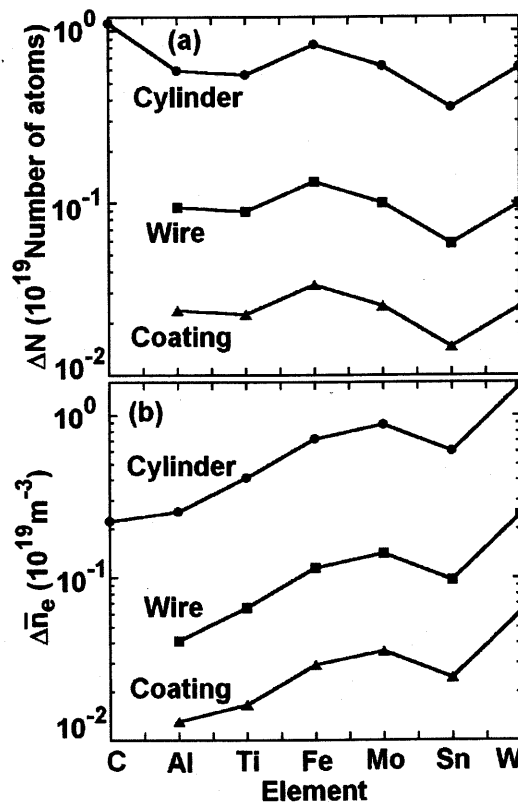


**Fig. 2.10** (a) Amount of heavy element for three kinds of impurity pellets. (b) Electron density rise from heavy element in LHD under assumption that the heavy element is fully ionized. (Cylinder: 0.5mm $\times$ 0.5mm $\dagger$ , Wire: 0.2mm $\times$ 0.5mm $\dagger$ , Coating: 10 $\mu\text{m}^\dagger$  on 0.5mm cylinder).

The amount of heavy element included in the pellet is calculated, as shown in Fig.2.10(a). The coating method can reduce to the amount of the element less than 10% of the cylinder case. Since the thick coating on the carbon surface is technically difficult, we can choose a suitable amount of the element by selecting either of the coating or the wire methods. The density rise with the pellet injection plotted in Fig.2.10(b) is calculated under an assumption that all the heavy element particles included in the pellet are fully ionized in the plasma volume of  $30\text{m}^3$  in LHD.

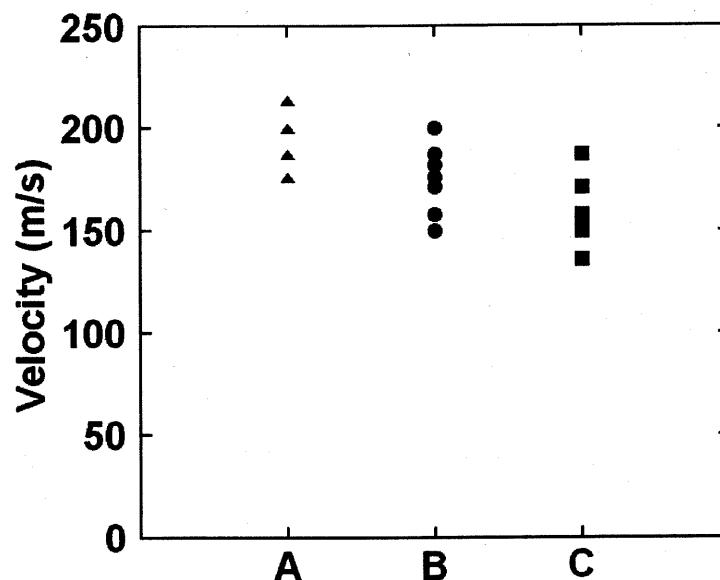


**Fig. 2.11** Velocities of impurity pellets shot with 15 atom helium gas (A: Cylindrical pure carbon  $0.8\text{mm}^{\circ}\times 0.8\text{mm}^{\dagger}$ , B: Co-axial pellet ( $0.8\text{mm}^{\circ}\times 0.8\text{mm}^{\dagger}$ ) inserted molybdenum wire  $0.2\text{mm}^{\circ}\times 1.0\text{mm}^{\dagger}$ , C: Co-axial pellet ( $0.8\text{mm}^{\circ}\times 0.8\text{mm}^{\dagger}$ ) inserted tungsten wire  $0.2\text{mm}^{\circ}\times 1.0\text{mm}^{\dagger}$ ). Velocity of coated impurity pellet is identical to the pure carbon pellet.

The velocity of the pellet is measured by a time-of-flight method using parallel He-Ne laser light and two narrow rectangular slits separated each other in a distance of 3mm, which is set in front of an avalanche photodiode (APD). The signal from the APD is digitized with a sampling time of 10 MHz. The velocity of cylindrical pure carbon ( $0.8\text{mm}^{\circ}\times 0.8\text{mm}^{\dagger}$ ) without coating denoted with 'A' ranges in 175-215m/s (see Fig.2.11).

The velocity of the Sn-coated carbon pellet is entirely identical to the case of 'A'. The velocities of Mo- and W-inserted tube pellets are a little lower than the cylindrical carbon pellet, but no significant difference appears between the Mo- and W-inserted tube pellets. These velocities are enough high for penetrating the edge plasma and ablating the pellet at the core plasma.

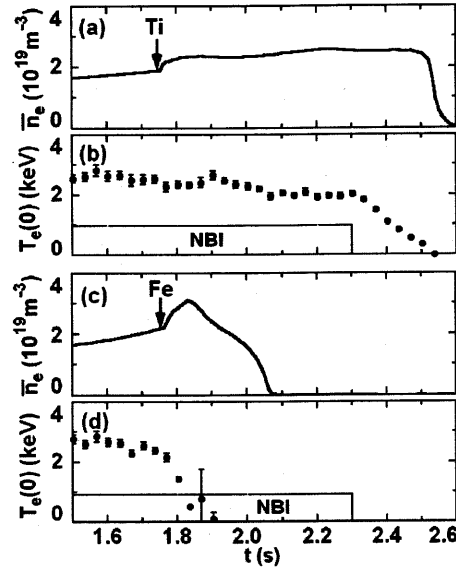


**Fig. 2.12** Temporal behaviors of the line-averaged electron density (a) and (c) and central electron temperature (b) and (d) for titanium ( $0.5\text{mm}^{\phi} \times 0.3\text{mm}^{\text{h}}$ ) and iron ( $0.5\text{mm}^{\phi} \times 0.3\text{mm}^{\text{h}}$ ) cylindrical pellet injection, respectively. The line-averaged electron density and the central electron temperature are measured from far-infrared interferometer and Thomson scattering, respectively.

Figure 2.12 shows the results when the 0.5mm-size cylindrical pellet is injected in LHD. Titanium and iron pellets are injected at 1.76s. In titanium case, the discharge can be smoothly sustained with a small density rise of  $0.4 \times 10^{19} \text{ m}^{-3}$  (see Figs. 2.12(a) and (b)). On the other hand, the discharge can not be sustained for iron pellet injection due to mainly the large ionization and radiation losses as shown in Figs. 2.12(c) and (d). The threshold of the impurity pellet element which can be used in LHD clearly exists at  $Z=22$ , when the 0.5mm-size cylindrical impurity pellet is injected. Therefore, alternative method has to be

developed for heavier element injection into LHD.

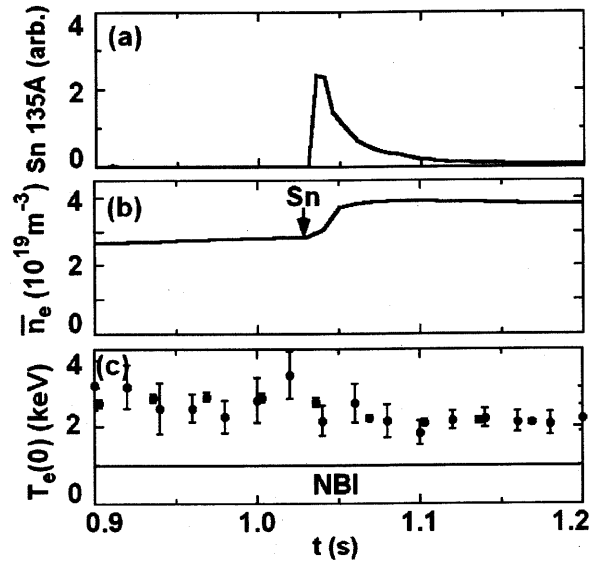


**Fig. 2.13** Temporal behavior of LHD discharges with cylindrical Sn-coated carbon pellet ( $0.8\text{mm}^{\circ}\times 0.8\text{mm}^{\dagger}$  with  $6.7\mu\text{m}$  coating).

The newly developed impurity pellets are tested by injecting into the LHD discharges. Figure 2.13 shows the waveform of the discharges that the Sn-coated pellet with  $6.7\mu\text{m}$  in thickness is injected at  $t=1.03\text{s}$ . The central electron temperature decreases mainly due to the central deposition of the Sn-coated carbon pellet, which is estimated to be within  $\rho=0.5$  from Thomson density profile, in addition to the density increase of  $1.0\times 10^{19}\text{m}^{-3}$  and enhanced radiation loss. The EUV line radiation from low-ionized SnIX-XIII ions emitted at  $135\text{\AA}$ , which is used for light source in next-generation lithography, is successfully measured with a flat-field EUV spectrometer [24] in the stable discharge without thermal collapse (see Fig. 2.13(a)).

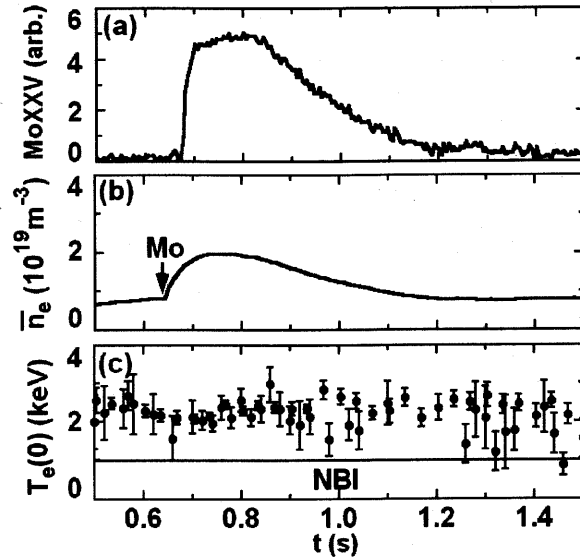


Fig. 2.14 Temporal behavior of LHD discharge with Mo-inserted co-axial impurity pellet (Mo:  $0.2\text{mm}^{\circ} \times 1.0\text{mm}^{\text{l}}$ ).

Result of the trial on the Mo-inserted co-axial pellet is shown in Fig.2.14. The pellet is injected at  $t=0.64\text{s}$ . The discharge is not affected by the impurity pellet injection and is well sustained with a density rise of  $1.2 \times 10^{19} \text{m}^{-3}$ . The co-axial pellet is ablated in the plasma outer region near  $\rho=0.8-0.9$  due to the low melting point of the plastic tube. The EUV line emission of MoXXV ( $108.25\text{\AA}$ :  $3p^6 1S_0-3p^5 3d 3P_1$ ) measured in this discharge is plotted in Fig.2.14(a) [24-26]. The MoXXV begins to increase in the emission with a delay time of 15ms after the co-axial impurity pellet injection. It suggests the ionization time until neutral molybdenum reaches  $\text{Mo}^{24+}$  ions in the present LHD plasma condition.

In summary newly designed high-Z impurity pellets have shown here indicated a favorable character as the source of active spectroscopy in high-temperature plasmas. These methods can be applied to the spectroscopic study of heavy elements such as molybdenum and tungsten, which are candidates for the plasma facing materials in the next generation fusion device. Furthermore, the pure carbon has a high melting point [27], and then the impurity pellet using the pure carbon is certainly applicable to the spectroscopic study in the core side of the burning plasmas with extremely high energy storage.

## References

- [1] S. Morita, S. Muto and M. Sakurai, *Fusion Eng. Des.* **34-35**, 211-214 (1997).
- [2] U. Wenzel, *et al.*, *Fusion Eng. Des.* **34-35**, 225-229 (1997).
- [3] A. R. Field, *et al.*, *Rev. Sci. Instrum.* **66**, 5433-5441 (1995).
- [4] R. C. Isler, *et al.*, *Nucl. Fusion* **29**, 1391-1397 (1989).
- [5] S. Morita and M. Goto, *Rev. Sci. Instrum.* **74**, 2036-2039 (2003).
- [6] H. Nozato, *et al.*, *Rev. Sci. Instrum.* **74**, 2032-2035 (2003).
- [7] K. Brau, S. Suckewer and S. K. Wong, *Nucl. Fusion* **23**, 1657-1668 (1983).
- [8] M. Goto and S. Morita, *Phys. Rev. E* **65**, 026401-1-6 (2002).
- [9] X. Lin and J. Xie, *Rev. Sci. Instrum.* **71**, 2068-2070 (2000).
- [10] B. Lipschultz, *et al.*, *Nucl. Fusion* **24**, 977-988 (1984).
- [11] F. P. Boody, *et al.*, *J. Nucl. Mater.* **145-147**, 196-200 (1987).
- [12] R. C. Isler, *et al.*, *Nucl. Fusion* **29**, 1384-1390 (1989).
- [13] U. Wenzel, *et al.*, *J. Nucl. Mater.* **241-243**, 728-733 (1997).
- [14] U. Wenzel, *et al.*, *Plasma Phys. Control. Fusion* **41**, 801-818 (1999).
- [15] Y. Liang, *et al.*, *Phys. Rev. Lett.* **94**, 105003-1-4 (2005).
- [16] B. J. Peterson, *et al.*, *Plasma Fusion Res.* **1**, 045-1-9 (2006).
- [17] S. Suckewer and E. Hinnov, *Nucl. Fusion* **17**, 945-953 (1977).
- [18] S. Miyachi, *et al.*, *J. Quant. Spectrosc. Radiat. Transfer.* **42**, 355-357 (1989).
- [19] A. Baciero, *et al.*, *Rev. Sci. Instrum.* **72**, 971-974 (2001).
- [20] H. Sakakita, *et al.*, *Rev. Sci. Instrum.* **74**, 2111-2114 (2003).
- [21] S. A. Cohen, J. L. Cecchi and E. S. Marmor: *Phys Rev Lett.* **35** 1507-1510 (1975).
- [22] H. Nozato, S. Morita, M. Goto, A. Ejiri and Y. Takase: *Rev. Sci. Instrum.* **74** 2032-2035 (2003).
- [23] K. Nagai, D. Wada, M. Nakai and T. Norimatsu: *Fusion Sci. Technol.* **49** 686-690 (2006).
- [24] M. B. Chowdhuri, S. Morita, M. Goto, H. Nishimura, K. Nagai and S. Fujioka, *Rev. Sci. Instrum.* **78** 023501-1-7 (2007).

- [25] A. Wouters, J. L. Schwob, S. Suckewer, J. F. Seely, U. Feldman and J. H. Davé, *J. Opt. Soc. Am. B* **5** 1520-1527 (1988).
- [26] B. Denne, G. Magyar and J. Jacquinot, *Phys. Rev. A* **40** 3702-3705 (1989).
- [27] S. Morita, H. Nozato, M. Goto *et al.*, Proc.30th. European Conference on Controlled Fusion and Plasma Physics, St.Petersburg, 2003 (European Physical Society) Vol.27A, P-3.13 (2003).

## **Chapter 3**

### **Observation of spectra**

#### **3.1. High-resolution VUV spectra of carbon, neon and argon**

##### **3.1.1. Introduction**

The purpose of passive plasma spectroscopy in fusion research is mainly to diagnose particle behaviors of impurity and fuel atoms and ions including the measurement of line radiation loss in addition to the contribution to atomic physics [1]. For the purpose the first resonance lines have been usually measured except for divertor diagnostics in which visible spectroscopy is useful. The resonance lines from highly ionized impurities are emitted in vacuum ultraviolet (VUV) region. Therefore, VUV spectroscopy becomes important for passive plasma spectroscopy and the resonance lines from typical intrinsic impurities such as carbon, oxygen and iron have been routinely measured in the VUV region in many magnetic fusion devices [2-11].

On the other hand, several wall conditioning techniques have been recently progressed, i.e., high-temperature baking of plasma facing components, He-glow discharge for wall cleaning and boronization of the vacuum wall. In addition, the vacuum wall has been fully covered by carbon plates and the carbon plates have been also installed in the divertor section. Thus, the impurity concentration in toroidal fusion devices has been much reduced.

According to the progress of the wall conditioning, spectral lines useful for passive spectroscopy in VUV region have been limited to the carbon emissions. External impurity injection is needed for a study on impurity behavior. The use of rare gas is one of good methods to overcome the present difficult situation in the passive spectroscopy. At present neon or argon is a possible candidate as the seeded gas. In ITER the use of krypton is planned for the spectroscopic diagnostics. Recently, such rare gases have been also used for edge plasma cooling based on the enhancement of radiation loss in order to reduce the divertor heat flux [12]. Therefore, it becomes important to investigate and identify the VUV spectral lines emitted from highly ionized ions of such rare gas elements for the alternative spectroscopic measurement in fusion devices.

Large Helical Device (LHD) is a toroidal fusion device without plasma current for confinement. Rare gas discharges are easily produced in LHD because current-driven MHD instability can be essentially avoided. Then, the VUV spectra of highly ionized rare gases such as neon and argon are studied using the rare gas discharges in LHD. The central electron density and temperature of the rare gas discharges used for the present study range in  $10^{18}$ - $10^{19}$  m<sup>-3</sup> and 2-4keV, respectively. The VUV spectra in a wavelength of 250 to 2300Å are observed by using a 3m normal incidence spectrometer with high spectral resolution of  $\Delta\lambda \sim 0.2$ Å. The spectral resolution observed here is narrower than Doppler broadening of most of the VUV lines emitted from the LHD plasmas. Therefore, the VUV spectra measured here can give the best spectral resolution as compared with the former results. In this paper the VUV spectra from carbon, neon and argon are presented and the wavelengths are tabulated with their relative intensities, the full width at half maximum (FWHM) and the ion temperature for spectroscopic use. Typical spectral lines useful for spectroscopic diagnostics of high-temperature plasmas are also summarized for the three elements. A self-absorption spectrum is observed in Lyman series of neutral hydrogen instead of Doppler broadening. The spectra of hydrogen Lyman series are also presented with an analysis.

### 3.1.2. Line identification of C, Ne and Ar

Identification of VUV spectrum is compiled by using previous experimental spectra and wavelength tables [16-24]. VUV spectra are obtained by scanning the wavelength of the spectrometer shot by shot. Figures 3.1-1 to 3.1-7 show VUV spectra from neon discharges in wavelength range of 250 to 1275Å. A VUV spectrum of 2257-2296Å is shown in bottom trace of Fig. 3.1-7 with He-like CV (ionization potential: 392eV) line at 2270Å. Below 435 Å, VUV spectra having relatively strong emissions from metallic impurities of iron and chromium ions (Na- and Mg-like) are specially selected as an exception of the present work. It will be useful as a reference of spectroscopic use.

Figures 3.2-1 to 3.2-9 show VUV spectra from argon discharges in wavelength range of 355 to 1565Å. In Figs. 3.2-1 to 3.2-9, oxygen and nitrogen lines are appeared with relatively strong intensities, because the data are taken just after a little air leak into the vacuum vessel. This is a good reference for diagnostics of light impurities. A little amount of boron is also seen in the spectra. Boronization is carried out to make boron coating on the stainless steel vacuum wall in order to suppress the metallic impurities.

Carbon lines identified from the spectra are listed in Table 3.1. The order in the table denotes the maximum number of higher order line seen in the figures. The relative intensity is defined by total counts summed over the line spectral range based on a least-square Gaussian fitting of the measured spectral profile, and the FWHM and the ion temperature are evaluated by the Gaussian profile. Almost of carbon lines are blended with neighbor lines, and then available lines for diagnostics are very limited. Only eight lines (CII 1334.5323Å, 1335.7077Å, CIII 386.2028Å, 574.281Å, 977.020Å, CIV 1548.20Å, 1550.77Å, CV 2270.89Å) are isolated from other lines. Here, the CIII: 574Å - 5696Å and CIV: 312.422Å, 312.453Å - 5801Å, 5812Å form the branching pair which has the same upper levels for the transitions. The branching ratio method is available to absolute sensitivity calibration of VUV spectrometers [7, 9, 10, 25-28].

Neon lines are listed in Table 3.2. The charge states of NeIII (O-like) -IX (He-like) are identified from the spectra in the present wavelength region. One line isolated from other

lines at least exists in each charge state except for NeIX 1248.28Å. The NeIX line with high ionization potential of 1196eV is very useful for spectroscopic diagnostics, especially for the ion temperature measurement from Doppler broadening. However, the 1st order of the NeIX (1248.28Å) is blended with the 3rd order NeV line (3×416.20Å). Then, it is better to measure the 2nd order for NeIX in order to observe the accurate line profile. The 6th order of NeV (6×416.20Å) becomes much weak as compared to the 2nd order of NeIX (2×1248.28Å) and the separation between the two lines is also better in case of the 2nd order for NeIX.

Argon lines are listed in Table 3.3. In case of the argon the magnetic dipole (M1) transition (ArXII 649.03Å) is observed [29-31]. This is the first observation in fusion plasmas. In tokamaks the maintenance of high-Z discharges is not generally easy because of the current-driven instability. As the ArXII M1 line is much weaker than resonance lines and the brightness of the VUV diagnostic system is darker than that of the visible diagnostic system, it was usually difficult to observe such the Ar M1 line. On the contrary the maintenance of high-Z discharges is quite easy in LHD. Therefore, pure Ar discharges can be performed at an electron density region of  $0.5-3 \times 10^{13} \text{cm}^{-3}$ . This is the reason why the ArXII M1 line was found for the first time in LHD. Several M1 transitions from argon have been also observed in LHD in the visible range. The wavelengths of the VUV lines suitable the plasma diagnostics are summarized in Table 3.4. It is seen that lines of CIII-V, NeIII-IX, ArIII-VIII and ArXV-XVI are available.

### 3.1.3. Ion temperature from the Doppler broadening

Ionization potential (IP) increases when the ionization stage of impurity ions goes up or the nuclear number Z of impurity elements increases, as shown in Fig. 3.3. The IP gradually increases with the ionization stages except for He- and H-like ions. The impurities in such ionization stages usually locate in some radial position of plasma when the central electron temperature is enough high as compared to the IPs. On the contrary,

the IP of He-like ions becomes much high, since the ionization of 1s electron requires a large energy compared with the ionization of n=2 electrons. Therefore, the emissions are useful to the ion temperature measurement at the plasma center.

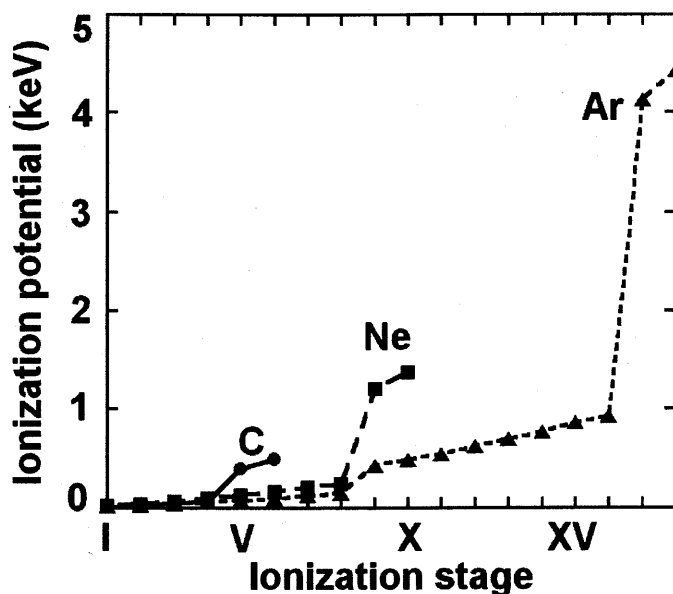


Fig. 3.3 Ionization potential of carbon, neon and argon ions as a function of ionization stages.

Figure 3.4 shows the ion temperature evaluated from Doppler broadening of measured VUV line emissions of neon and argon as a function of the IPs. The ion temperature of neon ions in various ionization stages distributes in a range of 1/2-1/4 of the ionization potential in each ion. However, the ion temperature of argon ions closely distributes to the IP. This is based on the difference in the central ion temperature. It is well known that the high ion temperature operation is possible to the rare gas discharges in LHD [32, 33]. The central ion temperature of the neon discharges ranges 3-5keV. In case of the argon discharges the ion temperature further increases up to 10-13keV mainly due to the less ion density, which leads to the increase in the ion heating power deposition.

Measurement of the ion temperature is also useful to the identification of the unclassified Ar lines. Several unclassified Ar lines appear in the Table 3.3. We also measured the ion temperature from the unclassified Ar lines. The ionization stages of such unclassified Ar

lines can be estimated from Fig.3.4(b) using the measured ion temperature. Thus, the unclassified Ar lines of 486.60Å (III), 618.63Å (VI-VIII) and 619.04Å (VI-VIII) are identified with the possible ionization stages. Results are indicated in the brackets after 'ArUn'.

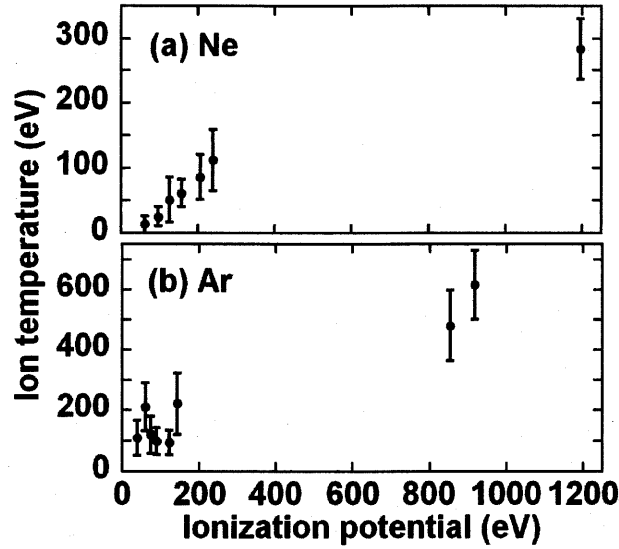


Fig. 3.4 Ion temperature evaluated from Doppler broadening of (a) neon and (b) argon VUV lines.

### 3.1.4. Line profile analysis of absorption spectra

The line profile of the Doppler broadening has a Gaussian shape if it is assumed the atoms or ions have the Maxwellian velocity distribution as follows;

$$I(\lambda) = \frac{1}{\sqrt{\pi}\Delta_D} \exp\left(-\frac{(\lambda - \lambda_0)^2}{\Delta_D^2}\right), \quad (1)$$

where  $\lambda_0$  is the center wavelength in Å and  $\Delta_D$  the Doppler width. The Doppler width at full width at half maximum (FWHM),  $\Delta_{FWHM}$ , is given by

$$\Delta_{FWHM} = 2\sqrt{\ln 2} \Delta_D$$

$$=7.71 \times 10^{-5} \lambda_0 \sqrt{\frac{T_i}{M}}. \quad (2)$$

The ion temperature in eV is thus given by

$$T_i = 1.68 \times 10^8 M (\Delta_{\text{FWHM}}/\lambda_0)^2, \quad (3)$$

where  $M$  is the atomic weight. Measured spectral lines are fitted by the Gaussian profile of the eq.(1) and the ion temperature is obtained using the eq.(3). Typical examples of the results are shown in Fig.3.5 for CIV  $2 \times 1548 \text{ \AA}$  and CV  $2270 \text{ \AA}$  lines. The experimental data can be fitted by the Gaussian profile. The ion temperature obtained from this fitting is indicated in the figure.

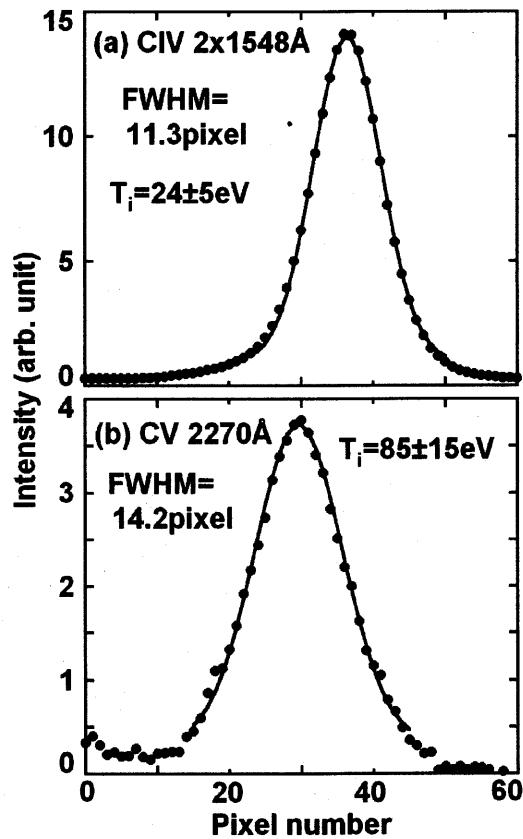


**Fig. 3.5** Spectral profiles of (a)  $2 \times \text{CIV}$  and (b)  $\text{CV}$  with Doppler broadening. Solid circles indicate raw experimental data and solid lines are fitting curves with Gaussian profiles.

On the other hand, neutral lines, especially Lyman-series lines ( $1s-np$ ,  $n \geq 2$ ) excited from hydrogen neutrals, have a completely different line profile from the Doppler profile. It is found in relatively high-density ( $>3.0 \times 10^{19} \text{ m}^{-3}$ ) discharges of LHD. Typical results on Lyman- $\alpha$  (HI:  $1s-2p$ ) are shown in Fig.3.6. Experimentally measured line profiles are denoted with solid circles. The Lyman- $\alpha$  lines are measured at the second order emission ( $2 \times 1215.67 \text{ \AA}$ ) in order to raise the spectral resolution. It is clearly seen that the top of the profile is deformed with electron density. It is well known that the neutral line is absorbed by the background neutral atoms [34].

The self-absorption line profile [35] is expressed using the Doppler broadening line profile as follows;

$$I_{SA}(\lambda) = I(\lambda) \exp(-kl), \quad (4)$$

The atomic absorption coefficient  $k$  is given by

$$k = k_0 \exp\left(-\frac{(\lambda - \lambda_0)^2}{\Delta_{SA}^2}\right), \quad (5)$$

where  $k_0$  is the atomic absorption coefficient at the center of the line and  $l$  the path length of absorption. The self-absorption line profile is then given by

$$I_{SA}(\lambda) = \frac{1}{\sqrt{\pi}\Delta_D} \exp\left(-\frac{(\lambda - \lambda_0)^2}{\Delta_D^2}\right) \times \exp\left\{-k_0 l \exp\left(-\frac{(\lambda - \lambda_{SA})^2}{\Delta_{SA}^2}\right)\right\} \quad (6)$$

Taking 0-th and 1st order terms after expansion of eq.(6), the eq.(6) is replaced by the following equation;

$$I_{SA}(\lambda) = \frac{1}{\sqrt{\pi}\Delta_D} \exp\left(-\frac{(\lambda - \lambda_0)^2}{\Delta_D^2}\right) \times \left\{1 - k_0 l \exp\left(-\frac{(\lambda - \lambda_{SA})^2}{\Delta_{SA}^2}\right)\right\}, \quad (7)$$

where  $k_0 l$  is the optical depth,  $\lambda_{SA}$  the center wavelength of absorption and  $\Delta_{SA}$  the absorption width. The self-absorption spectra of the Lyman- $\alpha$  line shown in Fig.3.6 are fitted by the eq.(6), which is expressed with solid line. The measured Lyman- $\alpha$  line profile is in good agreement with the consideration of self-absorption process. The self-absorption is also shown in Fig.3.7 for Lyman- $\beta$  line ( $2 \times 1025.72 \text{ \AA}$ ). The line profile of the

Lyman- $\beta$  has a very similar to the Lyman- $\alpha$  and can be well explained by the absorption process.

This absorption process is of course a function of edge neutral density  $n_n$  and length of the neutral  $l$ . The product of neutral number density and length of neutral density,  $n_n l$ , is given by the  $k_o l$  in eq. (6) and background neutral hydrogen temperature  $T_n$  in eV as follows;

$$n_n l = 1.67 \times 10^{15} k_o l \sqrt{1.67 \times 10^4 T_n} . \quad (8)$$

The optical depth of  $k_o l$  can be obtained from the line fitting by the eq.(7), as shown in Fig.6 and are determined to be  $k_o l = 0.55$  at  $\bar{n}_e = 5 \times 10^{19} \text{m}^{-3}$  and  $k_o l = 0.70$  at  $\bar{n}_e \sim 10 \times 10^{19} \text{m}^{-3}$ . The  $T_n$  is derived from  $\Delta_{SA}$  with eqs.(2) and (3). The instrumental width of the spectrometer for  $\Delta_{SA}$  is neglected in this analysis. The value of the optical depth is now insensitive to the density variation. When  $T_n = 0.5 \text{eV}$  and  $k_o l = 0.55$  at  $\bar{n}_e = 5 \times 10^{19} \text{m}^{-3}$  is assumed as Fig. 6(b), we obtain  $n_n l = 7.0 \times 10^{16} \text{m}^{-2}$  using eq.(8). Finally, we obtain the length of the neutral hydrogen of  $l = 10 \text{cm}$  (1cm) at  $n_n = 7.0 \times 10^{17} \text{m}^{-3}$  ( $7.0 \times 10^{18} \text{m}^{-3}$ ). This is fairly reasonable taking into account the measurement of neutral density from visible spectroscopy where the only  $n_n l$  is obtained [36]. Therefore, the result suggests that the absorption of hydrogen emissions is occurred at the plasma edge region.

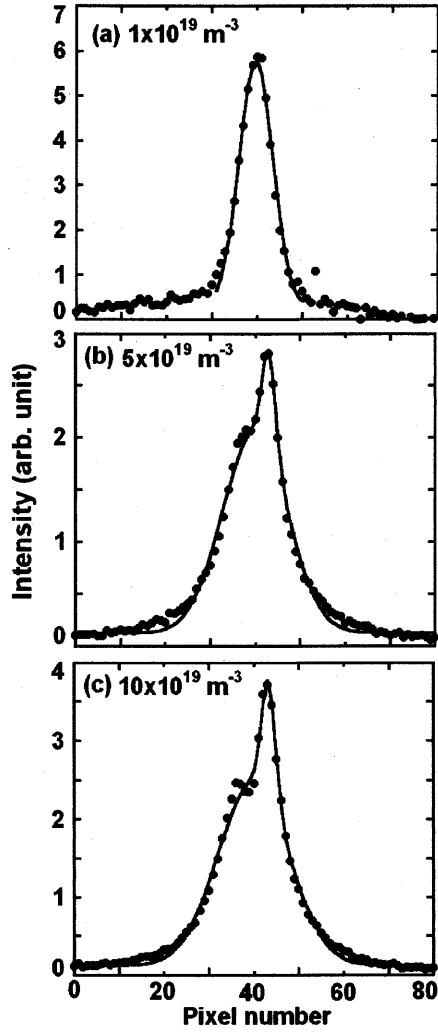


**Fig. 3.6** Line profiles of hydrogen Lyman- $\alpha$  ( $2 \times 1215.67 \text{ \AA}$ ) with self-absorption. Solid circles indicate raw experimental data in line-averaged electron density of (a)  $\bar{n}_e = 1 \times 10^{19} \text{ m}^{-3}$ , (b)  $\bar{n}_e = 5 \times 10^{19} \text{ m}^{-3}$  and (c)  $\bar{n}_e = 10 \times 10^{19} \text{ m}^{-3}$ . Solid lines express (a) Gaussian fitting curve with  $T_i = 1.5 \pm 0.5 \text{ eV}$  ( $\Delta_D = 5.2 \text{ pixels}$ ) and self-absorption fitting curves with (b)  $T_i = 9.2 \pm 1.0 \text{ eV}$  ( $\Delta_D = 10.2 \text{ pixels}$ ),  $T_n = 0.5 \pm 0.2 \text{ eV}$ , ( $\Delta_{SA} = 2.1 \text{ pixels}$ ) and (c)  $T_i = 11.4 \pm 1.1 \text{ eV}$  ( $\Delta_D = 11.2 \text{ pixels}$ ),  $T_n = 0.5 \pm 0.2 \text{ eV}$  ( $\Delta_{SA} = 2.2 \text{ pixels}$ ).

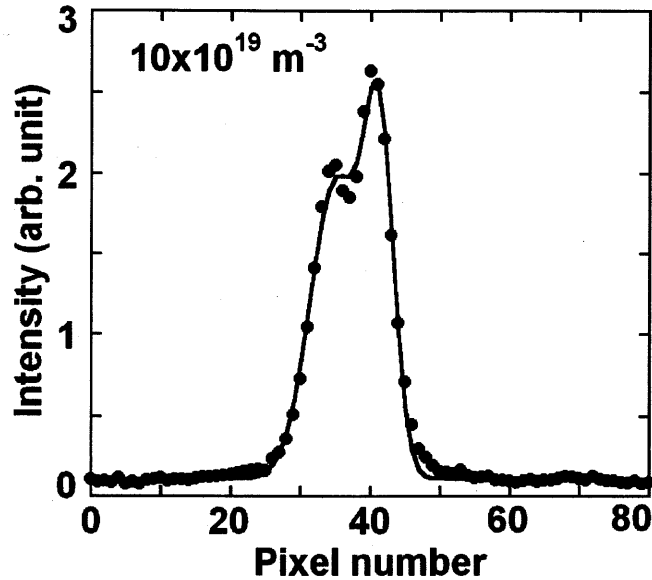


Fig. 3.7 Line profile of hydrogen Lyman- $\beta$  ( $2 \times 1025.72 \text{ \AA}$ ) with self-absorption. Solid circles indicate raw experimental data in line-averaged electron density of  $\bar{n}_e = 10 \times 10^{19} \text{ m}^{-3}$ . Solid line is self-absorption fitting curve with  $T_i = 2.4 \pm 1.2 \text{ eV}$  ( $\Delta_D = 5.1$  pixels) and  $T_n = 2.0 \pm 0.5 \text{ eV}$  ( $\Delta_{SA} = 2.1$  pixels).

### 3.1.5. Summary

High-resolution spectra (250 to 2300 $\text{\AA}$ ) have been measured in wavelength range of 250 $\text{\AA}$  to 2300 $\text{\AA}$  using a 3m normal incidence spectrometer in LHD and spectra from C, Ne and Ar have been recorded with good signal-to-noise ratio. Line identification, relative intensity and Doppler temperature of the VUV lines are analyzed. Wavelengths of the measured VUV lines in several ionization stages (CIII-V, NeIII-IX, ArIII-VIII and ArXV-XVI) are accurately determined and tabulated including not only the allowed (E1) lines but also the forbidden (M1) lines for alternative passive spectroscopy. Self-absorption of VUV lines are found for hydrogen Lyman-series lines in high-density LHD discharges. Those lines are analyzed using the absorption equation. The spectroscopic data reported here are truly available to high-temperature plasma diagnostics.

**Table 3.1** Wavelength list of carbon lines. Symbol of 'b' in relative intensity means the line is blended with other lines.

Wavelength (Å)	Ion charge state	Order	Relative intensity	FWHM (pixels)	FWHM (Å)	Ion temperature (eV)
312.422	CIV	2	b			
312.453	CIV	2	b			
319.415	CIII	1	b			
369.472	CIII	1	b			
371.694	CIII	1	b			
371.747	CIII	1	b			
371.784	CIII	1	b			
384.031	CIV	3	b			
384.174	CIV	3	b			
386.2028	CIII	3	4.4	5.1	0.18	<5
419.525	CIV	2	b			
419.714	CIV	2	b			
459.462	CIII	2	b			
459.521	CIII	2	b			
459.633	CIII	2	b			
493.341	CIII	1	b			
493.364	CIII	1	b			
493.396	CIII	1	b			
493.464	CIII	1	b			
493.519	CIII	1	b			
493.587	CIII	1	b			
499.425	CIII	2	b			
499.462	CIII	2	b			
499.53	CIII	2	b			
499.583	CIII	2	b			

538.08	CIII	2	b				
538.1487	CIII	2	b				
538.312	CIII	2	b				
574.281	CIII	2	27.5	4.7	0.17	<5	
641.593	CII	1	b				
641.627	CII	1	b				
641.771	CII	1	b				
641.8	CII	1	b				
641.888	CII	1	b				
651.211	CII	1	b				
651.234	CII	1	b				
651.269	CII	1	b				
651.304	CII	1	b				
651.345	CII	1	b				
651.389	CII	1	b				
687.0526	CII	1	b				
687.3453	CII	1	b				
687.3521	CII	1	b				
806.384	CII	1	b				
806.533	CII	1	b				
806.568	CII	1	b				
806.676	CII	1	b				
806.686	CII	1	b				
806.83	CII	1	b				
806.86	CII	1	b				
858.092	CII	1	b				
858.559	CII	1	b				
903.6235	CII	1	b				
903.9616	CII	1	b				

904.1416	CII	1	b				
904.4801	CII	1	b				
977.02	CIII	1	2429.6	5.7	0.21	<5	
1009.858	CII	1	b				
1010.083	CII	1	b				
1010.371	CII	1	b				
1036.34	CII	1	b				
1037.02	CII	1	b				
1174.933	CIII	1	b				
1175.263	CIII	1	b				
1175.59	CIII	1	b				
1175.711	CIII	1	b				
1175.987	CIII	1	b				
1176.37	CIII	1	b				
1334.532	CII	1	1.6	5.1	0.18	<5	
1335.708	CII	1	3.5	5.4	0.19	<5	
1548.2	CIV	1	116.9	5.8	0.21	5±5	
1550.77	CIV	1	58.4	5.9	0.21	6±5	
2270.89	CV	1	27.4	15.7	0.56	106±12	
2277.27	CV	1	b				
2277.92	CV	1	b				

**Table 3.2** Wavelength list of neon lines. Symbol of 'b' in relative intensity means the line is blended with other lines.

Wavelength (Å)	Ion charge state	Order	Relative intensity	FWHM (pixels)	FWHM (Å)	Ion temperature (eV)
357.831	NeIV	2	b			
357.95	NeV	2	b			
358.48	NeV	2	b			
358.721	NeIV	2	b			
359.39	NeV	2	44.0	6.2	0.22	39±30
365.61	NeV	2	46.4	6.3	0.23	51±34
379.31	NeIII	2	6.8	6.0	0.22	13±13
387.141	NeIV	1	4.5	7.0	0.25	131±102
388.218	NeIV	1	7.5	6.6	0.24	37±37
399.82	NeVI	3	138.1	6.5	0.23	54±22
401.14	NeVI	3	269.9	6.4	0.23	51±21
401.93	NeVI	3	696.2	6.5	0.23	55±21
403.26	NeVI	3	153.0	6.7	0.24	77±26
416.20	NeV	3	0.7	6.3	0.23	33±18
416.82	NeV	3	4.8	6.4	0.23	45±23
421.609	NeIV	3	6.7	6.2	0.22	25±15
433.176	NeVI	2	b			
433.24	NeIV	2	b			
435.649	NeVI	2	54.4	6.7	0.24	61±21
451.843	NeVI	2	8.1	5.8	0.20	40±40
452.745	NeVI	2	15.7	6.5	0.23	175±77
454.072	NeVI	2	24.3	6.7	0.24	216±80
465.221	NeVII	2	976.1	7.2	0.26	347±93
469.773	NeIV	2	b			
469.82	NeIV	2	b			

469.866	NeIV	2	b				
469.921	NeIV	2	b				
480.41	NeV	2	20.3	6.3	0.23	103±50	
481.28	NeV	2	b				
481.36	NeV	2	b				
482.99	NeV	2	109.8	6.6	0.24	168±75	
488.10	NeIII	2	8.4	6.0	0.21	28±27	
488.87	NeIII	2	7.5	6.1	0.22	56±47	
489.5	NeIII	2	b				
489.64	NeIII	2	b				
490.31	NeIII	2	6.4	5.6	0.20	16±16	
491.05	NeIII	2	9.1	5.9	0.21	24±24	
521.741	NeIV	2	b				
521.820	NeIV	2	b				
541.127	NeIV	2	49.1	6.2	0.22	65±36	
542.073	NeIV	2	101.7	6.1	0.22	54±32	
543.891	NeIV	2	155.8	6.1	0.22	52±36	
558.59	NeVI	2	b				
558.61	NeVII	2	b				
559.947	NeVII	2	100.3	6.7	0.24	143±74	
561.378	NeVII	2	b				
561.728	NeVII	2	b				
562.80	NeVI	2	b				
562.992	NeVII	2	b				
564.529	NeVII	2	126.4	7.2	0.26	245±66	
568.42	NeV	2	73.9	6.4	0.23	90±42	
569.76	NeV	2	b				
569.83	NeV	2	b				
572.11	NeV	2	b				

572.34	NeV	2	b			
770.409	NeVIII	2	1021.6	7.0	0.25	112±31
780.324	NeVIII	2	492.0	7.0	0.25	108±30
895.18	NeVII	1	23.5	6.6	0.24	53±19
1006.1	NeVI	1	2.0	6.0	0.22	8±8
1010.6	NeVI	1	3.7	6.3	0.23	22±16
1248.28	NeIX	1	12.5	21.6	0.78	283±47

---

**Table 3.3** Wavelength list of argon lines. Symbol of 'ArUn' in ion charge state means the unclassified line and the ion charge in brackets after the 'ArUn' indicates possible ionization stage evaluated from the ion temperature. Symbol of 'b' in relative intensity means the line is blended with other lines.

Wavelength (Å)	Ion charge state	Order	Relative intensity	FWHM (pixels)	FWHM (Å)	Ion temperature (eV)
353.92	ArXVI	4	1.3	9.0	0.32	637±127
389.14	ArXVI	4	12.8	9.4	0.34	615±114
424.01	ArXV	3	16.4	9.2	0.33	480±119
436.67	ArV	3	96.0	6.7	0.24	119±61
443.40	ArIV	3	135.1	7.3	0.26	210±80
445.997	ArV	3	32.7	6.2	0.22	45±37
446.949	ArV	3	b			
447.53	ArV	3	b			
449.065	ArV	3	b			
449.49	ArV	3	b			
451.20	ArIV	3	b			
451.87	ArIV	3	b			
457.48	ArVI	3	41.3	6.9	0.25	144±64
462.0096	ArIV	3	b			
462.1373	ArIV	3	b			
473.938	ArVII	3	b			
475.654	ArVII	3	b			
475.73	ArVII	3	b			
479.379	ArVII	3	b			
479.49	ArVII	3	b			
486.60	ArUn (III)	3	56.3	6.2	0.22	40±32
495.55	ArIV	3	16.7	6.6	0.24	53±53
501.07	ArVII	3	74.0	7.0	0.25	138±57

508.44	ArIII	1	b			
519.43	ArVIII	3	68.9	6.9	0.25	111±50
524.19	ArV	1	b			
526.46	ArVIII	1	b			
527.69	ArV	1	15.7	6.5	0.23	60±35
544.73	ArVI	2	23.9	6.9	0.25	150±45
548.91	ArVI	2	41.2	6.9	0.25	93±43
551.37	ArVI	2	108.1	6.9	0.25	97±44
555.64	ArVI	2	b			
558.48	ArV	2	b			
585.73	ArVII	2	478.3	6.7	0.24	288±141
588.92	ArVI	1	16.5	6.5	0.24	214±121
589.78	ArVI	1	3.7	6.5	0.24	218±122
594.10	ArVI	2	6.2	6.7	0.24	258±132
596.69	ArVI	2	18.6	6.6	0.24	240±217
618.63	ArUn (VI-VIII)	1	8.4	6.5	0.23	194±110
619.04	ArUn (VI-VIII)	1	8.2	6.7	0.24	248±124
630.30	ArVII	2	b			
634.23	ArVII	2	23.4	6.6	0.24	217±113
635.15	ArV	2	5.0	6.9	0.25	293±131
637.05	ArVII	2	b			
637.28	ArIII	2	b			
637.47	ArVII	2	b			
641.36	ArIII	2	b			
641.32	ArVII	2	b			
641.81	ArIII	2	b			
643.25	ArIII	2	b			
644.37	ArVII	2	28.1	6.9	0.24	271±158
649.03	ArXII	1	7.3	9.5	0.34	1136±253

670.39	ArUn	1	b			
683.28	ArIV	2	14.8	6.5	0.23	159±90
689.01	ArIV	2	27.2	6.5	0.23	141±84
690.17	ArIII	2	b			
700.245	ArVIII	2	211.7	6.7	0.24	190±96
705.35	ArV	2	0.8	5.4	0.19	<50
709.20	ArV	2	7.3	6.8	0.25	220±102
713.812	ArVIII	2	94.9	6.9	0.25	221±101
715.60	ArV	2	b			
715.65	ArV	2	b			
725.11	ArV	2	11.1	6.5	0.23	134±78
754.93	ArVI	2	21.5	6.6	0.24	153±80
767.06	ArVI	2	34.1	6.8	0.25	184±78
767.71	ArVI	1	b			
801.09	ArIV	1	15.0	7.0	0.25	194±85
822.161	ArV	1	2.9	6.9	0.25	172±78
827.052	ArV	1	b			
827.35	ArV	1	b			
834.88	ArV	1	b			
840.03	ArIV	1	b			
843.765	ArIV	1	22.9	6.7	0.24	125±65
850.596	ArIV	1	35.6	6.7	0.24	134±66
871.100	ArIII	1	b			
875.530	ArIII	1	2.6	6.3	0.23	70±47
878.731	ArIII	1	11.4	6.6	0.24	108±58
879.62	ArIII	1	3.1	6.4	0.23	81±50
887.40	ArIII	1	b			

**Table 3.4** Line lists of carbon, neon and argon VUV lines useful to spectroscopic measurement.

Ion charge state	Ionization potential (eV)	Wavelength (Å)
CII	24	1334.5323, 1335.7077
CIII	48	977.02
CIV	65	1548.20, 1550.77
CV	392	2270.89
NeIII	63	379.31
NeIV	97	421.609
NeV	126	365.61
NeVI	158	435.649
NeVII	207	465.221
NeVIII	239	770.409, 780.324
NeIX	1196	1248.28
ArIII	41	878.731
ArIV	60	443.4
ArV	75	436.67
ArVI	91	551.37
ArVII	124	585.73
ArVIII	143	700.245, 713.812
ArXV	854	424.01
ArXVI	918	353.92, 389.14

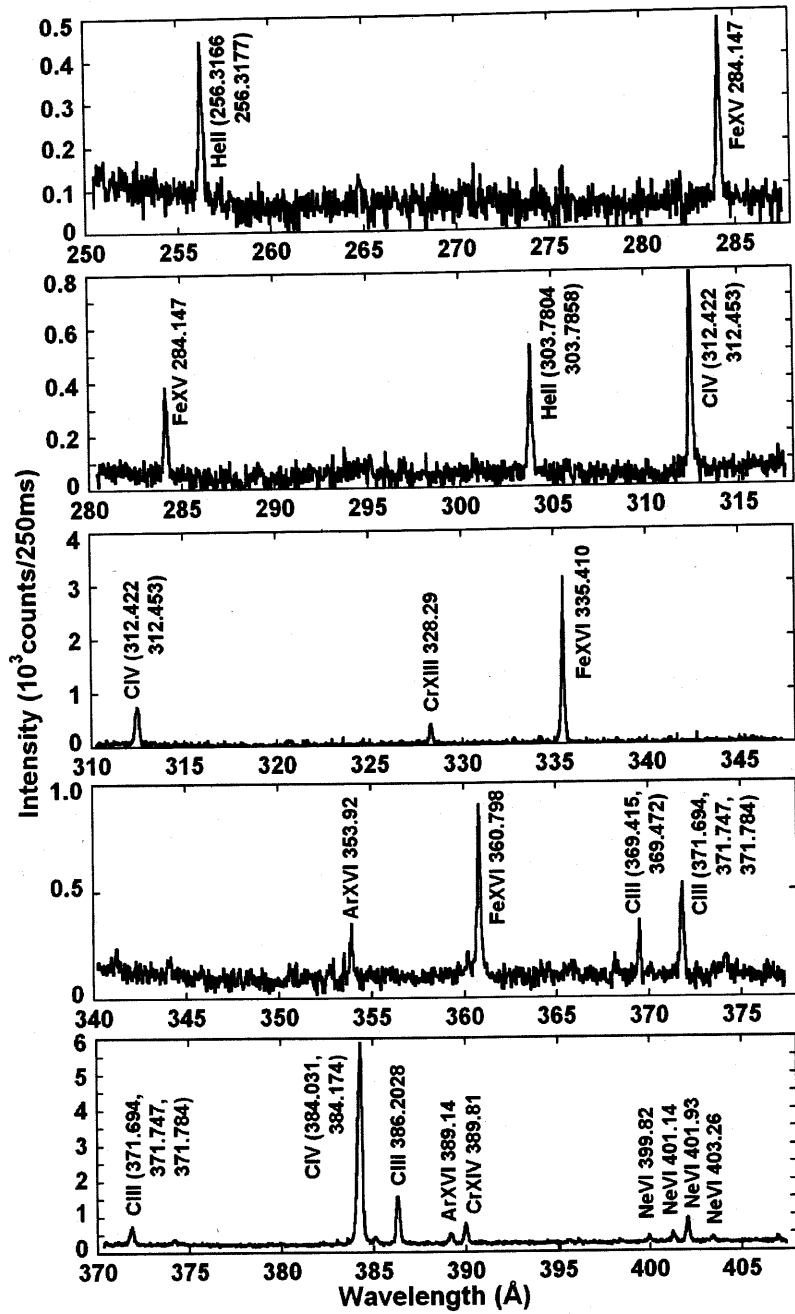


Fig. 3.1-1 VUV spectra from neon discharges.

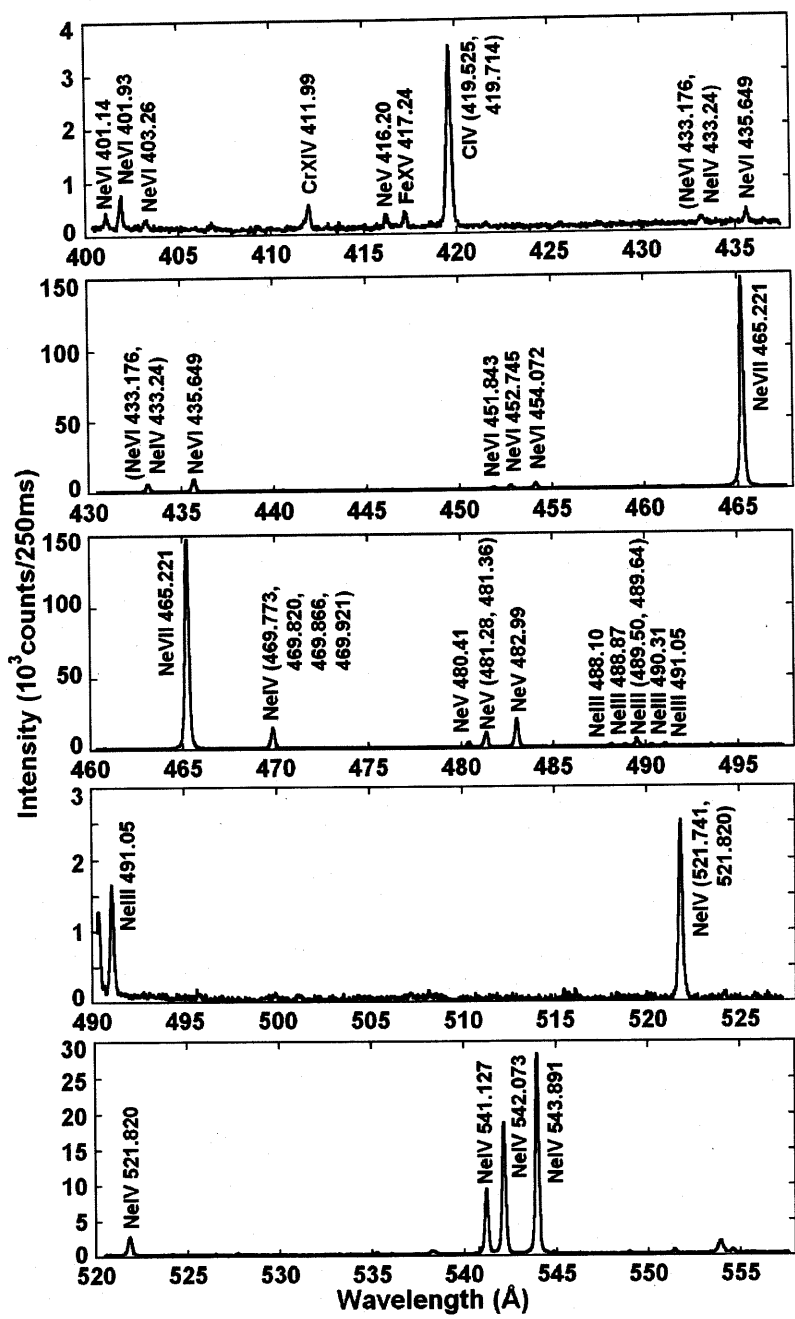


Fig. 3.1-2 VUV spectra from neon discharges.

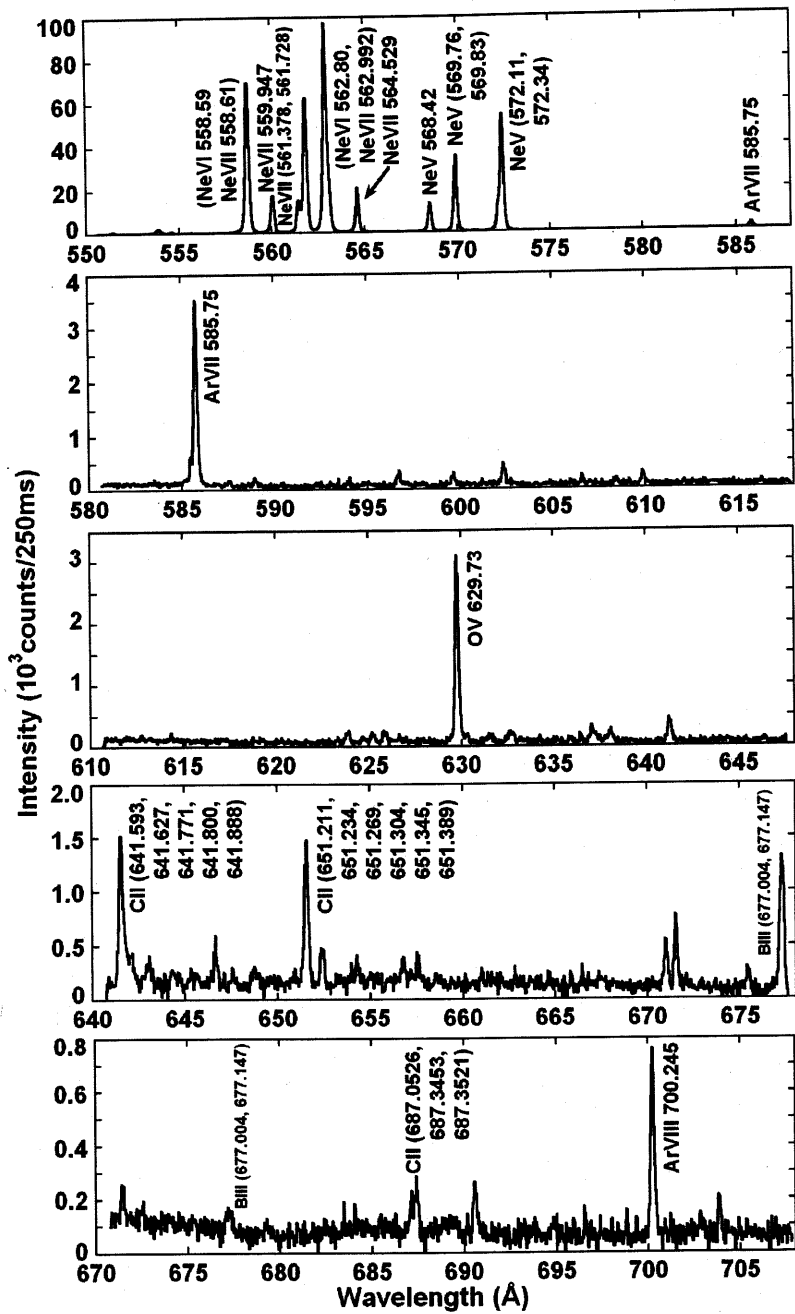


Fig. 3.1-3 VUV spectra from neon discharges.

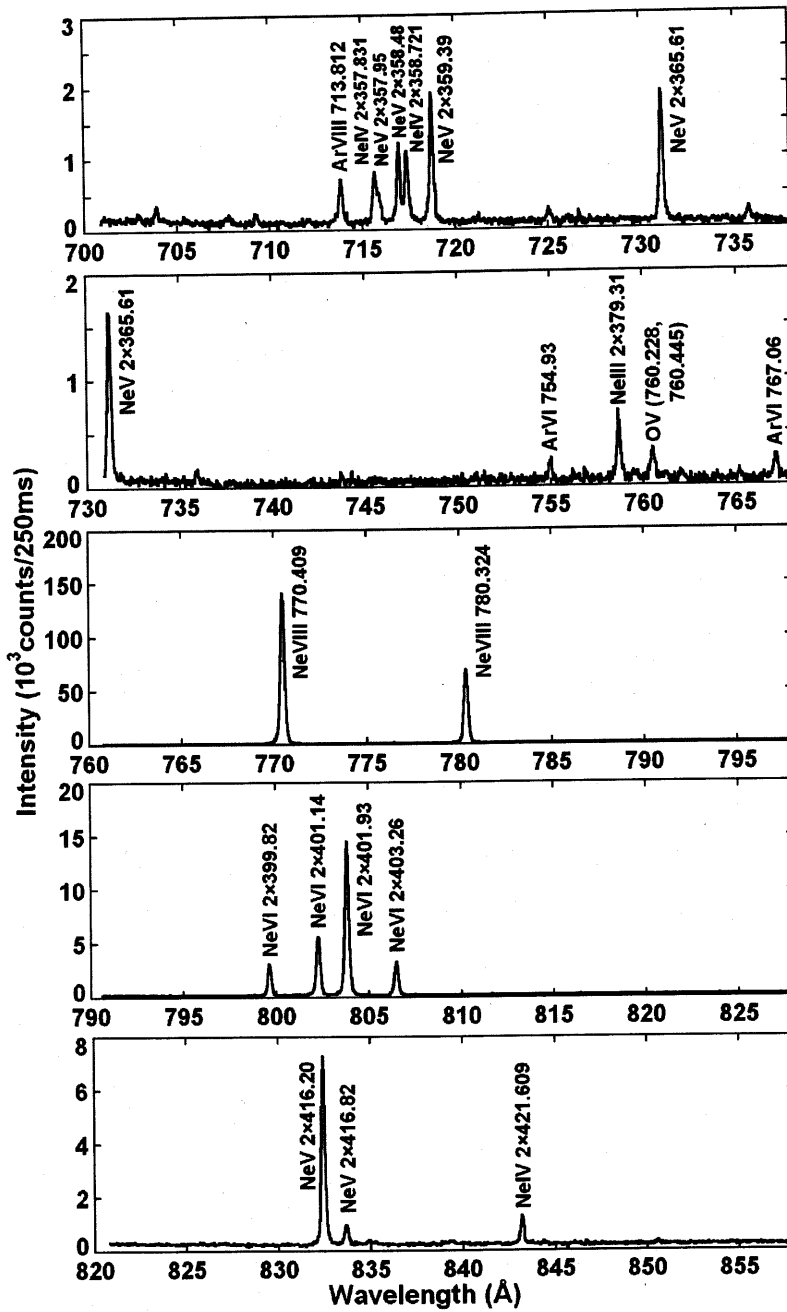


Fig. 3.1-4 VUV spectra from neon discharges.

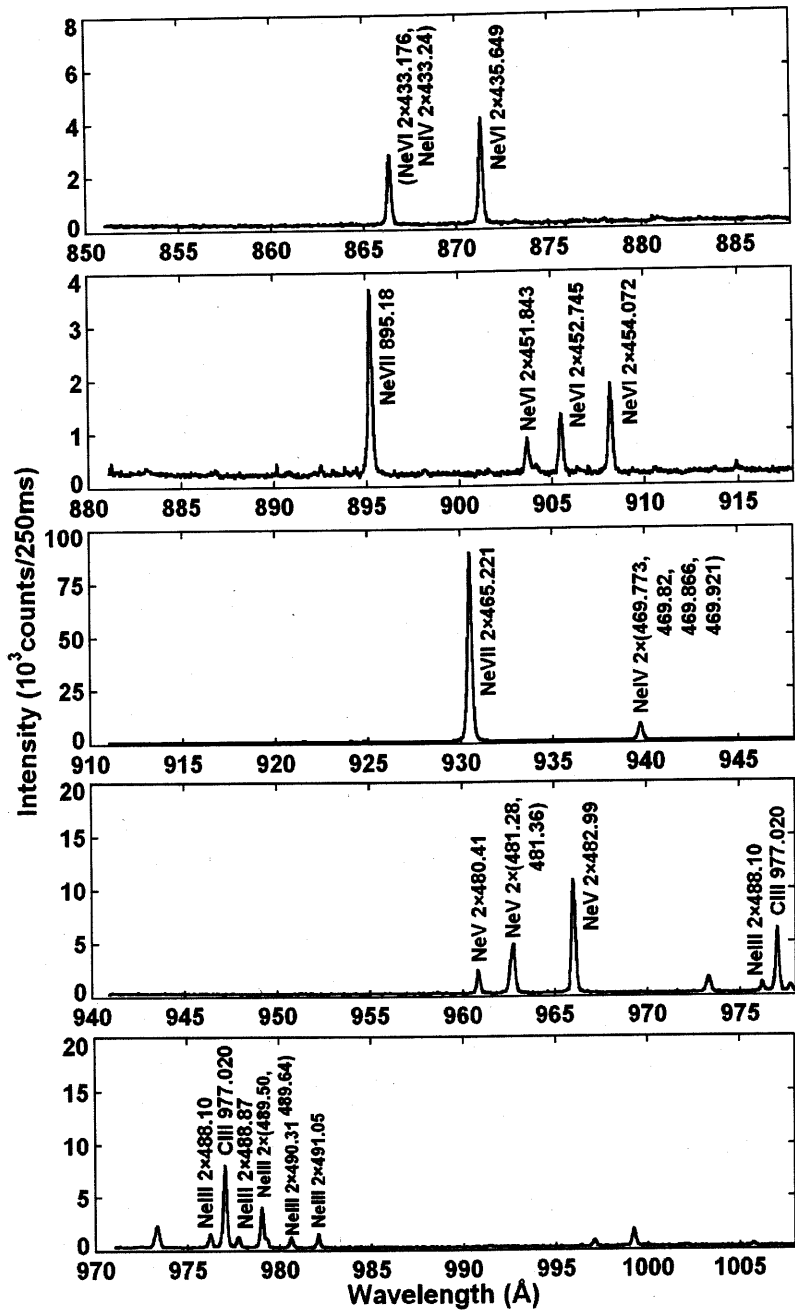


Fig. 3.1-5 VUV spectra from neon discharges.

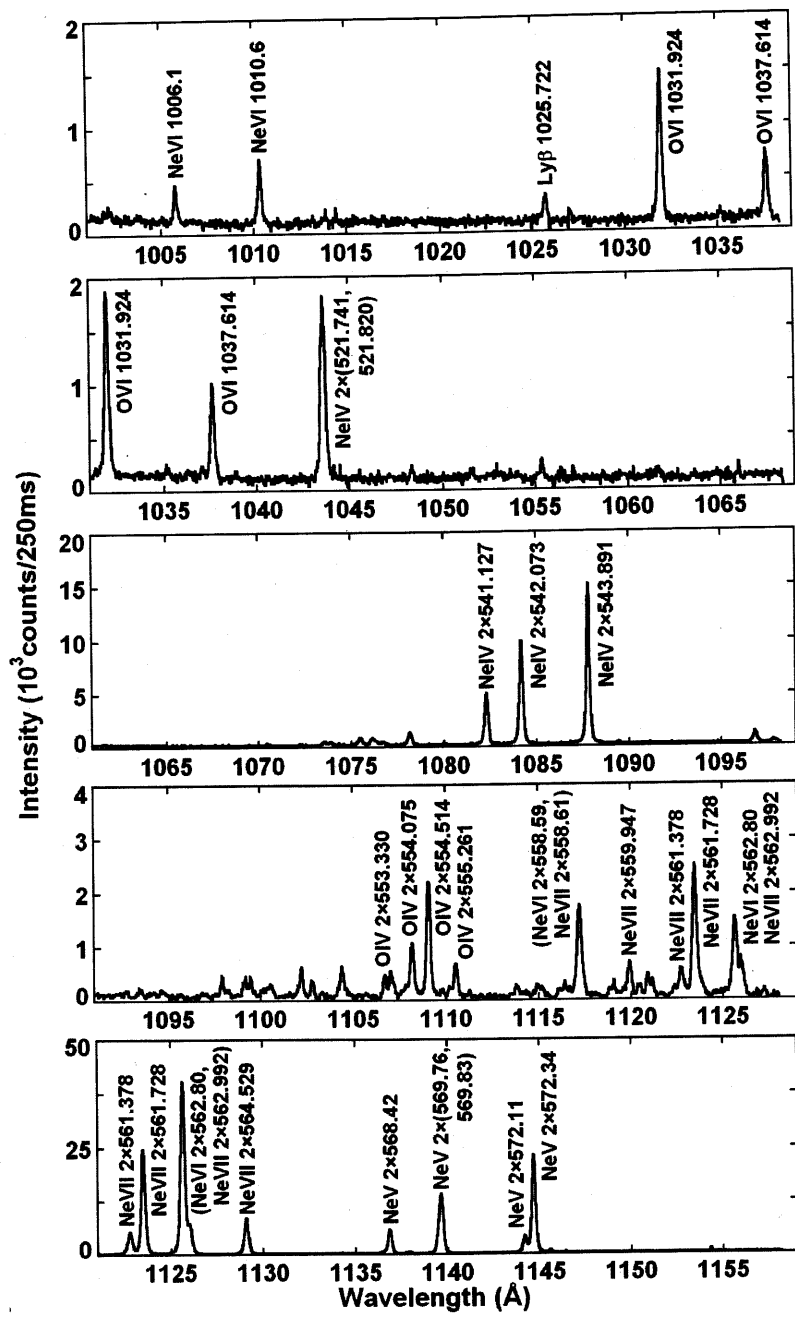


Fig. 3.1-6 VUV spectra from neon discharges.

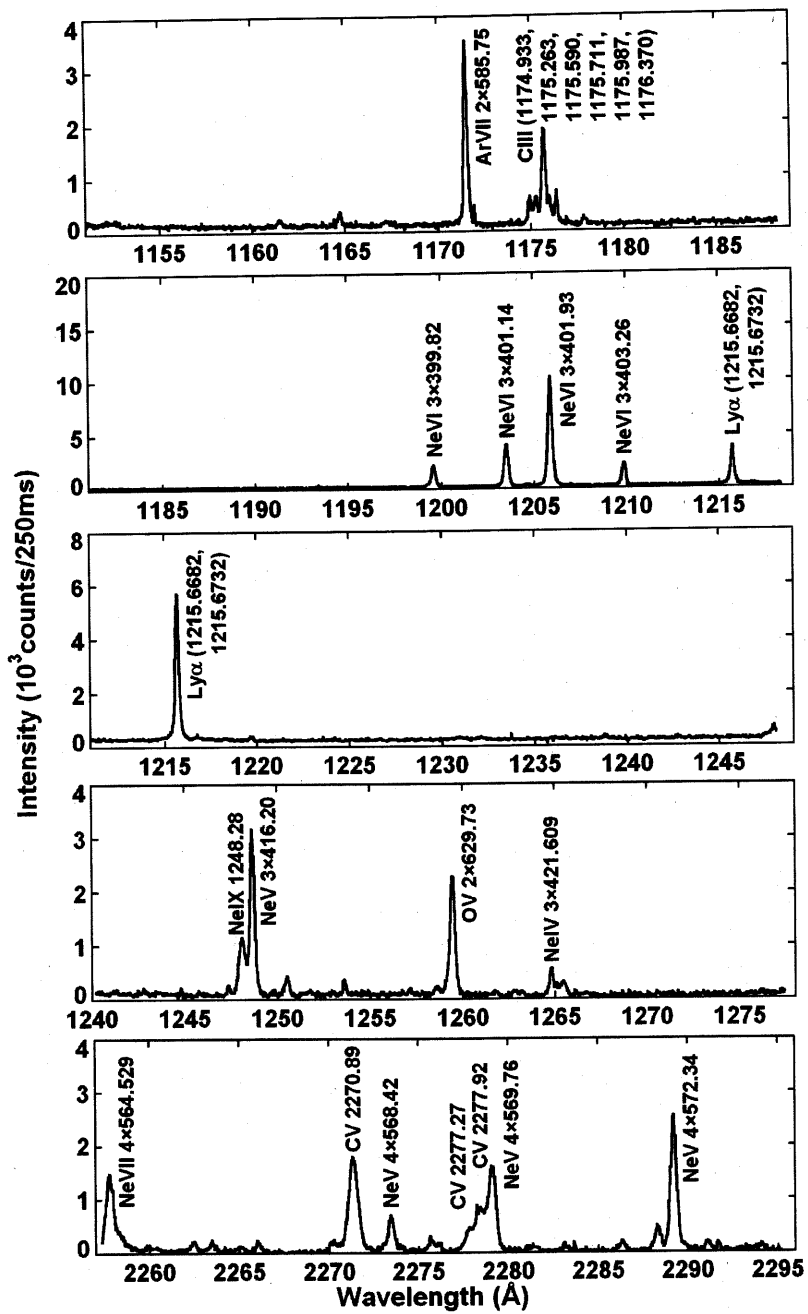


Fig. 3.1-7 VUV spectra from neon discharges.

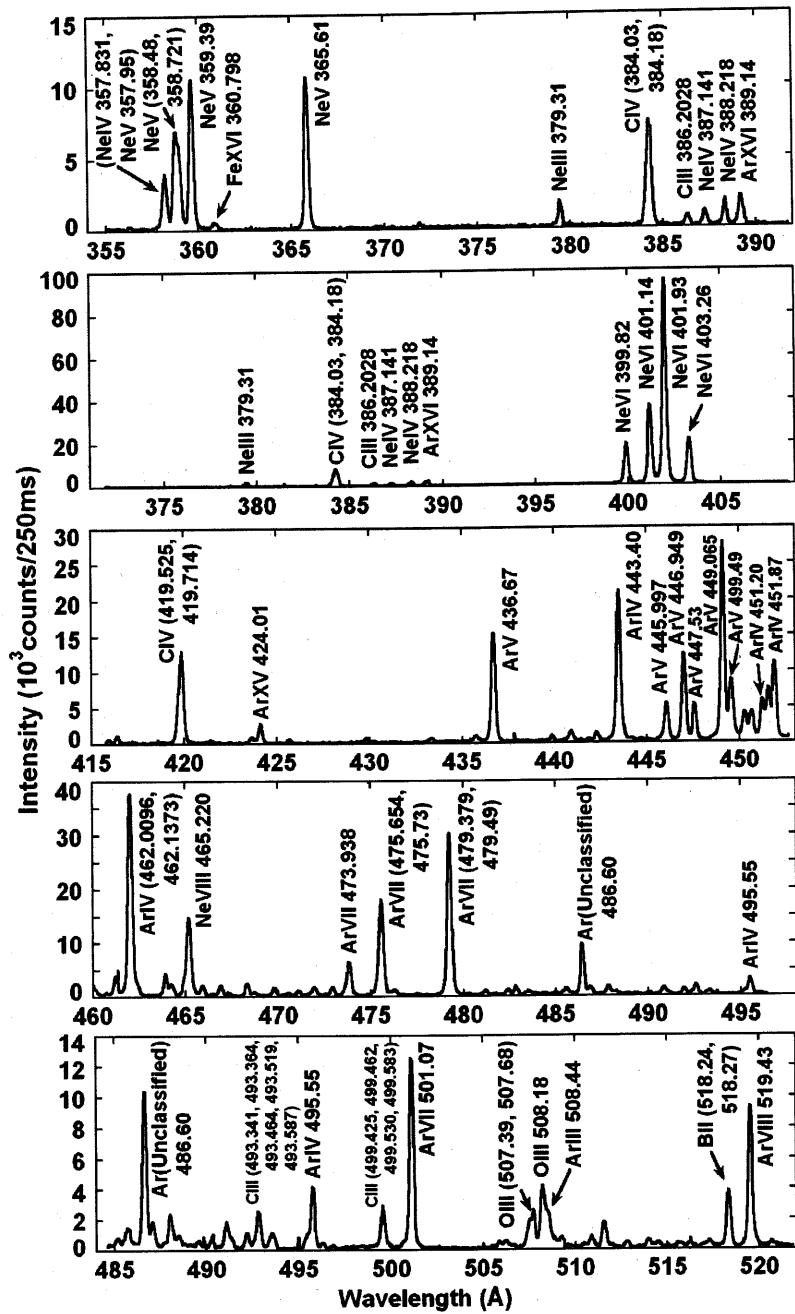


Fig. 3.2-1 VUV spectra from argon discharges.

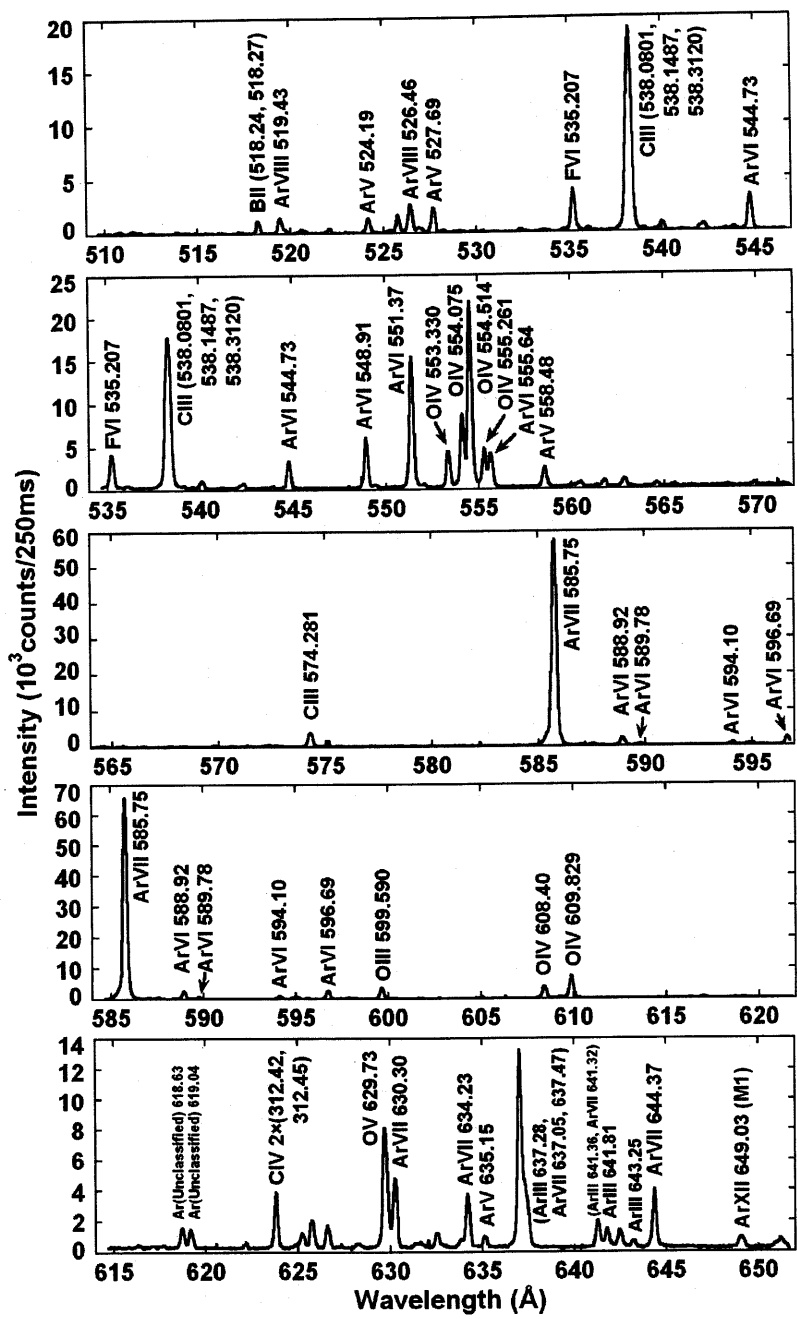


Fig. 3.2-2 VUV spectra from argon discharges.

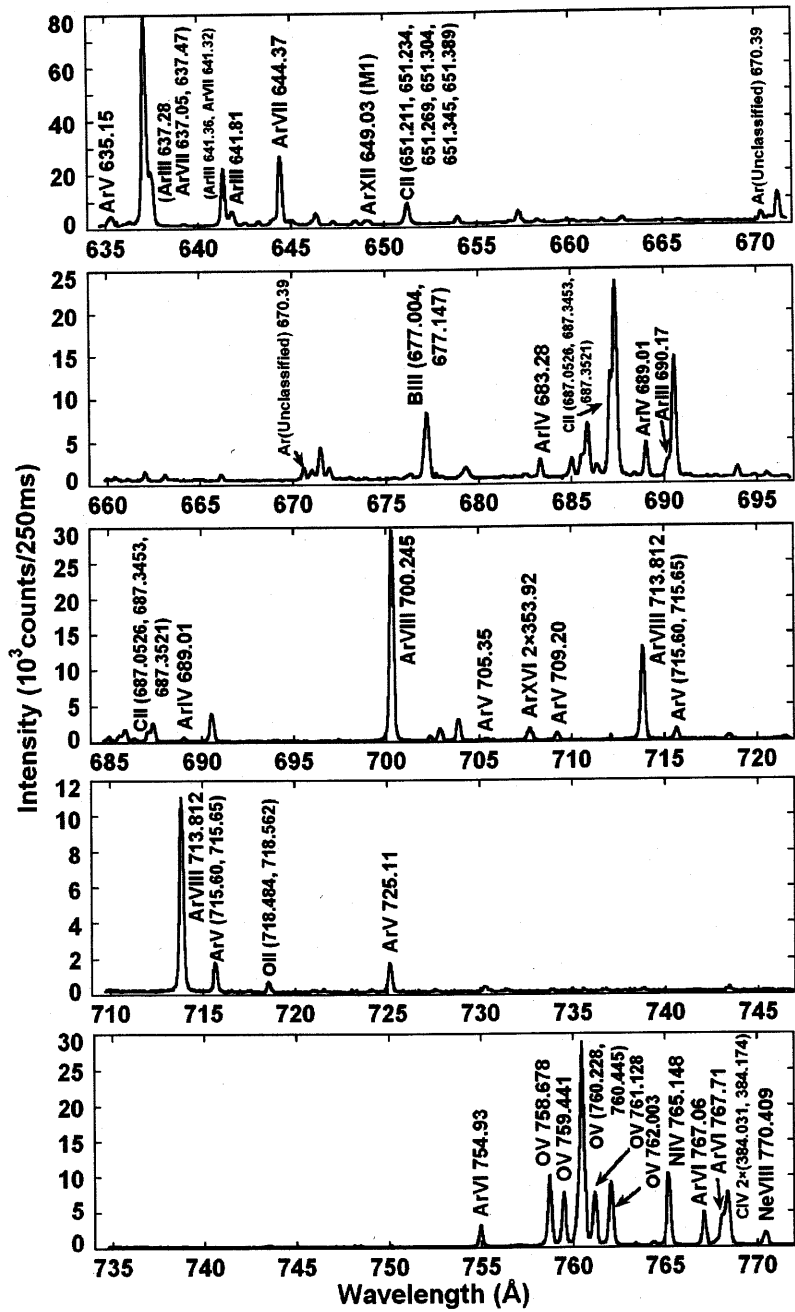


Fig. 3.2-3 VUV spectra from argon discharges.

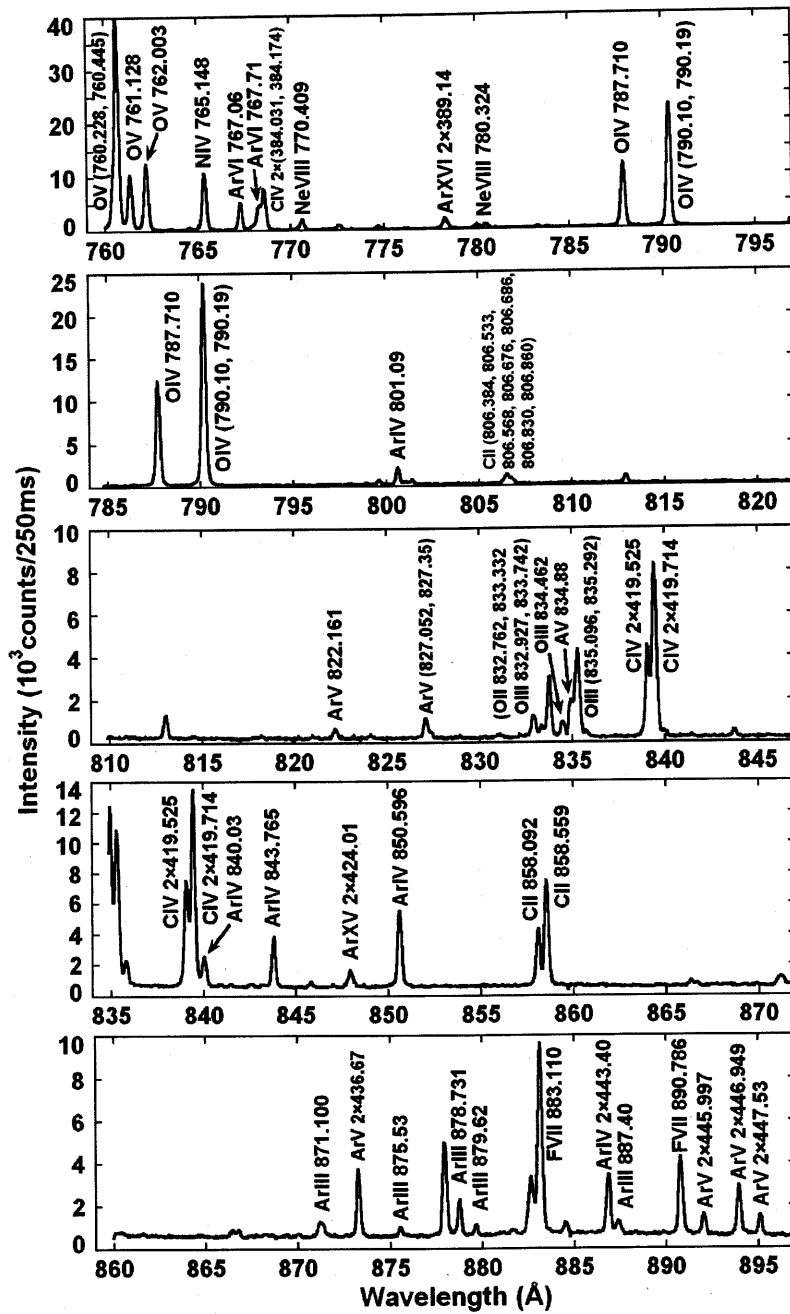


Fig. 3.2-4 VUV spectra from argon discharges.

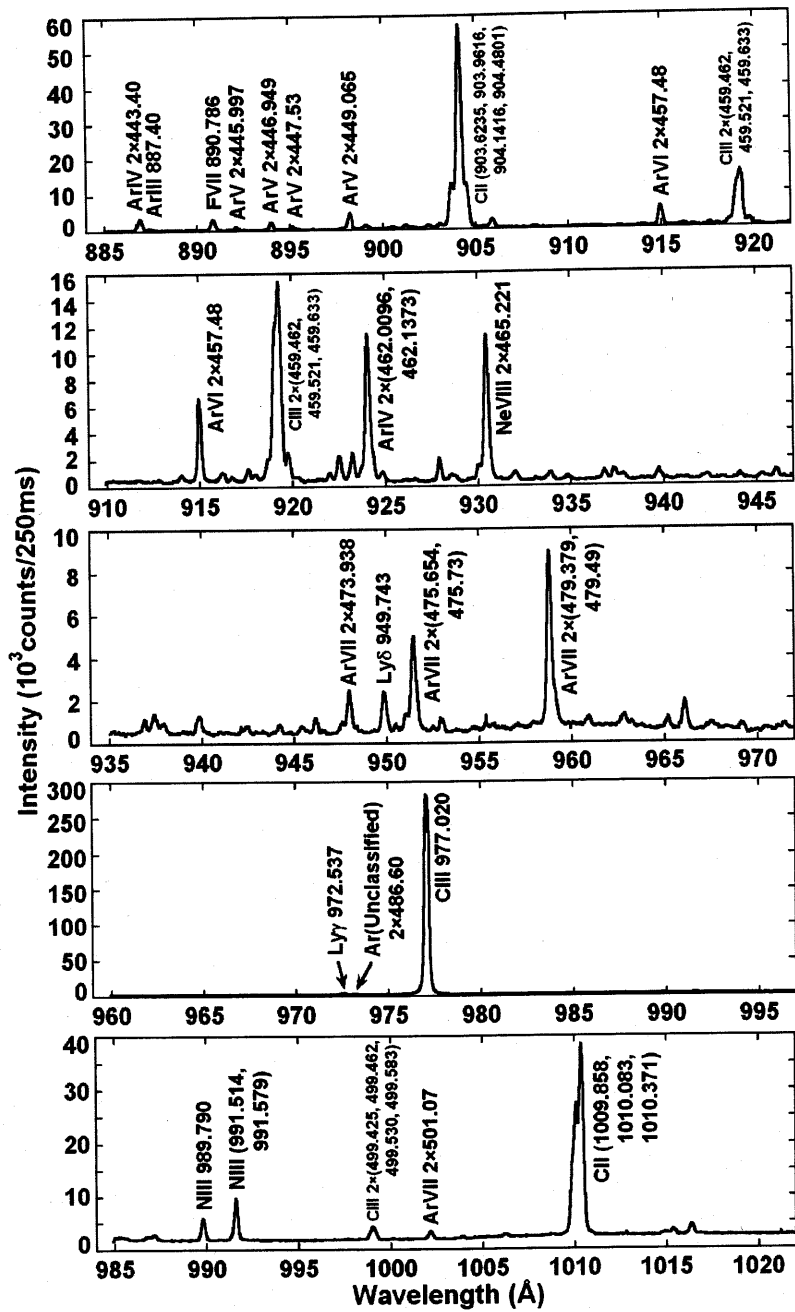


Fig. 3.2-5 VUV spectra from argon discharges.

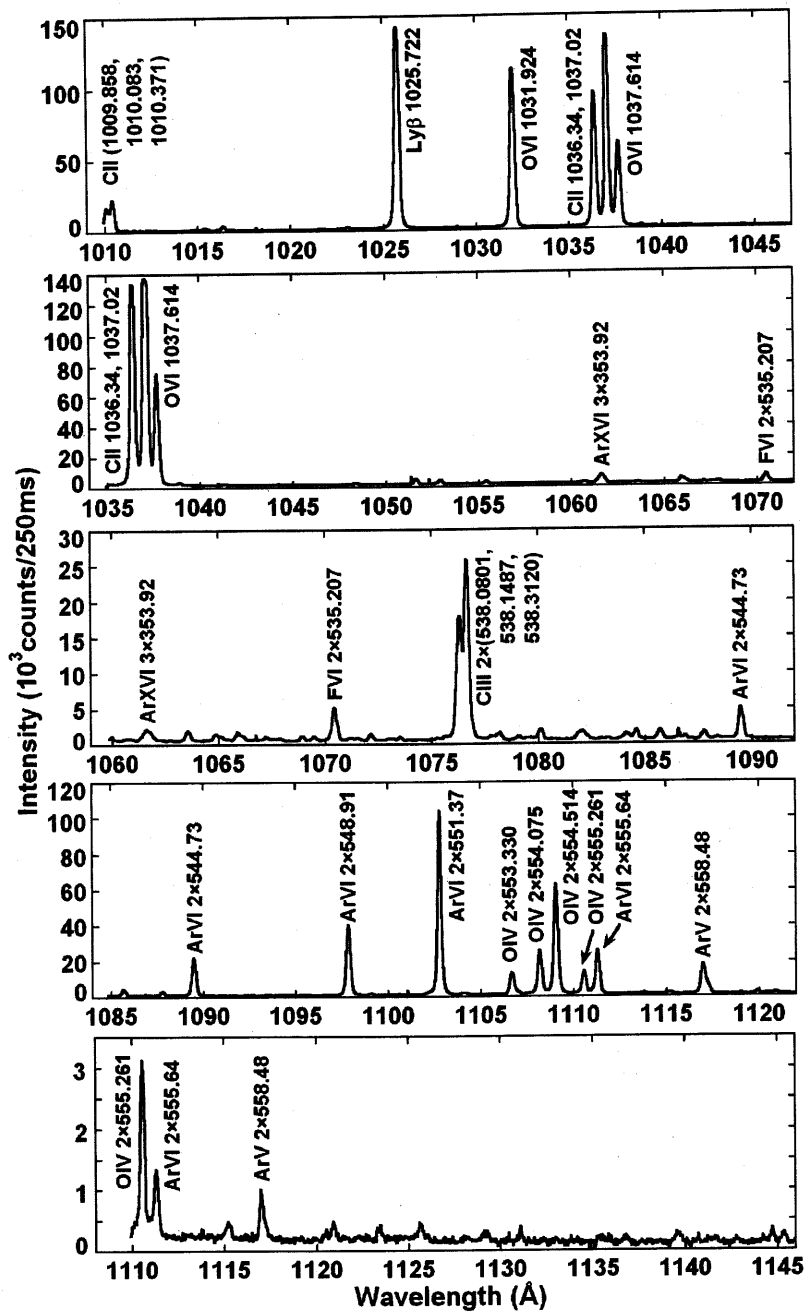


Fig. 3.2-6 VUV spectra from argon discharges.

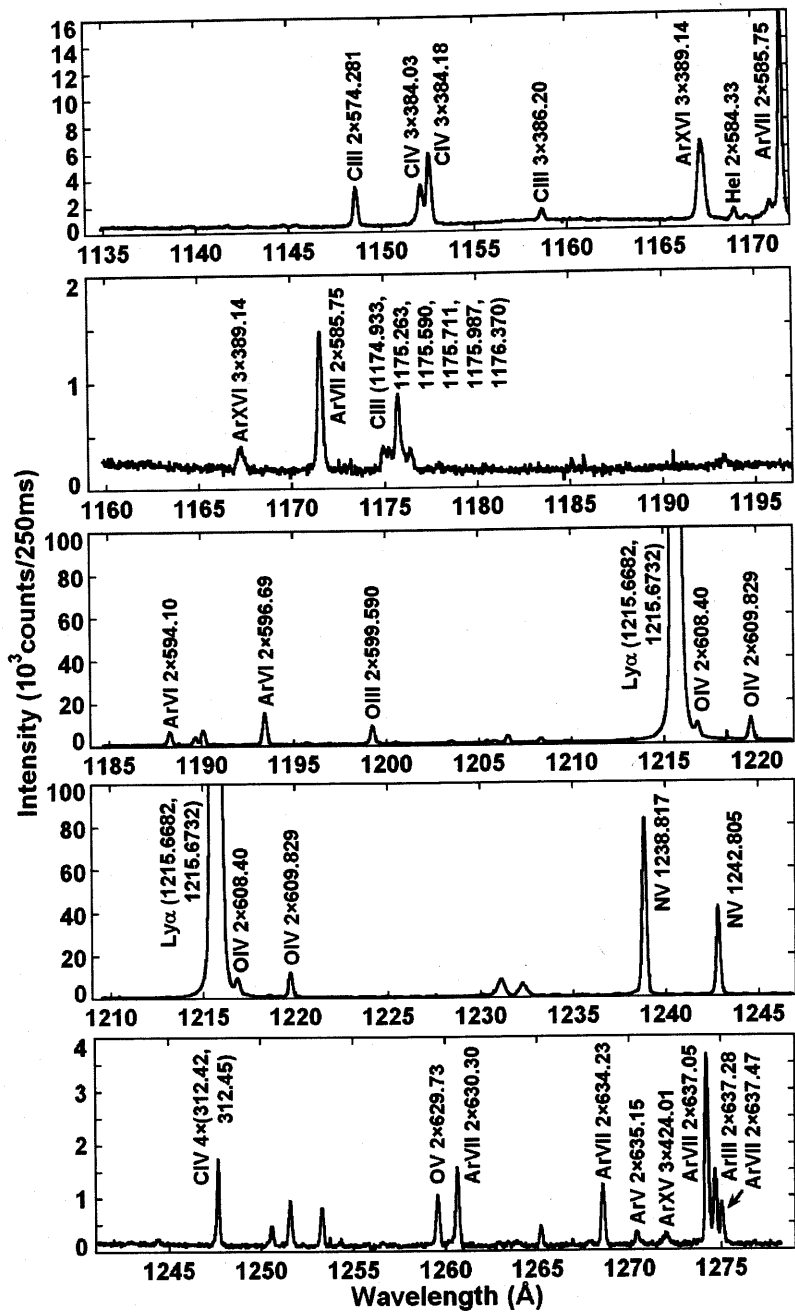


Fig. 3.2-7 VUV spectra from argon discharges.

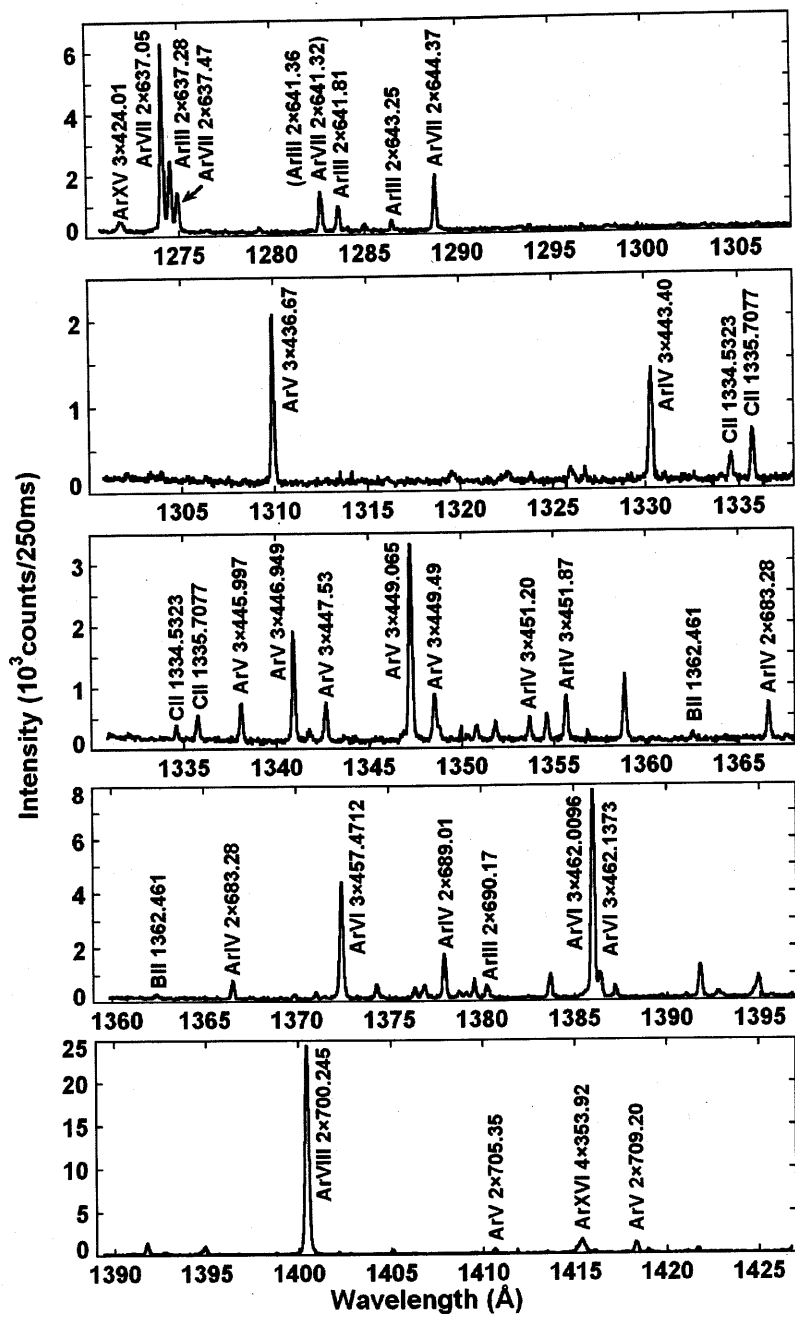


Fig. 3.2-8 VUV spectra from argon discharges.

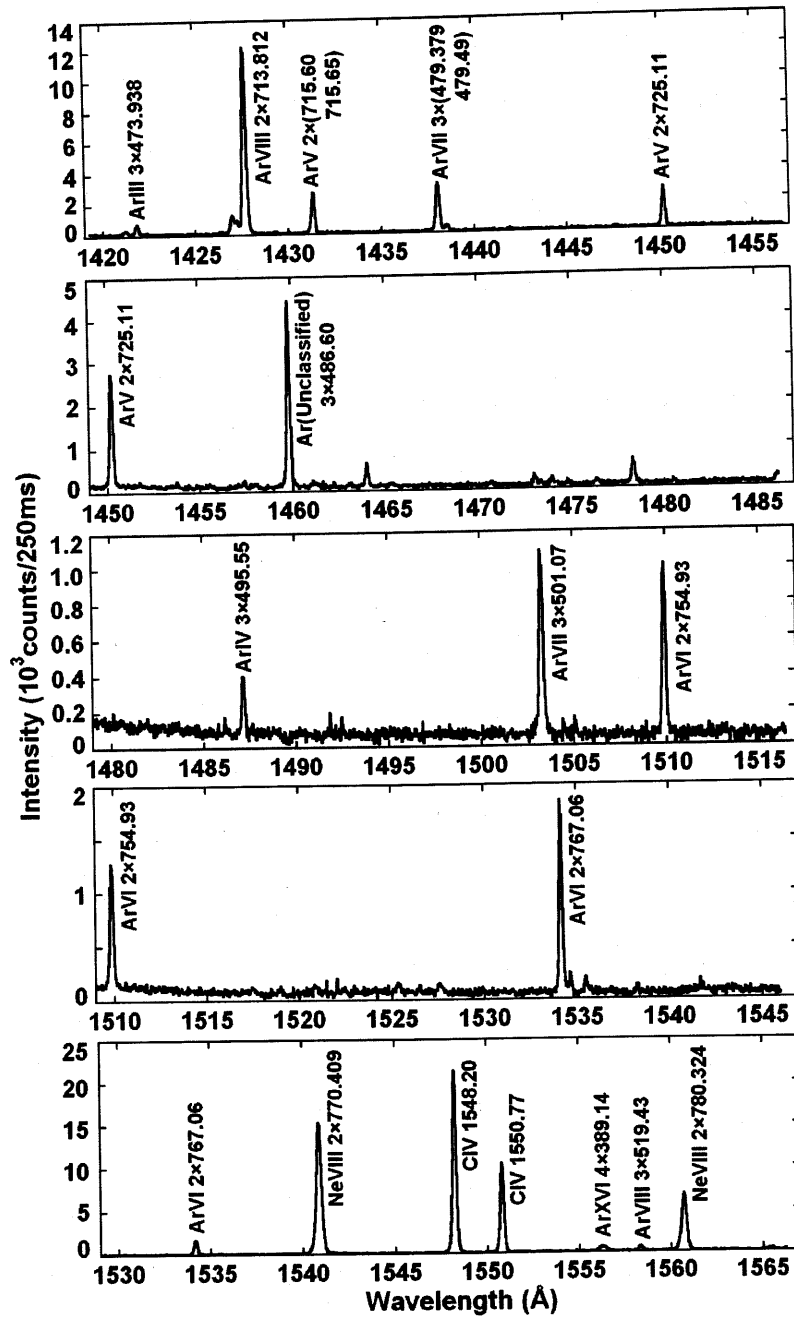


Fig. 3.2-9 VUV spectra from argon discharges.

## 3.2. Identification of M1 lines of Al, Ar, Ti and Fe

### 3.2.1. Introduction

Forbidden lines arising from magnetic dipole (M1) transitions of highly charged ions are interesting in diagnostic applications of magnetically confined fusion plasmas in addition to spectroscopic studies of the atomic structure. These M1 lines are generated by electron transitions in  $ns^2np^x$  ( $x = 1$  to  $5$ ) ground and  $nsnp$  ( $n = 2, 3$ ) excited configurations between the fine structure states of highly charged ions. The wavelength of the M1 line is longer than that of an allowed (E1) line in the same ionization stage. Some of the forbidden lines in highly charged ions of medium-Z impurities are emitted in the visible region. Spatial intensity profile and the Doppler broadening of such forbidden lines can be easily measured with the visible spectroscopy, which does not require any vacuum system and allows the use of optical fibers.

Several M1 transitions of highly charged ions have been studied in laboratory and astronomy plasmas [37]. The first measurement of the M1 transition in a fusion experimental device was made in the Princeton Large Torus tokamak [38]. Since then, many observations of the M1 lines from high-Z elements larger than  $Z=21$  have been done in magnetically confined plasmas to measure the wavelengths, impurity densities, ion temperatures and radial intensity profiles mainly in the visible region [37-46]. Although the M1 transitions with elements smaller than  $Z=28$  have been also observed from astronomy plasmas such as solar corona, nebula and several kinds of stars by using satellites in the visible and VUV region [47-50], the data quality from them are not quite enough, e.g., for the accurate determination of wavelength. Recently, the studies on the M1 transitions including argon ( $Z=18$ ) have been extensively done in the Electron Beam Ion Trap (EBIT) [51-55]. However, the data are mainly limited to the visible range, because the intensity of

M1 lines from the EBIT is very weak and a long exposure time is required to take a good signal to noise ratio.

In the Large Helical Device (LHD), to the contrary, argon discharges with high purity have been successfully operated without any instability and the argon emissions have been observed with strong intensities. Many M1 transitions of highly charged argon ions were found and identified in such argon discharges by analyzing their Doppler broadening, temporal behavior and spatial intensity distribution [56]. Furthermore, the M1 transitions from metallic elements have been also observed by injecting the impurity pellet [57]. The study on the M1 transition has been done not only in the visible region, but also in the VUV region using a 3m normal incidence spectrometer, since those lines are very bright. The wavelengths of the argon M1 transitions are accurately determined in the visible and VUV ranges.

In this section, the wavelengths of the M1 transitions carefully determined from aluminum, argon, titanium and iron spectral lines are presented and compared with previous experimental and theoretical works. Some of lines are newly identified in the present study.

### **3.2.2. Instrumentation**

Vacuum ultraviolet (VUV) spectra have been measured by using a space-resolved VUV system, which consists of a 3m normal incidence spectrometer with a 1200grooves/mm grating, charged-coupled device (CCD) detector (1024×1024pixels, 13μm×13μm/pixel) and a pair of mirrors for view-angle adjustment [58, 59]. Extreme ultraviolet (EUV) spectra have also been measured using a flat-field EUV spectrometer with the CCD detector [60].

Visible spectra have been measured using a 50cm Czerny-Turner type spectrometer (Chromex model 500is) equipped with CCD detector (1024×256pixels, 26μm×26μm/pixel). Low-resolution 100grooves/mm gratings were selected for monitoring a wider spectral band. High-resolution visible spectra have been measured using a 1.33m Czerny-Turner type

spectrometer equipped with an 1800grooves/mm grating and CCD detector [61]. The visible emission was collected by a focusing lens and transmitted by optical fibers with a core diameter of 100 $\mu$ m. The fibers installed on the diagnostic port were arranged vertically for measuring vertical distributions of the LHD plasma poloidal cross-section with a spatial resolution of 50 mm. The end of the fibers at the other side was coupled on the entrance slit of the visible spectrometer.

### 3.2.3. Identification of M1 transitions

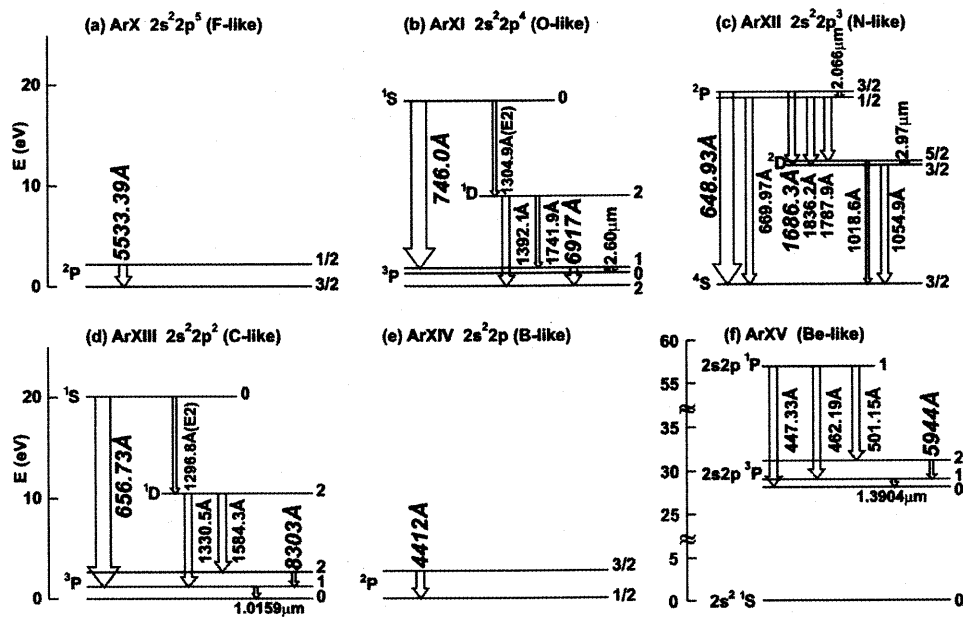


Fig. 3.8 Partial energy level diagram of M1 and E2 transitions in  $2s^2 2p^x$  ( $x=1$  to 5) ground and  $2s2p$  excited configurations of highly charged argon. Italic fonts indicate wavelength of M1 transitions observed in this work. The expression of E2 in bracket shows the E2 transition. Width of arrows represents relative amplitudes of spontaneous emission transition rates.

The partial energy level diagrams for the  $2s^2 2p^x$  ( $x=1$  to 5) ground state and  $2s2p$  excited state configurations of highly charged argon are illustrated in Fig. 3.8. Here, the possible

M1 and E2 transitions are also shown with the arrows. The width of the arrows represents the spontaneous transition probability. The wavelengths of the M1 and E2 lines have been calculated with the multi-configuration Dirac-Fock method [37]. The M1 lines observed in our experiment are indicated with the bold italic fonts. Several M1 lines in the first excited state configuration are observed, though the ground state of the Be-like ion consists of a singlet term and hence has no transitions in it. Since the F-like and B-like ions have only two fine-structures in the ground configuration, the detection of ArX 5533Å and ArXIV 4412Å becomes relatively easy.

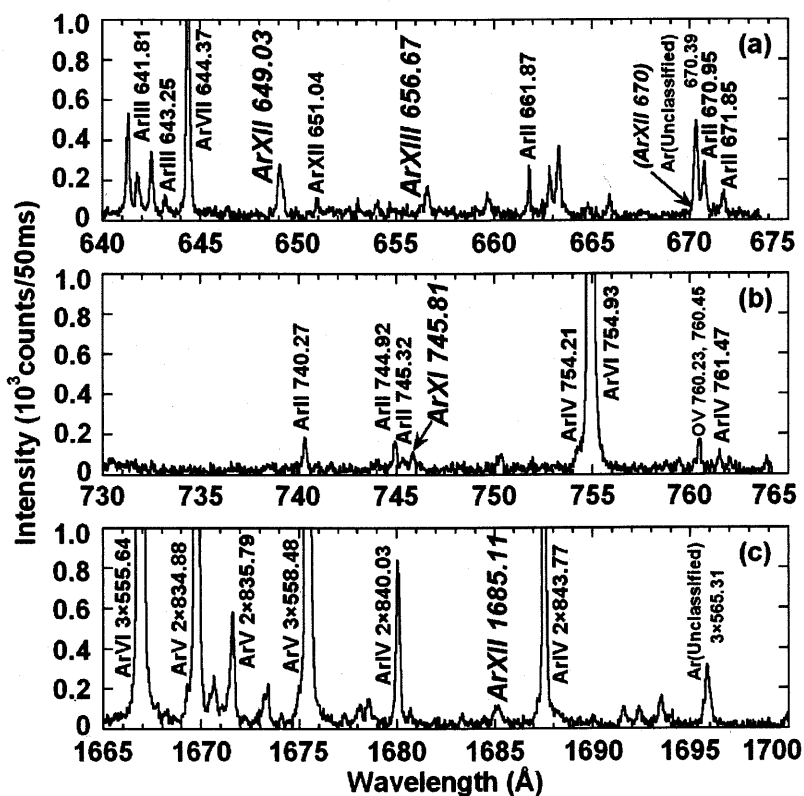


Fig. 3.9 VUV spectra from argon plasmas measured with 3m normal incidence spectrometer. Italic fonts indicate M1 lines observed in this work.

In the present observation four and five M1 lines in the VUV and visible wavelength ranges were identified, respectively. Figure 3.9 shows the examples of spectra obtained in

the VUV region for argon discharges. Most of the lines are identified to be E1 lines from relatively low ionization stage argon ions and only a few lines are considered to be M1 lines from highly ionized ions. In order to confirm our identification on the M1 lines, the Doppler broadening, temporal intensity behavior and spatial intensity distribution of the M1 lines were examined and compared with those of low ionization stage ions.

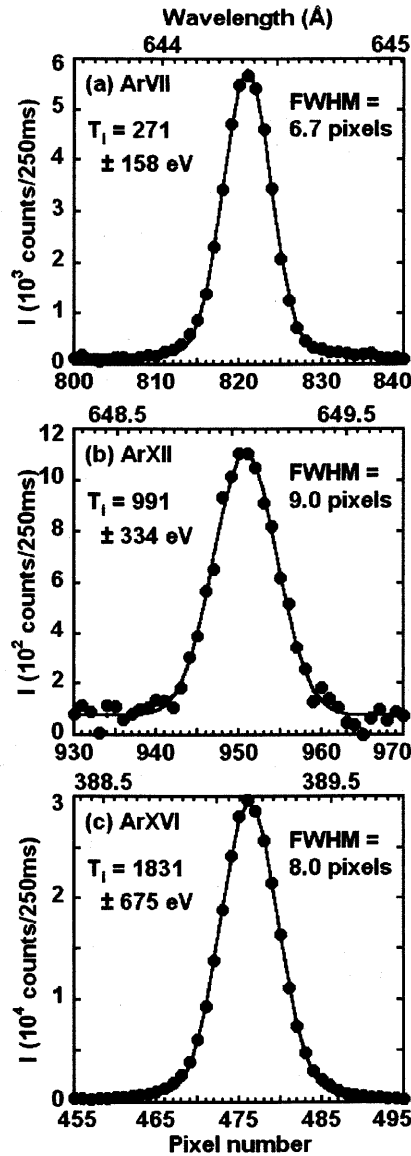
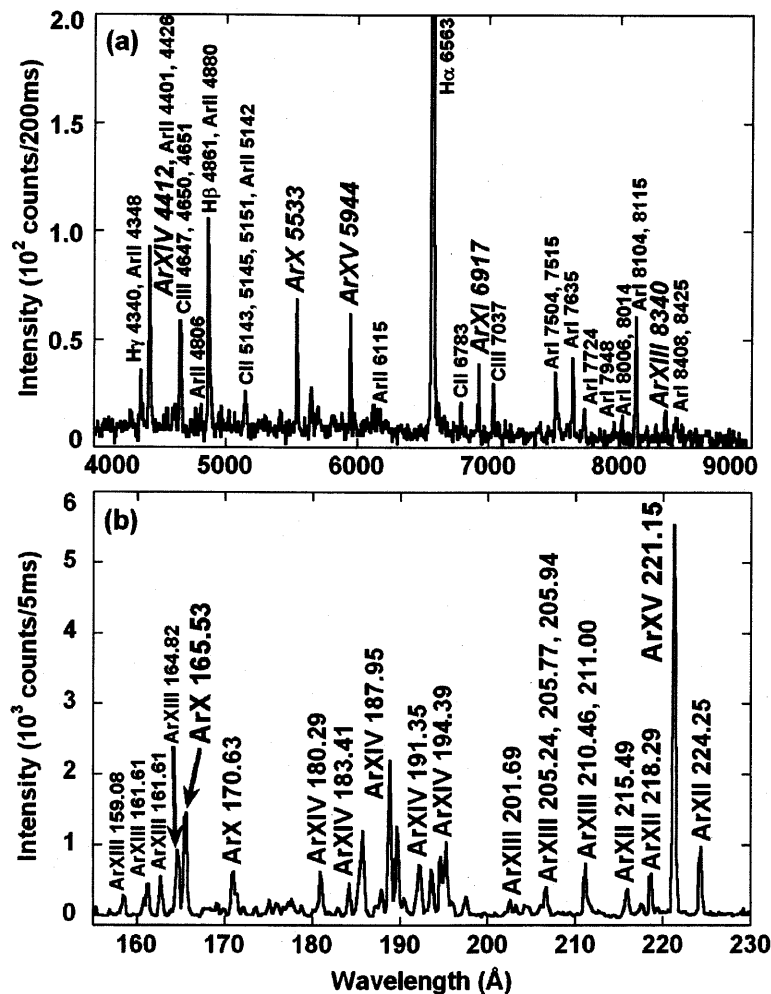


Fig. 3.10 Spectral profiles of (a) ArVII ( $3s3p\ ^3P_2 - 3p^2\ ^3P_1$ :  $644.37\text{\AA}$ , E1), (b) ArXII ( $2s^22p^3\ ^4S_{3/2} - ^2P_{3/2}$ :  $649.03\text{\AA}$ , M1) and (c) ArXVI ( $1s^22s\ ^2S_{1/2} - 1s^22p\ ^2P_{1/2}$ :  $389.14\text{\AA}$ , E1). Solid circles

indicate raw experimental data and solid lines are Gaussian fitting curve.

Figure 3.10 shows the Doppler broadening profiles of the ArVII E1 line ( $3s3p\ ^3P_2-3p^2\ ^3P_1$ : 644.37Å), ArXII M1 line ( $2s^22p^3\ ^4S_{3/2}-^2P_{3/2}$ :  $649.03\pm 0.02\text{Å}$ ), and ArXVI Li-like E1 line ( $1s^22s\ ^2S_{1/2}-1s^22p\ ^2P_{1/2}$ : 389.14Å). The instrumental width, the full width at half maximum (FWHM), of the 3 m normal incidence spectrometer is known to be  $5.7\pm 1.0$  pixels on the CCD detector, and the observed ArIII line has a similar width to the instrumental width. The measured ion temperature of ArVII ( $T_i=271\pm 158\text{eV}$ ) has a large error as shown in Fig. 3.10(a). In contrast, the widths of the ArXII and ArXVI lines are much broader than the instrumental width as shown in Fig. 3.10(b) and (c), and relatively high temperatures are obtained for ArXII ( $991\pm 334\text{eV}$ ) and ArXVI ( $1831\pm 675\text{eV}$ ). Furthermore, the ion temperature of ArXVI is a little higher than that of ArXII, reflecting a difference of ionization potentials (ArXII 618eV and ArXVI 918eV), which means the different radial location in the plasma. Using the same manner, the ArXI ( $2s^22p^4\ ^3P_1-^1S_0$ :  $745.81\pm 0.02\text{Å}$ ), ArXII ( $2s^22p^3\ ^2D_{3/2}-^2P_{3/2}$ :  $1685.11\pm 0.02\text{Å}$ ), and ArXIII ( $2s^22p^2\ ^3P_1-^1S_0$ :  $656.67\pm 0.02\text{Å}$ ) lines have also been identified as the M1 lines. The ArXII ( $2s^22p^3\ ^4S_{3/2}-^2P_{1/2}$ :  $670.34\pm 0.02\text{Å}$  [50]) line is also present in the spectra of Fig. 2(a) but that line is blended with Unclassified line of argon 670.39Å.

An example of visible spectra is shown in Fig. 3.11(a) indicating five M1 transitions of ArX ( $2s^22p^5\ ^2P_{3/2}-^2P_{1/2}$ : 5533Å), ArXI ( $2s^22p^4\ ^3P_2-^3P_1$ : 6917Å), ArXIII ( $2s^22p^2\ ^3P_1-^3P_2$ : 8340Å), ArXIV ( $2s^22p\ ^2P_{1/2}-^2P_{3/2}$ : 4412Å), and ArXV ( $2s2p\ ^3P_1-^3P_2$ : 5944Å). Some hydrogen and carbon lines are also identified. The ArXIV line is blended with two ArII lines in this low-resolution spectrum. The ArXI, ArXIV and ArXV wavelengths are precisely determined using reference lines of NeI (5944.834Å), ArII (4400.986Å and 4426.001Å), and BII ( $2\times 3451.287\text{Å}$ ) and NeI (6929.467Å), respectively. The two M1 lines of ArX and ArXV are isolated from other lines having a strong intensity. Then, intensity analysis was used those visible M1 lines with resonance lines (ArX  $2s^22p^5\ ^2P_{3/2}-2s2p^6\ ^2S_{1/2}$ : 165.53Å and ArXV  $2s^2\ ^1S_0-2s2p\ ^1P_1$ : 221.15Å) in EUV spectra (see Fig. 3.11(b) and chapter 4).



**Fig. 3.11** (a) Visible spectrum from argon plasmas measured with 50cm Czerny-Turner spectrometer. *Italic fonts indicate M1 lines observed in this work.* (b) EUV spectrum measured with flat-field spectrometer.

The M1 transitions of ArX-XV were compared with previous works. Results are listed in Table 3.5 with experimentally obtained and theoretically calculated values in other works. Wavelengths of the Ar M1 transitions in the VUV range are newly determined here with high accuracy as the experimental value. For example, the wavelength of ArXII VUV line

is determined as presented in the table and the measured wavelength of  $649.03 \pm 0.02 \text{ \AA}$  shows a good agreement with the theoretical value of  $648.93 \pm 0.27 \text{ \AA}$ . The ArXIII ( $8340 \pm 3 \text{ \AA}$ ) does not have other experimental data for comparison. The ArX ( $5533 \pm 2 \text{ \AA}$ ) and ArXIII ( $8340 \pm 3 \text{ \AA}$ ) have no good accuracy because the low-resolution gratings were used for the observation. Four visible lines of ArX, ArXI, ArXIV and ArXV have been already investigated with high-precision measurement by EBIT [51]. The present work on the five lines also shows an excellent agreement with the previous results.

Observation of the M1 transition from medium-Z metallic elements was done by injecting metallic pellets into the LHD plasmas using an impurity pellet injector [57]. The metallic impurity pellets of cylindrical aluminum of  $0.8 \text{ mm}^\phi$  in diameter and  $0.8 \text{ mm}^L$  in length, cylindrical titanium of  $0.5 \text{ mm}^\phi \times 0.4 \text{ mm}^L$  and hemisphere stainless (iron) of  $0.5 \text{ mm}^\phi \times 0.3 \text{ mm}^L$  were used in the present study. The velocity of the pellets ranged in 200-300 m/s and the pellets were ablated at half radius of the plasma. Line radiations from the injected metallic ions continue during 100-200 ms with a temporal behavior after the pellet injection. Figure 3.12 shows VUV spectra including the M1 transitions of metallic ions such as aluminum, titanium and iron. Identified M1 transitions are indicated by bold italic fonts with their wavelengths. These results are listed in Table 3.6. The M1 VUV lines arising from the same configuration of  $2s^2 2p^2 \ ^3P_1 - ^1S_0$  are measured at AlVIII  $1058.02 \pm 0.02 \text{ \AA}$ , ArXIII  $656.67 \pm 0.02 \text{ \AA}$  and TiXVII  $470.69 \pm 0.02 \text{ \AA}$  with a good accuracy. Wavelengths of almost all the M1 transitions determined here are successfully improved through the present work. The M1 transitions of ArX  $5533 \text{ \AA}$ , TiXIV  $2118.15 \text{ \AA}$  and FeXVIII  $974.85 \text{ \AA}$  appearing from the same configuration of  $2s^2 2p^5 \ ^2P_{3/2} - ^2P_{1/2}$  are used in the analysis on line intensity ratios mentioned in the chapter 4.

### 3.2.4. Summary

Forbidden lines originated in magnetic dipole (M1) transitions of highly charged Al, Ar, Ti and Fe ions were measured in LHD. Several VUV and visible lines are identified as the

M1 transition by analyzing the Doppler broadening, temporal intensity behavior and spatial intensity dependence. Wavelengths of these M1 transitions were determined with high accuracy and have a good agreement with previous experimental and calculated values.

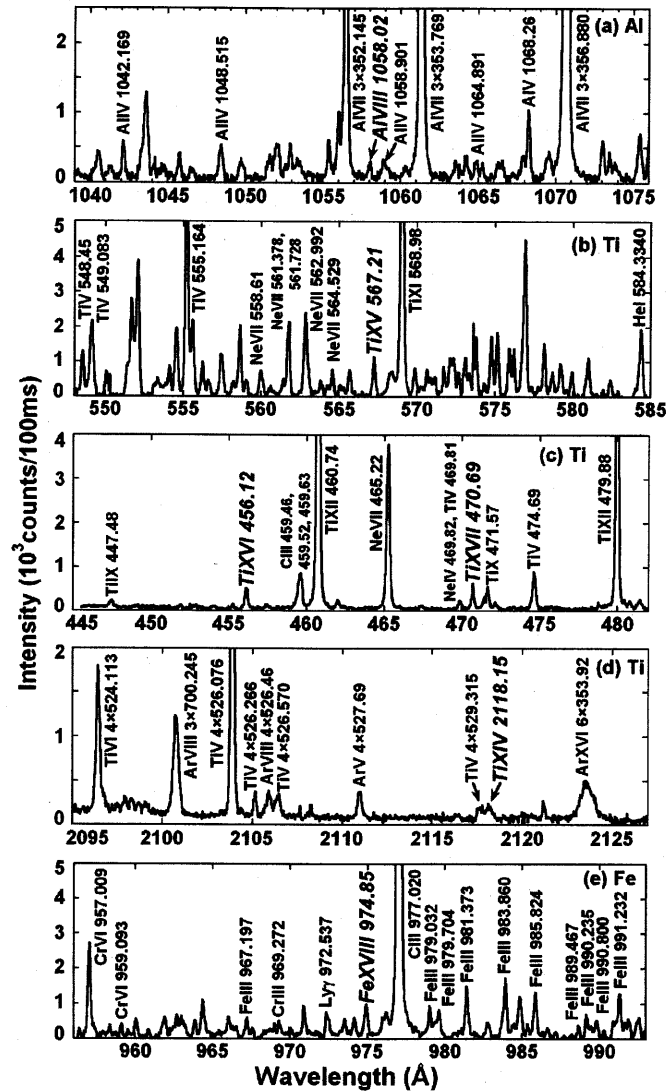


Fig. 3.12 VUV spectra from impurity pellet injected plasmas measured using 3m normal incidence spectrometer. (a) Al pellet, (b-d) Ti pellet and (e) Fe pellet. *Italic fonts indicate M1 lines observed in this work.*

**Table 3.5** Wavelengths of Ar M1 transitions determined from the present work in comparison with previous data.

Spectra	Transitions	Observed wavelengths (Å)		Calculated
		This work	Others	wavelengths (Å)
ArXI <sup>a</sup>	$2s^2 2p^4 \ ^3P_1 - ^1S_0$	745.81±0.02	745.80±0.02 [50]	746.0±0.4 [37] 745.95 [65]
ArXII <sup>a</sup>	$2s^2 2p^3 \ ^4S_{3/2} - ^2P_{3/2}$	649.03±0.02	650 [63] 649 [50]	648.93±0.27 [37]
ArXII <sup>a</sup>	$2s^2 2p^3 \ ^2D_{3/2} - ^2P_{3/2}$	1685.11±0.02	1687 [63]	1686.3±1.8 [37]
ArXIII <sup>a</sup>	$2s^2 2p^2 \ ^3P_1 - ^1S_0$	656.67±0.02	656.67±0.02 [50]	656.73±0.28 [37] 656.69 [64]
ArX <sup>b</sup>	$2s^2 2p^5 \ ^2P_{3/2} - ^2P_{1/2}$	5533±2	5533.265±0.002 [50] 5533.4±0.13 [62]	5533.39±0.21 [37] 5534.0 [64, 66]
ArXI <sup>b</sup>	$2s^2 2p^4 \ ^3P_2 - ^3P_1$	6916.88±0.02	6916.878±0.012 [51] 6916.86±0.06 [53]	6931±24 [37] 6917[64] 6916 [65]
ArXIII <sup>b</sup>	$2s^2 2p^2 \ ^3P_1 - ^3P_2$	8340±3	4412.559±0.001 [51]	8303±40 [37] 4416±4 [37]
ArXIV <sup>b</sup>	$2s^2 2p \ ^2P_{1/2} - ^2P_{3/2}$	4412.57±0.02	4412.50±0.03 [53] 4412.6±0.08 [54]	4412.2[64] 4413.2 [67]
ArXV <sup>b</sup>	$2s 2p \ ^3P_1 - ^3P_2$	5943.87±0.02	5943.880±0.005 [51] 5943.73±0.04 [53]	5944±25 [37] 5943.7 [64]

<sup>a</sup>in vacuum    <sup>b</sup>in air

**Table 3.6** Wavelengths of M1 transitions determined from the present work in comparison with previous data.

Spectra	Transitions	Observed wavelengths (Å)		Calculated
		This work	Others	wavelengths (Å)
AlVIII <sup>a</sup>	$2s^2 2p^2 \ ^3P_1 - ^1S_0$	1058.02±0.02	1058 [63]	1058.0±0.7 [37]
				1057.6 [64]
TiXV <sup>a</sup>	$2s^2 2p^4 \ ^3P_1 - ^1S_0$	567.21±0.02	567.42 [63]	567.41±0.16 [37]
				567.41 [64]
TiXVI <sup>a</sup>	$2s^2 2p^3 \ ^4S_{3/2} - ^2P_{3/2}$	456.12±0.02	456.1±0.3 [37]	456.10±0.05 [37]
			456.1 [63]	456.10 [64]
TiXVII <sup>a</sup>	$2s^2 2p^3 \ ^3P_1 - ^1S_0$	470.69±0.02	470.4±0.3 [37]	470.54±0.11 [37]
			470.60 [63]	470.54 [64]
TiXIV	$2s^2 2p^5 \ ^2P_{3/2} - ^2P_{1/2}$	2118.15±0.02 <sup>a</sup>	2117.1±0.2 <sup>b</sup> [37]	2117.12±0.18 <sup>b</sup> [37]
TiXVI <sup>b</sup>	$2s^2 2p^3 \ ^2P_{1/2} - ^2P_{3/2}$	4637±2	4635.6±0.3 [37]	4639±5 [37]
TiXVII <sup>b</sup>	$2s^2 2p^2 \ ^3P_0 - ^3P_1$	3370.92±0.02	3370.8±0.2 [37]	3370.80±0.23 [37]
TiXVII <sup>b</sup>	$2s^2 2p^3 \ ^3P_1 - ^3P_2$	3834.91±0.02	3834.4±0.2 [37]	3834.4±0.4 [37]
TiXIX <sup>b</sup>	$2s 2p^3 \ ^3P_0 - ^3P_1$	6092±10		6092±16 [37]
FeXVIII <sup>a</sup>	$2s^2 2p^5 \ ^2P_{3/2} - ^2P_{1/2}$	974.85±0.02	974.86±0.02 [37, 50]	974.858±0.019 [37]

<sup>a</sup>in vacuum    <sup>b</sup>in air

### 3.3. M1 lines of high-Z elements (Kr, Mo and Xe)

#### 3.3.1. Introduction

Impurity spectroscopy has been usually done in VUV and EUV ranges below 1000Å in fusion plasma research measuring allowed (electric dipole: E1) transitions of highly charged impurity ions. In D-T burning plasmas in the future a grating and CCD detector of the VUV (or EUV) spectrometer are possibly damaged by the high neutron flux. Moreover, the tritium contamination of the spectrometer is also a serious problem in a view point of safety in addition to a negative effect to the detector. On the contrary, the visible spectroscopy with optical fibers can easily separate the spectrometer from the burning fusion device. This gives an extremely large advantage to such the burning plasma impurity spectroscopy.

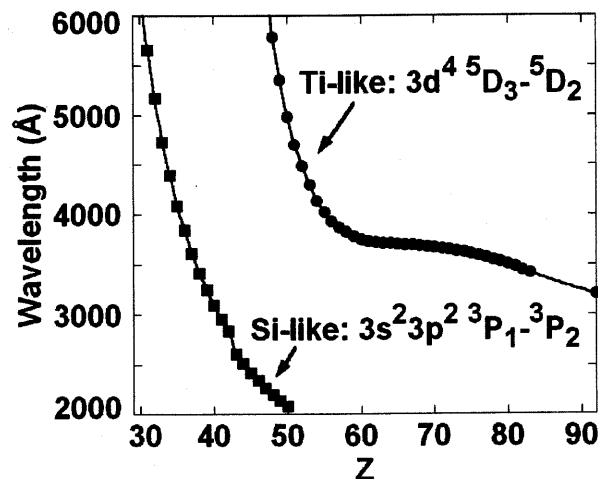


Fig. 3.13 Z dependence of wavelengths for Si-like [68, 103] and Ti-like [69, 86, 87] M1 transitions.

Forbidden (magnetic dipole: M1) transitions emitted among  $ns^2np^k$  ( $k=1-5$ ) ground states have been recently observed in laboratory fusion plasmas [68]. The importance of the M1

transition is that the spectral lines are mainly emitted in the visible range. However, wavelengths of the M1 transitions become again below 2500Å when the nuclear number of the element,  $Z$ , is greater than 40 (see Fig. 3.13). Fifteen years ago, Feldman, Indelicato and Sugar found that the M1 transitions of  $3d^4 \ ^5D_3\text{-}^5D_2$  from Ti-like ions are emitted in the visible range for heavy elements of  $60 \leq Z \leq 92$  [69], as shown in Fig.3.13. Since then, the Ti-like M1 transitions have been studied on theoretical and experimental works. Especially, the experiment has been extensively done in electron beam ion trap (EBIT) devices [70-88]. On the other hand, the heavy elements such as molybdenum and tungsten are one of candidates to plasma facing materials in ITER. If the impurity diagnostics of such heavy impurities is possible in the visible spectroscopy, the essential difficulty related to the impurity diagnostics in the burning plasma will be solved. Visible M1 transitions from argon have been studied and the wavelengths and the physical processes on the M1 emission have been analyzed in details in Large Helical Device (LHD) [89-91]. The M1 transitions from highly charged heavy impurity ions of Kr, Mo, Xe and W have been also surveyed in visible and near-UV ranges above 2500Å. In this paper results of the survey are reported with the line analysis and the measured M1 transitions are listed with precisely determined wavelengths.

### 3.3.2. Experimental setup

The Kr and Xe are externally puffed at the beginning of LHD NBI discharges for the present study. When the rare gas is puffed during discharges, the particle supply becomes inefficient due to the screening effect of the ergodic layer. Typical plasma parameters of the discharges are the electron temperature of  $T_e \sim 1\text{-}2\text{keV}$  and the electron density of  $n_e \sim 2\text{-}5 \times 10^{19} \text{m}^{-3}$ . The magnetic field strength in the present experiment is 3T at the magnetic axis. The Mo and W are injected by a method of impurity pellet injection. The carbon pellet including a thin wire (0.1-0.2mm in diameter and 0.5mm in length) instead of pure metallic pellets is injected into the LHD discharges to avoid the plasma thermal

collapse. [92, 93]. The M1 transition is observed using a 1.33m Czerny-Turner-type spectrometer with a 1800 grooves/mm grating and a back-illuminated charge-coupled device (CCD) detector [94]. Reciprocal linear dispersion of this spectrometer is  $3.85\text{\AA}/\text{mm}$ . The visible emission is collected by a focusing lens and transmitted by optical fibers with a core diameter of  $100\mu\text{m}$ . The fibers are installed and arranged on the window of the diagnostic port. The end of the fibers at the other side is coupled on the entrance slit of the visible spectrometer. The size of the CCD exposure area is  $13.3\times 13.3\text{mm}^2$  ( $13\times 13\mu\text{m}^2/\text{pixel}$ ) and the total number of channels are  $1024\times 1024$ . The CCD is operated at  $-20^\circ\text{C}$  to reduce the thermal noise down to a negligible level.

### 3.3.3. Results and discussion

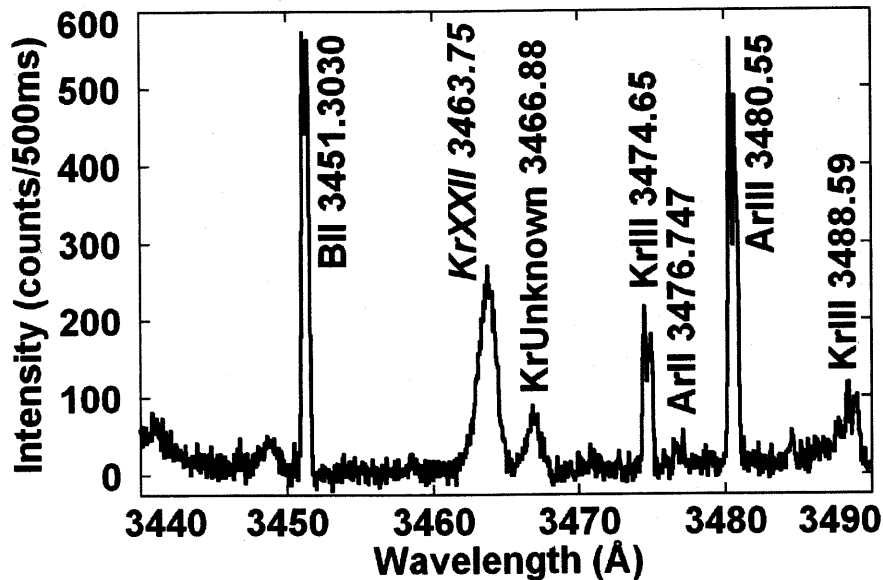


Fig. 3.14 Spectrum with KrXXII M1 transition. Italic fonts indicate the Kr M1 lines.

Figure 3.14 shows spectrum of the M1 transition of KrXXII ( $\text{Kr}^{21+}$ ; P-like)  $3s^23p^3$   $^2D_{3/2}$ - $^2D_{5/2}$   $3463.75\pm 0.05\text{\AA}$ . The KrXXII line has a wider Doppler broadening as compared with other lines in low-ionized charge states, because impurity ions in higher ionization

stages exist in higher temperature region of the plasma. Then, it is easy to notice the existence of the M1 transition in the spectrum, if the intensity of the M1 transition is enough. The wavelength of the M1 transition is carefully determined by interpolation between well known lines of BII 3451.3030Å and ArIII 3480.55Å. Boron is brought into LHD with boronization for wall conditioning. Since Kr gas is puffed in low-density Ar discharges in the present study, Ar lines are visible with high intensities. It is seen that emission lines from low-ionized ions are splitted by the Zeeman effect. There exists an unknown line at 3466Å. This line has approximately identical Doppler broadening to the KrXXII M1 transition. Therefore, the unknown line is also estimated to be the M1 transition.

The measured M1 transition of KrXXII is listed in Table 3.7 with the wavelength determined in the present study. The error value of wavelength is only determined by the Doppler shift of plasmas, which is estimated from the line shift distribution measured using several discharges, since the statistical error in the present experiment is much less than 0.02Å. Experimental results from EBIT are presented for comparison. The wavelength accuracy obtained here is much better than the result from EBIT. The difference in the brightness of the M1 transition between the LHD plasma and EBIT is the main reason why the determined wavelength accuracy is so different, because the error in wavelengths are essentially determined by statistical error as a function of the signal counts when the measured line is analyzed with line fitting. The M1 transitions from LHD plasmas are really much brighter than the EBIT. It is estimated the difference is in order of  $10^3$ - $10^5$ . Theoretically predicted wavelengths are also listed in the Table 1. However, the calculated values are much different from the measured value. At present it is very difficult to calculate theoretically the wavelength in heavy elements because of the complicated atomic system.

KrXXIII ( $\text{Kr}^{22+}$ : Si-like)  $3s^23p^2 \ ^3P_1$ - $^3P_2$  3841.07±0.03Å is observed in the same experimental condition as the KrXXII line, as shown in Fig. 3.15. Here, HI 3835.384Å and ArII 3850.581Å are good reference lines for the wavelength determination. The wavelength of the KrXXIII M1 transition is widely examined in several experimental works from EBIT (see Table 3.7). Only one of them is obtained from tokamak of TEXT [32].

The high-precision wavelength of the KrXXIII line is reported from the EBIT as a value of  $3841.146 \pm 0.002 \text{ \AA}$  with an elaborate fitting procedure [35].

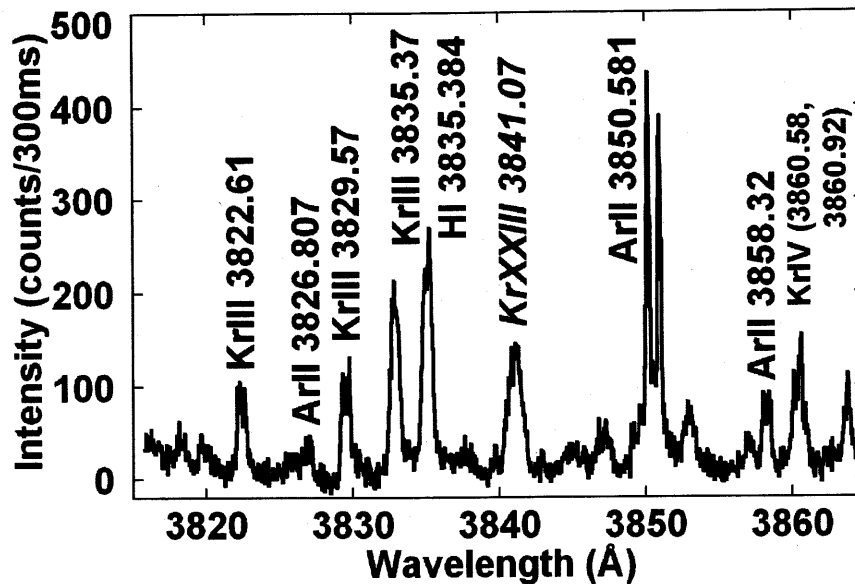


Fig. 3.15 Spectrum with KrXXIII M1 transition. *Italic fonts indicate the Kr M1 line.*

A spectrum of MoXXIX ( $\text{Mo}^{28+}$ : Si-like)  $3s^2 3p^2 \ ^3P_1\text{-}^3P_2$   $2842.10 \pm 0.05 \text{ \AA}$  in the same isoelectronic sequence as the KrXXII line is shown in Fig. 3.16. The vertical scale in the figure is adjusted to the MoII lines for good understanding. The MoXXIX wavelength is determined by the several MoII lines. Carbon lines are recorded in Fig. 4. The carbon is a unique abundant impurity in LHD and mainly originates in the carbon divertor plates. The MoXXIX line is measured in PLT tokamak at the first time [68]. Other experimental works are done in EBIT [75].

A spectrum of XeXXXIII ( $\text{Xe}^{32+}$ : Ti-like)  $3d^4 \ ^5D_3\text{-}^5D_2$   $4139.01 \pm 0.02 \text{ \AA}$  is traced in Fig. 3.17. The Ti-like XeXXXIII measured in LHD is obtained for the first time in laboratory fusion plasmas, whereas the several experimental results are reported from EBIT (see Table 3.7). High ionization energy is required to produce the  $\text{Xe}^{32+}$  ions in plasmas in addition to the stable discharge without MHD instability. The LHD discharge is really favorable to the study of the highly ionized heavy elements. The wavelength of the XeXXXIII determined

here is in good agreement with the calculated result of 4138.3Å. Hartree-Fock approach including relativistic corrections is done with semi-empirical adjustments considering the experimental results [86] (see Table 3.7).

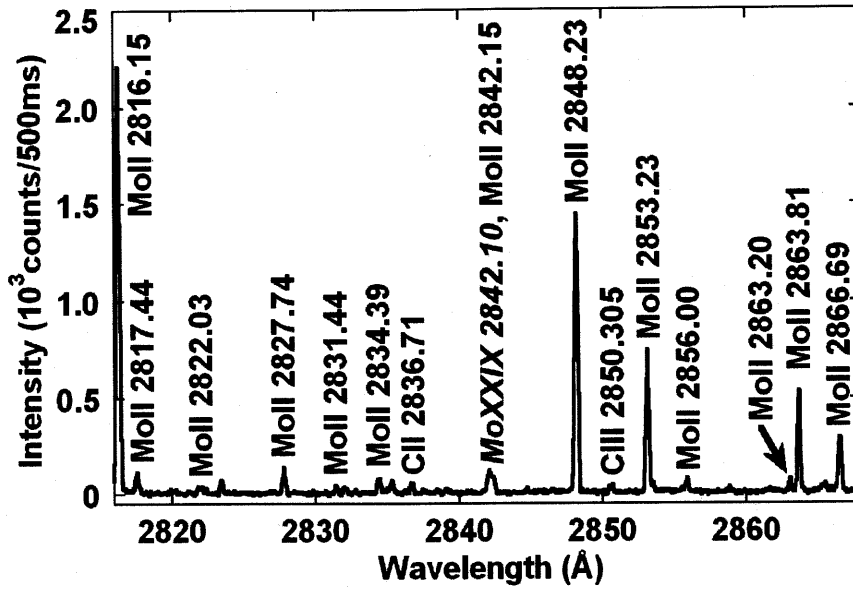


Fig. 3.16 Spectrum with MoXXIX M1 transition. *Italic fonts indicate the Mo M1 line.*

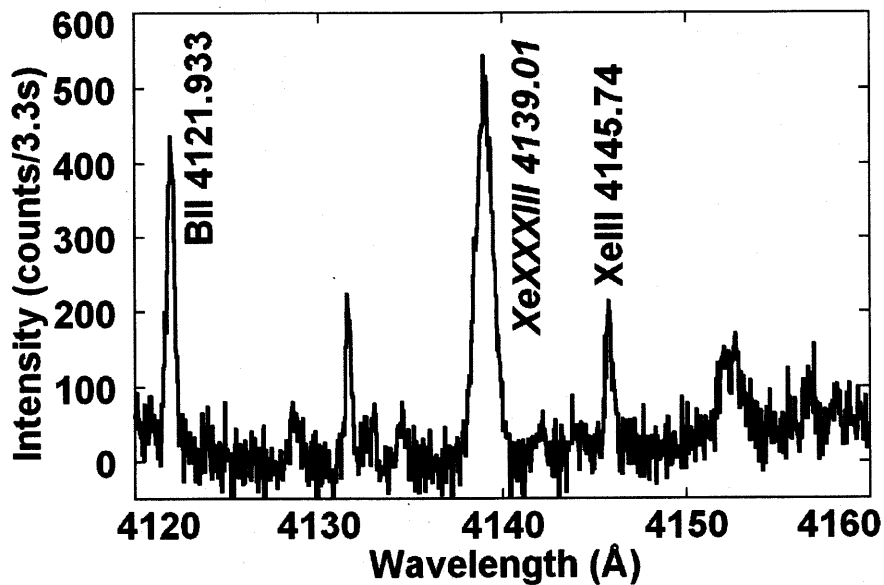


Fig. 3.17 Spectrum with XeXXXIII M1 transition. *Italic fonts indicate the Xe M1 line.*

### 3.3.4. Summary

M1 transitions of KrXXII (Kr<sup>21+</sup>: P-like)  $3s^23p^3 \ ^2D_{3/2}-^2D_{5/2}$  3463.75±0.05Å, KrXXIII (Kr<sup>22+</sup>: Si-like)  $3s^23p^2 \ ^3P_1-^3P_2$  3841.07±0.03Å, MoXXIX (Mo<sup>28+</sup>: Si-like)  $3s^23p^2 \ ^3P_1-^3P_2$  2842.10±0.05Å, XeXXXIII (Xe<sup>32+</sup>: Ti-like)  $3d^4 \ ^5D_3-^5D_2$  4139.01±0.02Å have been observed with high accuracy in Large Helical Device. These observed M1 lines are useful to the visible impurity spectroscopy in D-T burning plasmas.

**Table 3.7** M1 transitions of heavy impurity elements observed in the present study and determined wavelengths. Comparison is made with former experimental works and calculated results.

Spectra	Transition	Observed (Å)		Calculated (Å)
		This work	Others	Others
KrXXII	$3s^2 3p^3$	3463.75±0.05	3464.7±0.6 [95]	3446±30 [68]
(Kr <sup>21+</sup> ) E <sub>i</sub> =990eV	$^2D_{3/2}-^2D_{5/2}$		3464 [75] 3466.6±0.2 [96]	3438±2 [97]
KrXXIII	$3s^2 3p^2 ^3P_1-^3P_2$	3841.07±0.03	3840.9±0.3 [68,98,99]	3663.5 [103]
(Kr <sup>22+</sup> )			3840.8±2 [70] 3842.6 [78]	3832±40 [68]
935eV			3841.4±0.2 [100] 3840.5±0.9 [81]	3845 [101]
			3841.1±0.2[96] 3843±2 [101]	3837.0±6.5 [102]
			3841.146±0.002 [102]	
MoXXIX	$3s^2 3p^2 ^3P_1-^3P_2$	2842.10±0.05	2841.1±0.2 [68,98]	2712.1511 [103]
(Mo <sup>28+</sup> ) 1590eV			2840±2 [75]	2834±40 [68]
XeXXXIII	$3d^4 ^5D_3-^5D_2$	4139.01±0.02	4139.4±2.0 [70]	3952.5 [69]
(Xe <sup>32+</sup> )			4130±0.2 [77]	4130 [71]
1920eV			4138.7 [78]	4079.3 [73]
			4138.8±0.7 [81]	4036.59 [77]
			4139±2 [101]	4052 [78,101]
				4155.3 [81]
				4156.44 [82]
				4125.9 [85]
				4138.3 [86]
WLIII	$3d^4 ^5D_3-^5D_2$	-	3626±2 [80]	3546.1 [69]
(W <sup>52+</sup> )			3626.7±0.5 [81]	3524 [71]
4927eV			3627.13±0.10 [79,87]	3601.5 [76]
				3624.7 [81]
				3625.68 [82]
				3606.8 [85]
				3627.2 [86]

## References

- [1] W.-Ü L. Tchang-Brillet and V. I. Azarov, *Phys. Scr.* **T100**, 104-113 (2002).
- [2] R. C. Isler, *Fusion Eng. Des.* **34-35**, 115-123 (1997).
- [3] W. Biel, *et al.*, *Fusion Sci. Technol.* **47**, 246-252 (2005).
- [4] K. Ebisawa, *et al.*, *Rev. Sci. Instrum.* **70**, 328-331 (1999).
- [5] V. A. Soukhanovskii, *et al.*, *Rev. Sci. Instrum.* **72**, 3270-3276 (2001).
- [6] R. Barnsley, *et al.*, *Rev. Sci. Instrum.* **74**, 1969-1973 (2003).
- [7] H. Kubo, *et al.*, *Nucl. Fusion* **33**, 1427-1433 (1993).
- [8] D. G. Nilson, M. E. Fenstermacher and R. Ellis, *Rev. Sci. Instrum.* **70**, 738-741 (1999).
- [9] J. Miyazawa, *et al.*, *Fusion Eng. Des.* **34-35**, 235-239 (1997).
- [10] T. Sugie, *et al.*, JAERI-M 93-057 (1993).
- [11] Y. Okamoto, *et al.*, *Rev. Sci. Instrum.* **72**, 4366-4371 (2001).
- [12] M. J. May, *et al.*, *Phys. Rev. E* **61**, 3042-3052 (2000).
- [13] S. Morita and M. Goto, *Rev. Sci. Instrum.* **74**, 2036-2039 (2003).
- [14] R. Katai, S. Morita and M. Goto, *Rev. Sci. Instrum.* **77**, 10F307-1-5 (2006).
- [15] H. P. Garnir and P. H. Lefèbvre, *Nucl. Instrum. Meth. Phys. Res. B* **235**, 530-534 (2005)
- [16] M. F. Stamp, *et al.*, CRPP EPFL LRP 220 (1983).
- [17] N. J. Peacock, M. F. Stamp and J. D. Silver, *Phys. Scr.* **T8**, 10-20 (1984).
- [18] H. Kubo, *et al.*, JAERI-M 88-126 (1988) in japanese.
- [19] A. J. J. Raassen, *et al.*, *Astron. Astrophys. Suppl. Ser.* **95**, 223-231 (1992).
- [20] A. G. Trigueiros, *et al.*, *J. Opt. Soc. Am. B* **14**, 2463-2468 (1997).
- [21] I. Lesteven-Vaïsse, *et al.*, *Phys. Scr.* **38**, 45-54 (1988).
- [22] P. S. Antsiferov, *et al.*, *Phys. Scr.* **62**, 127-131 (2000).
- [23] R.L. Kelly, *J. Phys. Chem. Ref. Data.* **16**, Suppl. 1 (1987).
- [24] D. A. Verner, E. M. Verner and G. J. Ferland, *At. Data Nucl. Data Tables* **64**, 1-180 (1996).
- [25] B. Denne and E. Hinnov, *J. Opt. Soc. Am. B* **1**, 699-703 (1984).

- [26] C. Breton, *et al.*, J. Phys. E: Sci. Instrum. **20**, 554-555 (1987).
- [27] J. Z. Klose and W. L. Wiese, J. Quant. Spectrosc. Radiat. Transfer. **42**, 337-353 (1989).
- [28] M. Mimura, *et al.*, Jpn. J. Appl. Phys. **29**, 2831-2834 (1990).
- [29] V. Kaufman and J. Suger, J. Phys. Chem. Ref. Data. **15**, 321-387 (1986).
- [30] R. Katai, S. Morita and M. Goto, J. Plasma Fusion Res. Ser. **7**, 9-13 (2006).
- [31] R. Katai, S. Morita and M. Goto, J. Quant. Spectrosc. Radiat. Transfer. (to be published).
- [32] S. Morita, M. Goto, Y. Takeiri *et al.*, Nucl. Fusion **43**, 899-909 (2003).
- [33] Y. Takeiri, S. Morita *et al.*, Nucl. Fusion **45**, 565-573 (2005).
- [34] R. C. Isler *et al.*, Phys. Plasma **4**, 355-368 (1997).
- [35] J. Laimer, *et al.*, Meas. Sci. Technol. **6**, 1413-1421 (1995).
- [36] M. Goto and S. Morita, Phys. Rev. E **65**, 026401-1-6 (2002).
- [37] V. Kaufman and J. Suger, J. Phys. Chem. Ref. Data. **15**, 321-387 (1986).
- [38] S. Suckewer and E. Hinnov, Phys. Rev. Lett. **41**, 756-759 (1978).
- [39] S. Suckewer, *et al.*, Nucl. Fusion **19**, 1681-1683 (1979).
- [40] K. D. Lawson, N. J. Peacock and M. F. Stamp, J. Phys. B **14**, 1929-1952 (1981).
- [41] M. Finkenthal, R. E. Bell and H. W. Moos, J. Appl. Phys. **56**, 2012-2016 (1984).
- [42] J. R. Roberts, *et al.*, Phys. Rev. A **35**, 2591-2595 (1987).
- [43] E. C. Crume, Jr., L. D. Horton, R. C. Isler and S. Morita, Rev. Sci. Instrum. **61**, 3147 (1990).
- [44] R. Myrnäs, C. Jupen, G. Miecznik and I. Martinson, Phys. Scr. **49**, 429-435 (1994).
- [45] B. Denne and E. Hinnov, Phys. Scr. **35**, 811-818 (1987).
- [46] R. U. Datla, J. R. Roberts and A. K. Bhatia, Phys. Rev. A **43**, 1110-1113 (1991).
- [47] T. R. Ayres, *et al.*, Astrophys. J. **583**, 963-984 (2003).
- [48] S. Redfield, *et al.*, Astrophys. J. **585**, 993-1006 (2003).
- [49] U. Feldman, E. Landi and W. Curdt, Astrophys. J. **607**, 1039-1045 (2004).
- [50] U. Feldman, *et al.*, Astrophys. J. **503**, 467-474 (1998).
- [51] I. Draganić *et al.*, Phys. Rev. Lett. **91**, 183001-1-4 (2003).
- [52] H. Chen, P. Beiersdorfer, C. L. Harris and S. B. Utter, Phys. Scr. **65**, 252-256 (2002).
- [53] D. J. Bieber, H. S. Margolis, P. K. Oxley and J. D. Silver, Phys. Scr. **T73**, 64-66

- (1997).
- [54] H. Watanabe, *et al.*, Phys. Rev. A **63**, 042513-1-6 (2001).
  - [55] E. Träbert, *et al.*, Astrophys. J. **541**, 506-511 (2000).
  - [56] R. Katai, S. Morita and M. Goto, J. Plasma Fusion Res. **7**, 9-13 (2006).
  - [57] H. Nozato, S. Morita, M. Goto, A. Ejiri and Y. Takase, Rev. Sci. Instrum. **74**, 2032-2035 (2003).
  - [58] S. Morita and M. Goto, Rev. Sci. Instrum. **74**, 2036-2039 (2003).
  - [59] R. Katai, S. Morita and M. Goto, Rev. Sci. Instrum. **77**, 10F307-1-5 (2006).
  - [60] M. B. Chowdhuri, S. Morita, M. Goto, H. Nishimura, K. Nagai and S. Fujita, Rev. Sci. Instrum. to be published.
  - [61] M. Goto and S. Morita, Rev. Sci. Instrum. **77**, 10F124-1-4 (2006).
  - [62] M. H. Prior, J. Opt. Soc. Am. B **4**, 144-147 (1987).
  - [63] R.L. Kelly, J. Phys. Chem. Ref. Data. **16**, Suppl. 1 (1987).
  - [64] "NIST Atomic Spectra Database", <http://physics.nist.gov/> (2006).
  - [65] B. Edlén, Phys. Scr. **28**, 51-67 (1983).
  - [66] B. Edlén, Phys. Scr. **26**, 71-83 (1982).
  - [67] B. Edlén, Phys. Scr. **28**, 483-495 (1983).
  - [68] V. Kaufman and J. Sugar, J. Phys. Chem. Ref. Data. **15**, 321-387 (1986).
  - [69] U. Feldman, P. Indelicato and J. Sugar, J. Opt. Soc. Am. B **8**, 3-5 (1991).
  - [70] C. Morgan, *et al.*, Phys. Rev. Lett. **74**, 1716-1719 (1995).
  - [71] F. G. Serpa, *et al.*, Phys. Rev. A **53**, 2220-2224 (1996).
  - [72] F. G. Serpa, *et al.*, Phys. Rev. A **55**, 4196-4200 (1997).
  - [73] D. R. Beck, Phys. Rev. A **56**, 2428-2430 (1997).
  - [74] D. J. Bieber, H. S. Margolis, P. K. Oxley and J. D. Silver, Phys. Scr. **T73**, 64-66 (1997).
  - [75] E. Träbert, P. Beiersdorfer, S. Utter and J. R. Crespo López-Urrutia, Phys. Scr. **58**, 599-604 (1998).
  - [76] D. R. Beck, Phys. Rev. A **60**, 3304-3305 (1999).
  - [77] D. Kato, *et al.*, Phys. Scr. **T80**, 446-447 (1999).

- [78] J. R. Crespo López-Urrutia, P. Beiersdorfer, K. Widmann and V. Decaux, Phys. Scr. **T80**, 448-449 (1999).
- [79] S. B. Utter, P. Beiersdorfer and G. V. Brown, Phys. Rev. A **61**, 030503-1-4 (2000).
- [80] J. V. Porto, I. Kink and J. D. Gillaspay, Phys. Rev. A **61**, 054501-1-4 (2000).
- [81] H. Watanabe, *et al.*, Phys. Rev. A **63**, 042513-1-6 (2001).
- [82] D. Kato *et al.*, J. Chinese Chem. Soc. **48**, 525-529 (2001).
- [83] D. N. Crosby, K. Gaarde-Widdowson, J. D. Silver and M. R. Tarbutt, Phys. Scr. **T92**, 144-146 (2001).
- [84] U. Feldman, R. Doron, M. Klapisch and A. Bar-Shalom, Phys. Scr. **63**, 284-288 (2001).
- [85] C. F. Fischer and S. Fritzsche, J. Phys. B **34**, L767-L772 (2001).
- [86] E. Biemont, E Träbert and C. J. Zeippen, J. Phys. B **34**, 1941-1951 (2001).
- [87] S. B. Utter, P. Beiersdorfer and E Träbert, Phys. Rev. A **67**, 012508-1-5 (2003).
- [88] H. A. Sakaue and D. Kato, J. Vac. Soc. Jpn. **48**, 23-28 (2005) in Japanese.
- [89] R. Katai, S. Morita, M. Goto, J. Plasma Fusion Res. Ser. **7**, 9-13 (2006).
- [90] R. Katai, S. Morita, M. Goto, J. Quant. Spectrosc. Radiat. Transfer (to be published).
- [91] A. Iwamae, M. Atake, A Sakaue, M. Goto, R. Katai and S. Morita, Phys. Plasmas (to be published).
- [92] H. Nozato, S. Morita, M. Goto, A. Ejiri and Y. Takase, Rev. Sci. Instrum. **74**, 2032-2035 (2003).
- [93] R. Katai, S. Morita, M. Goto *et al.*, submitted to Jpn. J. Appl. Phys.
- [94] M. Goto and S. Morita, Rev. Sci. Instrum. **77**, 10F124-1-4 (2006).
- [95] F. G. Serpa, *et al.*, Phys. Rev. A **55**, 1832-1835 (1997).
- [96] H. Chen, P. Beiersdorfer, C. L. Harris and S.B. Utter, Phys. Scr. **66**, 133-139 (2002).
- [97] J. Sugar, V. Kaufman and W. L. Rowan, J. Opt. Soc. Am. B **8**, 22-26 (1991).
- [98] J. Sugar, V. Kaufman and W. L. Rowan, J. Opt. Soc. Am. B **7**, 152-158 (1990).
- [99] J.R. Roberts, *et al.*, Phys. Rev. A **35**, 2591-2595 (1987).
- [100] E. Träbert, S. B. Utter and P. Beiersdorfer, Phys. Lett. A **272**, 86-92 (2000).
- [101] J. R. Crespo López-Urrutia, P. Beiersdorfer, K. Widmann and V. Decaux, Can. J.

Phys. **80**, 1687-1700 (2002).

[102] I. I. Tupitsyn, *et al.*, Phys. Rev. A **68**, 022511-1-5 (2003).

[103] K.-N. Huang, At. Data Nucl. Data. Tables **32**, 503-566 (1985).

## Chapter 4

### Intensity analysis on M1 transitions

#### 4.1. Introduction

It is known that the line intensity ratio of the M1 transition to the allowed (E1) transition becomes sensitive to the electron density, because the dependence on the electron density of the population mechanism for the upper states of the M1 and E1 transitions is different [1-3]. Since the transition probability of the M1 lines is very small compared with the E1 line, the collisional de-excitation by electrons and protons is not negligible in a relatively high-density region. Several theoretical calculations on the M1/E1 line intensity ratio have been carried out until now [4-11]. However, there exists no detailed experimental study on the intensity ratio.

In this section, the intensity ratios of the M1 to E1 transitions are experimentally studied and results are presented on ArX (5533Å/165Å) and ArXV (5944 Å/221Å) with a simple level population calculation. Contribution of fast proton impact, which is brought by 180keV Neutral Beam Injection (NBI), to the ratios of F-like ions such as ArX, TiXIV (2118Å/122Å) and FeXVIII (975 Å /94Å) is also studied and analyzed with the calculation.

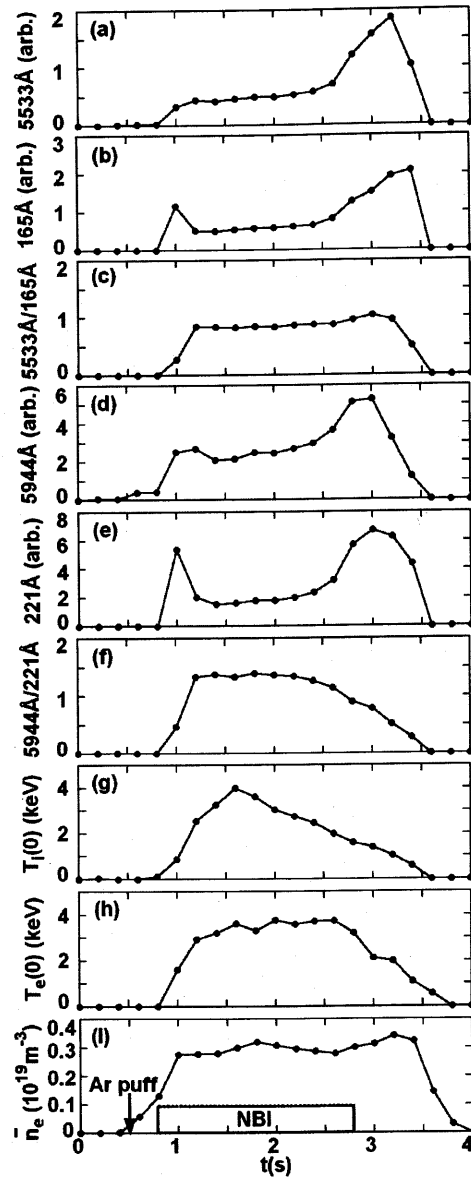


**Fig. 4.1** Temporal behaviors of intensities of (a) ArX 5533Å, (b) ArX 165Å, (c) ArXV 5944Å and (d) ArXV 221Å, line ratios of (e) 5533Å/165Å and (f) 5944Å/221Å, (g)  $T_1(0)$ , (h)  $T_e(0)$ , and (i) line-averaged electron density  $\bar{n}_e$ . Argon is puffed at  $t=0.5$ s during ECH phase and NBI is operated during  $t=0.8$ - $2.8$ s for further heating.

## 4.2. Analysis of line intensity ratios

Figure 4.1 shows temporal behaviors of Ar line intensities (ArX 5533Å and 165Å, ArXV 5944Å and 221Å), line intensity ratios of 5533Å/165Å and 5944Å/221Å, central ion temperature  $T_i(0)$ , central electron temperature  $T_e(0)$  and line-averaged electron density  $\bar{n}_e$  in the argon discharge. The line-averaged electron density, which is measured by FIR (far-infra red) interferometer, is built up by external Ar gas puff at  $t=0.4$ s in ECH (electron cyclotron heating) phase and is kept constant to be  $0.3 \times 10^{19} \text{ m}^{-3}$  (see Fig.6(i)). Intensities of argon lines rapidly increase after NBI (neutral beam injection) is turned on for further heating at  $t=0.8$ s. The electron temperature is measured by Thomson scattering and the central ion temperature is determined by the Doppler broadening of an ArXVII x-ray line using a crystal spectrometer [12]. Both the electron and ion temperatures gradually increase and at  $t=1.6$ s they reach the maximum values of  $T_e(0)=3.5\text{keV}$  and  $T_i(0)=4\text{keV}$ . The transient-phase of the discharge is triggered by turning off the NBI at  $t=2.8$ s. In LHD a long plasma decay phase ( $t=2.8-4.0$ s) always appears, especially in such a low-density discharge, because the magnetic surface for confinement is steadily completed by external helical coils. No spectroscopic data during such a transient phase are used in the present study to avoid a complexity in the analysis. The line ratios between  $t=0.8$ s and  $2.8$ s during NBI phase are used in the following analysis.

The excitation cross sections of ArXV  $2s2p^3P_1-^3P_2$  are shown in Fig. 4.2 as an example. The electron impact data are calculated using a Flexible Atomic Code (FAC) based on the relativistic configuration interaction with independent particle basis wave functions and continuum processes of the distorted-wave approximation [13]. The result calculated from the FAC indicated with solid line showed a good agreement with that from the relativistic distorted-wave method [14] indicated with closed circles. The proton impact data are calculated with a close-coupling impact parameter method [15] and a semi-classical collision theory [16] and both the results show a good agreement. Though the proton impact data are available only for  $E>150\text{eV}$ , the values in the lower energy range should be much smaller than the electron impact data and can be neglected. The electron impact

cross section has the maximum value at the threshold energy of 2.2eV, while for the proton impact at  $E_p=800$  eV.

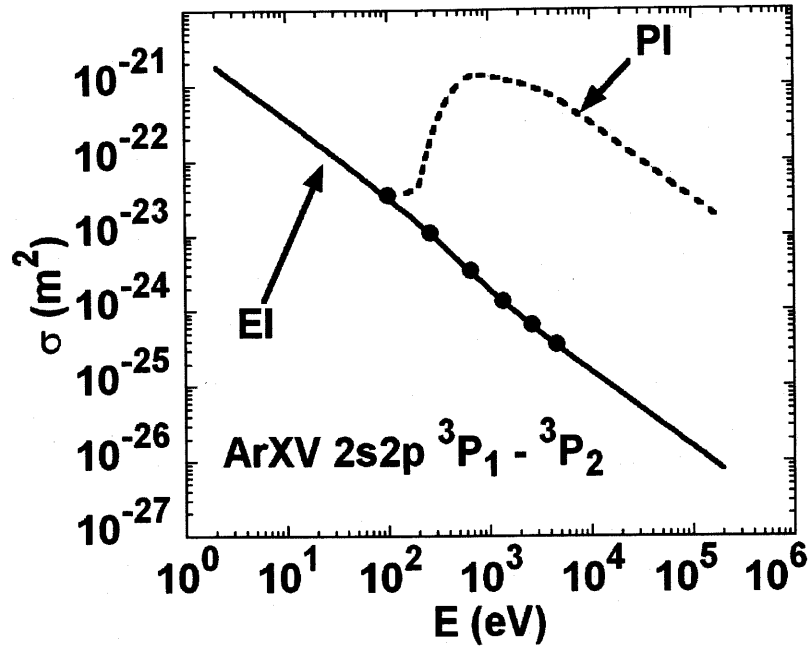


Fig. 4.2 Calculated electron and proton impact excitation cross sections,  $\sigma$ , among fine structure levels of ArXV  $2s2p\ ^3P_1-^3P_2$  as a function of electron and proton impact energy. Solid and dashed lines are expressed electron impact (EI) and proton impact (PI), respectively. Electron impact cross sections are calculated by Flexible Atomic Code [13] (solid line) and relativistic distorted-wave method [14] (closed circles) and proton impact cross section is calculated by close-coupling impact parameter method [15] (dashed line).

In magnetically confined toroidal plasmas, the radial density profile of a certain ionized stage impurity ion is mainly determined by the electron temperature profile. In order to determine the  $T_e$  where ions in a selected ionization stage exist, a radial line intensity distribution of the ions has been measured in the visible range with multi-viewing-chord observation using a Czerny-Turner type spectrometer and fiber arrays. Typical examples on the measured profiles are shown in Fig. 4.3 for M1 lines of ArX and ArXV. Since the

central electron temperature is high ( $\sim 2.5\text{keV}$ ), both the ArX and ArXV line emissions are located in the edge region of the plasma. In the discharges used for the present analysis, slightly different locations are derived at  $\rho \sim 0.8$  between the two ions. The  $T_e$  values for the calculation are determined to be 376eV and 646eV for ArX and ArXV, respectively. The  $T_i$  values for ArX and ArXV are estimated from those of ArXII (991 eV) and ArXVI (1831 eV) shown in Fig. 4.3 assuming an appropriate  $T_i$  profile. Consequently, the  $T_i$  values of 557eV and 1050eV are derived for ArX and ArXV, respectively. The proton temperature is assumed to be equal to the Ar ion temperature ( $T_i = T_p$ ) in the following analysis.

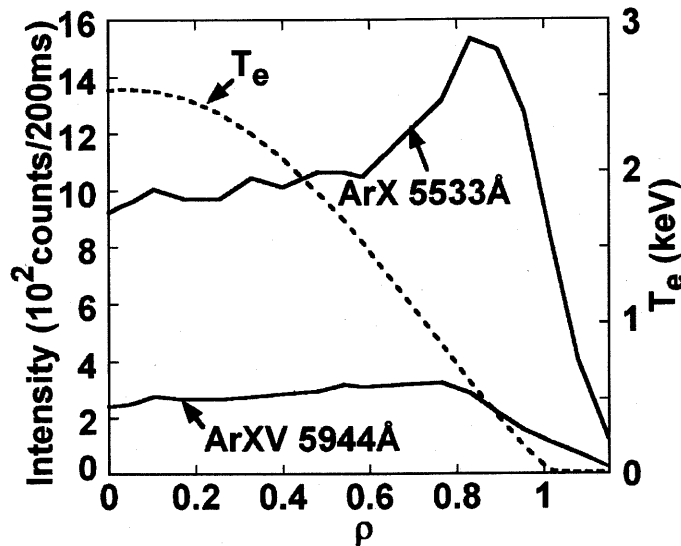


Fig. 4.3 Vertical distributions of line-integrated ArX (5533Å) and ArXV (5944Å) with solid lines and  $T_e$  profile with dashed line measured from argon plasmas.

#### 4.3. Line ratio of F-like ions (ArX, TiXIV and FeXVIII)

In order to analyze the density dependence of the M1 line intensity, the F-like ions are selected as the simplest configuration and the level-population of ArX has been calculated with quasi-steady-state rate equations, which include high-energy proton impact excitation

between the fine structure levels. This level-population calculation of ArX is applied to a three levels model, because the influence of electron cascade from higher levels is considered to be relatively small. The energy level diagram of ArX considered here is

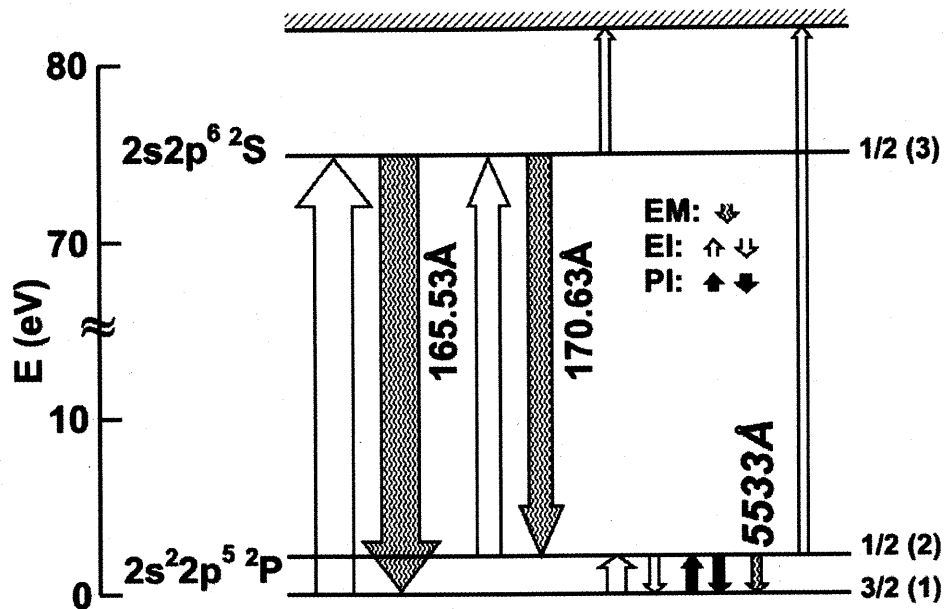


Fig. 4.4 Partial energy diagram of ArX with M1 ( $5533\text{\AA}$ ) and E1 ( $165.53\text{\AA}$  and  $170.63\text{\AA}$ ) transitions (EM: spontaneous emission, EI: electron impact collisional excitation and de-excitation, PI: proton impact collisional excitation and de-excitation). Horizontal line with hatch above figure indicates ionization level. Integers in brackets at right hand denote states used in quasi-steady-state rate equations with J values of levels. Width of arrows represents relative amplitudes of transitions.

illustrated in Fig. 4.4. The numbers in the parentheses are the labels used to identify the levels in the following discussion. The atomic processes considered in the model are drawn with arrows and their width represents the magnitude of the population flow under a typical plasma condition. The population mechanism of the level 1 is rather simple and is explained with the corona equilibrium, namely, the population is determined on a balance of the population inflow from the lower levels due to electron collisions and the outflow down to the lower levels due to spontaneous radiative transitions. Consequently, the level 3

population proportionally increases with the electron density. On the other hand, the population mechanism of level 2 is rather complicated because several processes are competitive for the population determination owing to the small transition probability of the level 2 to level 1 ( $1.06 \times 10^2 \text{s}^{-1}$ ). The population inflow to the level 2 is always dominated by the collisional excitation from the level 1 and the radiative cascade from the level 3, and their transition rates are proportional to the electron density: for the latter process the level 3 density is proportional to the electron density though the transition probability is constant. As for the population outflow from the level 2, in the low density case it is dominated by the radiative transition to the level 1 and in the high density case the collisional processes predominate over the radiative process. As a result, in the low density case the level 2 population increases with the electron density similarly to the level 3 population, whereas in the high density case the level 2 population is saturated. The density dependence of the line intensity ratio of E1/M1 is thus understood qualitatively.

Five processes are taken into account to analyze the level 2 population, i.e., electron and proton collisional excitation and de-excitation and radiative decay by M1 transition between the level 2 and level 1, electron impact ionization from the level 2 and radiative decay from the level 3, as shown in Fig. 4.4. A set of quasi-steady-state rate equations in ArX (F-like) configuration is given by

$$n_1 = n_{g1}, \quad (1a)$$

$$n_2[n_e(C_{21}^e + C_{23}^e + S_2) + n_p C_{21}^p + n_{fp} C_{21}^{fp} + A_{21}] = n_1(n_e C_{12}^e + n_p C_{12}^p + n_{fp} C_{12}^{fp}) + n_3(A_{32} + n_e C_{32}^e), \quad (1b)$$

$$n_3[n_e(C_{31}^e + C_{32}^e + S_3) + A_{31} + A_{32}] = n_1 n_e C_{13}^e + n_2 n_e C_{23}^e, \quad (1c)$$

where the subscripts of 1, 2, and 3 are the same meaning as Fig. 4.4. And  $n_e$  and  $n_p$  is the electron and proton densities, respectively,  $n_i$  the population density of energy level  $i$ ,  $A_{ij}$  the spontaneous emission probability,  $C_{ij}^x$  the collisional-excitation rate coefficient when  $i < j$  or de-excitation rate coefficient when  $i > j$  and  $S_i$  the electron impact ionization rate coefficient of level  $i$ . Here, the  $n_{g1}$  is normalized to 1. The de-excitation rate is obtained from the Klein-Rosseland formula as

$$C_{ji}^x = \frac{g_i}{g_j} C_{ij}^x \exp \frac{\Delta E_{ij}}{T_x}, \quad (2)$$

where  $g_{i(j)}$  is the statistical weight of the lower  $i$  or upper  $j$  level,  $\Delta E_{ij}$  and  $T_x$  are the transition energy and the temperature of electron or proton, respectively. In the Ar discharges of LHD the amount of hydrogen is largely reduced since Ar glow discharge cleaning is repeated before the main discharge. The hydrogen density is determined spectroscopically with the help of the impurity and 3-dimensional H $\alpha$  diagnostics and  $Z_{\text{eff}}$  measurement. Here, the value of  $n_p = n_e/5$  is used. The subscript of fp expresses a contribution of collisional process by fast protons, which are originally brought by high-energy neutral beam injection (NBI). The beam energy of the NBI used in LHD is 180keV. These fast protons reduce their energies mainly through the collision with thermal electrons in the plasma and the energies finally become equal to the thermal ion temperature after the collision with thermal ions. A mono-energetic beam of  $E_{\text{fp}}=100\text{keV}$  is then assumed in the calculation. A little change of this energy has no influence on the calculation result (see Fig. 4.2). The excitation rate coefficient by the fast proton impact is given by  $C_{ij}^{\text{fp}} = v_{\text{fp}} \sigma_{ij}^{\text{fp}}$ , where  $v_{\text{fp}}$  is the velocity of fast proton and  $\sigma_{ij}^{\text{fp}}$  is the excitation cross section for the proton impact. The spontaneous transition probabilities of the M1 and E1 lines are given in the atomic database table [17, 18]. The intensity of transition from  $j$  to  $i$  is represented by  $I_{ji} = N_j A_{ji}$ . The F-like ions of TiXIV and FeXVIII are also calculated using the same manner as ArX. Atomic data of ArX, TiXIV and FeXVIII used in this calculation are listed in Table 4.1.

The calculation results on M1/E1 ( $I_{21}/I_{31}$ ) intensity ratios of ArX 5533Å/165Å, TiXIV 2218Å/122Å and FeXVIII 975Å/94Å are shown in Fig. 4.5 as a function of the electron density. In this calculation no contribution of the fast-proton is taken into account ( $n_{\text{fp}} = 0$ ). The intensity of the E1 line essentially has a linear dependence on the electron density in all density range. However, the intensity of the M1 line tends to saturate at higher density range since the radiative decay is limited because of the small value of spontaneous decay rate. Then, strong electron density dependence is appeared in the line ratios of M1/E1. The density dependence of the ratios for ArX, TiXIV and FeXVIII appears above  $1 \times 10^{16} \text{m}^{-3}$ ,

$1 \times 10^{18} \text{m}^{-3}$  and  $1 \times 10^{19} \text{m}^{-3}$ , respectively. This threshold density is mainly determined by the transition probability of the M1 line.

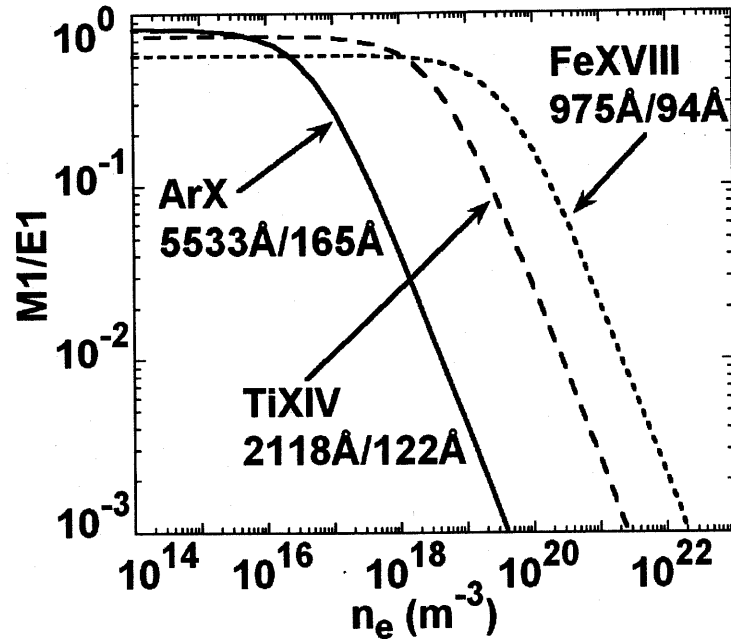


Fig. 4.5 Electron density dependence of line ratios on F-like ions of ArX (solid line), TiXIV (long dashed line) and FeXVIII (short dashed line).

The population of the level 2, the upper level of the M1 line, is generally influenced by the ion collisions because of its small excitation energy from the ground state, whereas for the population of the level 3, which is the upper level of the E1 line, the effect is small. The intensity ratio of these lines has little dependence on the electron temperature, since the temperature range considered here is quite high as compared to the excitation energies of these levels from the ground state. Consequently, their rate coefficients have the similar dependence on the electron temperature. The influence of the ion temperature on the intensity ratios given in Fig. 4.5 is calculated and the results are shown in Fig. 4.6. A relatively low density of  $n_e = 0.3 \times 10^{19} \text{m}^{-3}$  is taken in this calculation ( $n_p = 0$ ) for the later discussion. The ratios show slight dependences in the low temperature region, and are

almost constant in the region higher than 1keV. Therefore, it can be understood the change of the intensity ratio of M1/E1 is ascribed to the electron density.

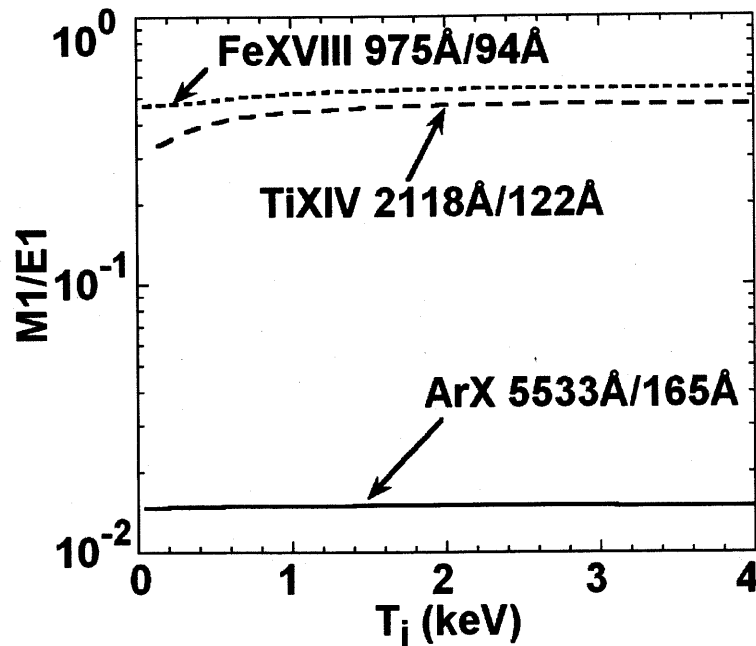


Fig. 4.6 Ion temperature dependence of line ratios on F-like ions of ArX (solid line), TiXIV (long dashed line) and FeXVIII (short dashed line).

In LHD the M1 line is difficult to be observed in the discharges without external impurity injection, because the M1 lines are very weak. In order to measure the density dependence of the ratio (M1/E1) for the medium-Z impurities such as TiXIV and FeXVIII high densities near  $10^{20}\text{m}^{-3}$  are needed with a considerably large amount of such impurities. It is quite difficult to have a smooth discharge of the LHD in such an experimental condition. In contrast to this, the ArX line has the density dependence at much lower densities of  $10^{18}\text{-}10^{19}\text{m}^{-3}$ . The argon discharges of LHD, which can be easily operated in  $n_e=0.2\text{-}1\times 10^{19}\text{m}^{-3}$ , provide a very nice opportunity for the present study.

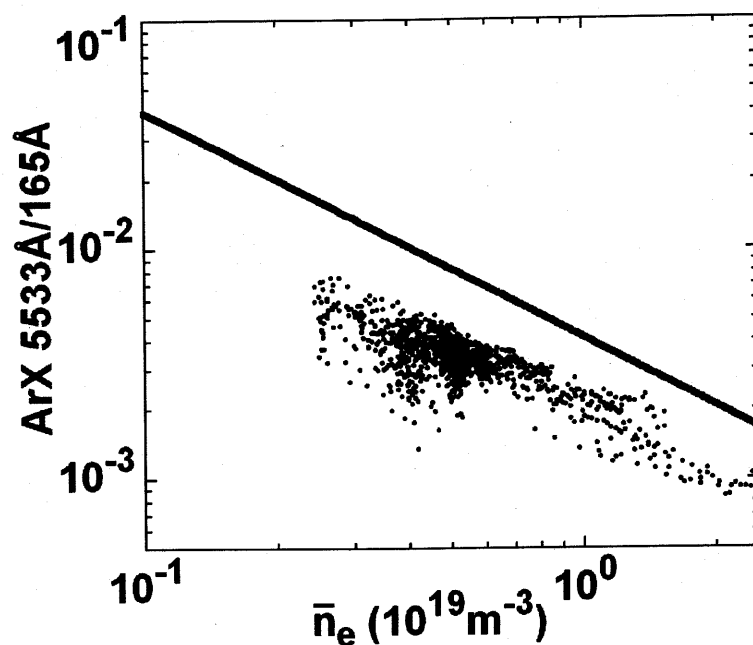
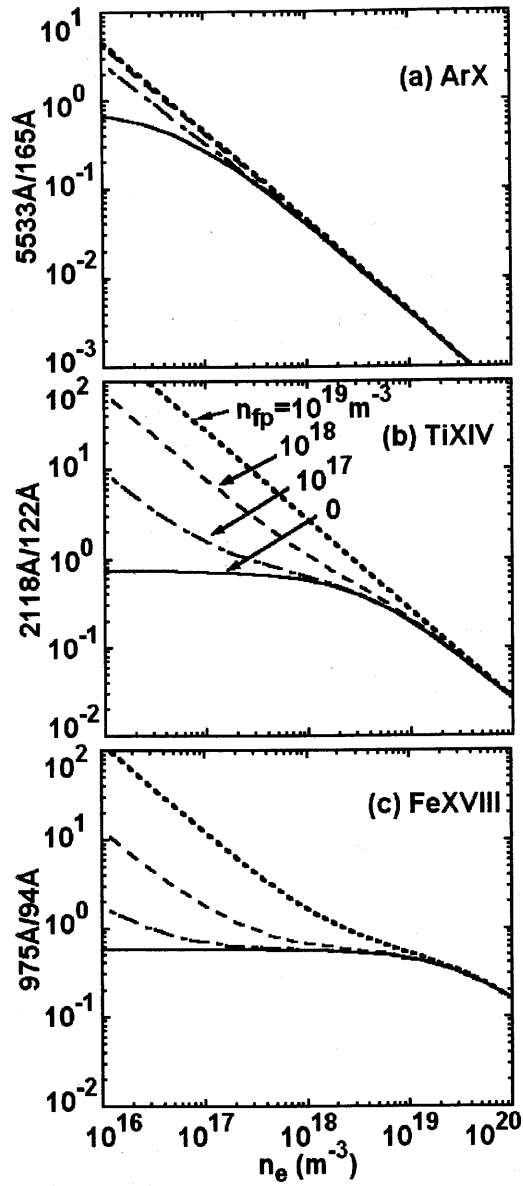


Fig. 4.7 Line ratios of ArX M1/E1 as a function of line-averaged electron density (dotted circles: experimental data, solid line: calculated result).

The M1 visible and E1 EUV lines were measured by scanning the Ar puff rate and controlling the electron density. The result is plotted in Fig. 4.7 with the calculated result. The density in the figure is expressed by a line-averaged electron density,  $\bar{n}_e$ , instead of the local density,  $n_e(\text{ArX})$ , where the ArX is abundant, since it is difficult to obtain the density profile with a good quality from the Thomson scattering measurement owing to the low density discharges. The density profile is obtained at higher density discharges and it is known that the density profile is near flat. Then, the line-averaged electron density used in the figure is roughly equal to the density used in the calculation. However, the data are a little scattered at densities to 10% below  $0.5 \times 10^{19} \text{m}^{-3}$ . This originated in a little difference between the  $\bar{n}_e$  and  $n_e(\text{ArX})$ . The EUV spectrometer is absolutely calibrated using a combination of continuum radiation measurement in the EUV range and a use of the branching ratio (CIV 2s-3p 312Å and 3s-3p 5801Å and 5812Å transitions) [19, 20]. The tendency of the experimentally obtained line ratios against the density is in a good

agreement with the calculation, although a clear discrepancy between experimental and calculated values exists. This difference of 30% is discussed with the result for the ArXV line intensity ratio described in the following section.



**Fig. 4.8** Line ratios (M1/E1) of F-like ions for (a) ArX, (b) TiXIV and FeXVIII with fast proton impact excitation. Assumed fast proton densities are indicated in figure.

Contribution of the collisional excitation by the fast proton originating in the NBI for plasma heating is examined. The result is shown in Fig. 4.8 for several cases of the fast proton density values from  $10^{17}$  to  $10^{19}\text{m}^{-3}$ . The number of fast-protons provided by NBI is  $4.17 \times 10^{20}\text{s}^{-1}$  at input power of 12MW with the injection energy of 180keV. The density of the fast-proton is estimated to be  $1.4 \times 10^{19}\text{m}^{-3}$  where the energy slowing down time of 1s and the LHD plasma volume of  $30\text{m}^3$  are taken into account. The ratio is largely affected by the fast proton impact at lower density range and the enhancement of the M1 line intensity depends on the proton impact cross section. The contribution of the fast proton impact to the M1 line intensity is reduced in the higher density range, because the electron collision processes become dominant. The observation is attempted for TiXIV and FeXVIII M1 lines, since the ArX has no chance to observe the influence of the fast proton impact. In order to observe the line emissions of TiXIV and FeXVIII, impurity pellets were injected. In Fig. 4.9 the results are shown with the calculation data. The experimental results of TiXIV and FeXVIII are absolutely calibrated data of EUV and VUV region. The 3m normal incidence spectrometer with which the M1 VUV lines were observed, the absolute sensitivity has been calibrated by using the branching ratios (Ly $\gamma$  972Å – H $\beta$  4861Å and Ly $\beta$  1025Å – H $\alpha$  6563Å) and direct comparisons of CV 2271Å, CIII 2296Å and BIII 2821Å which are accessible from both of VUV and visible spectrometers [20]. The tendency of the TiXIV ratio is in a good agreement with the calculation, but the FeXVIII ratio has 50% error. This discrepancy of the FeXVIII ratio is discussed in the following section. Unfortunately, the lowest operational density in LHD is  $0.3 \times 10^{19}\text{m}^{-3}$  with the impurity pellet injection and the intensity ratios were obtained only in the density range higher than  $0.4 \times 10^{19}\text{m}^{-3}$ . Therefore the contribution of the fast proton impact was unclear at present.

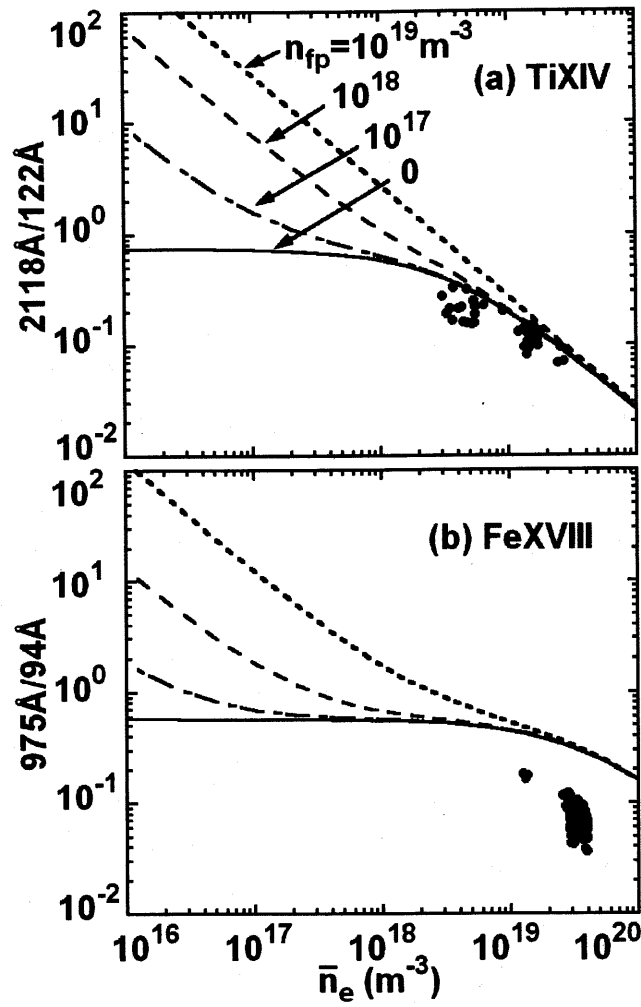


**Fig. 4.9** Experimental results of line ratios for (a) TiXIV and (b) FeXVIII plotted with solid circles.

Calculated results are a parameter of fast proton density assumed in the calculation.

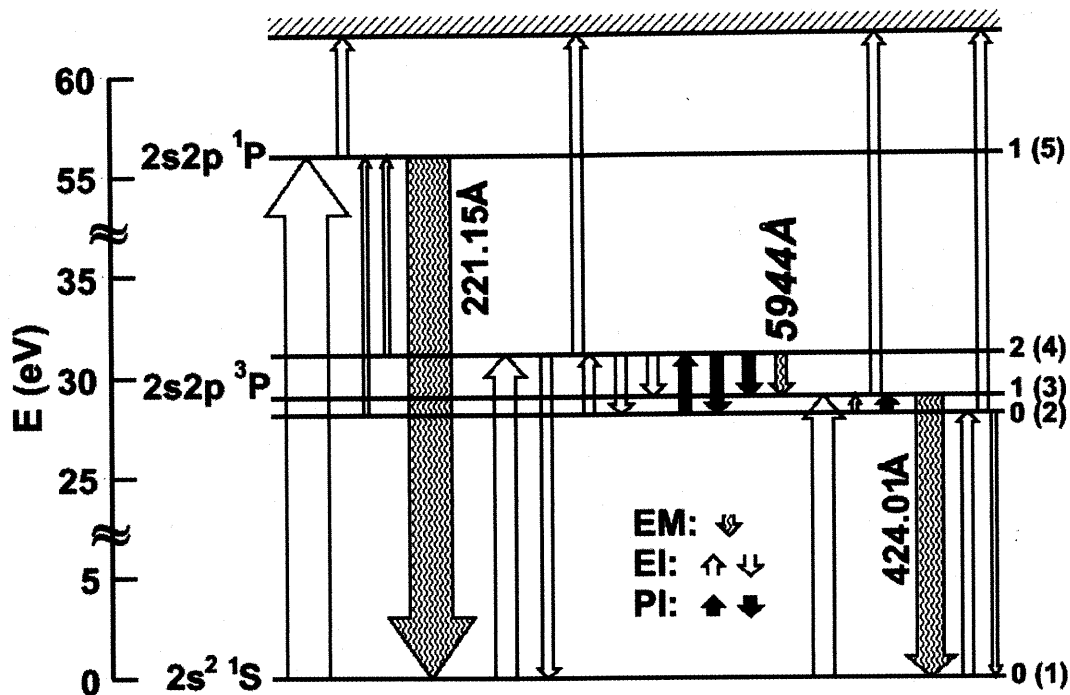


Fig. 4.10 Partial energy diagram of ArXV with M1 5944Å and E1 221.15Å and inter-combination (spin-forbidden) 424.01Å transitions (EM: spontaneous emission, EI: electron impact collisional excitation and de-excitation, PI: proton impact collisional excitation and de-excitation). Horizontal line with hatch above figure indicates ionization level. Integers in brackets at right hand denote states used in quasi-steady-state rate equations with J values of levels. Width of arrows represents relative amplitudes of transitions.

#### 4.4. Line ratio of Be-like ion (ArXV)

The level-population calculation is also carried out for ArXV to obtain the intensity ratio of M1/E1 lines, for which the lowest five levels are taken into account. The energy level diagram is illustrated in Fig. 4.10, where the radiative and collisional transitions considered here are also shown with the arrows. The width of the arrows represents the magnitude of the transition rate under a typical plasma condition. The population mechanism of the level

1 and 5 is explained with the corona equilibrium, which is the same as the level 1 and 3 for ArX case. The level 5 population then proportionally increases with the electron density. The fine-structure levels of 2, 3 and 4 can be populated also by proton impact collision. The levels of 2 and 4 are the meta-stable states which have no radiative decay. The population inflow to the level 4, which is the upper state of M1 transition, is determined by only the collisional excitation from lower levels having no radiative cascade from upper levels, and this is a different point to the level 2 of ArX model. Intensities of three emission lines ( $2s2p\ ^1P_1-2s^2\ ^1S_0$  221Å,  $2s2p\ ^3P_2-^3P_1$  5944Å and  $2s2p\ ^3P_1-2s^2\ ^1S_0$  424Å) are calculated. The following quasi-steady-state rate equations are used for the calculation for ArXV;

$$n_1 = n_{g1}, \quad (3a)$$

$$n_2[n_e(C_{21}^e + C_{23}^e + C_{24}^e + C_{25}^e + S_2) + n_p(C_{23}^p + C_{24}^p) + n_{fp}(C_{23}^{fp} + C_{24}^{fp})] = n_1 n_e C_{12}^e + n_3(n_e C_{32}^e + n_p C_{32}^p + n_{fp} C_{32}^{fp} + A_{32}) + n_4(n_e C_{42}^e + n_p C_{42}^p + n_{fp} C_{42}^{fp}) + n_5(n_e C_{52}^e + A_{52}), \quad (3b)$$

$$n_3[n_e(C_{31}^e + C_{32}^e + C_{34}^e + C_{35}^e + S_3) + n_p(C_{32}^p + C_{34}^p) + n_{fp}(C_{32}^{fp} + C_{34}^{fp}) + A_{31} + A_{32}] = n_1 n_e C_{13}^e + n_2(n_e C_{23}^e + n_p C_{23}^p + n_{fp} C_{23}^{fp}) + n_4(n_e C_{43}^e + n_p C_{43}^p + n_{fp} C_{43}^{fp} + A_{43}) + n_5(n_e C_{53}^e + A_{53}), \quad (3c)$$

$$n_4[n_e(C_{41}^e + C_{42}^e + C_{43}^e + C_{45}^e + S_4) + n_p(C_{42}^p + C_{43}^p) + n_{fp}(C_{42}^{fp} + C_{43}^{fp}) + A_{43}] = n_1 n_e C_{14}^e + n_2(n_e C_{24}^e + n_p C_{24}^p + n_{fp} C_{24}^{fp}) + n_3(n_e C_{34}^e + n_p C_{34}^p + n_{fp} C_{34}^{fp}) + n_5(n_e C_{54}^e + A_{54}) \quad (3d)$$

and

$$n_5[n_e(C_{51}^e + C_{52}^e + C_{53}^e + C_{54}^e + S_5) + A_{51} + A_{52} + A_{53} + A_{54}] = n_1 n_e C_{15}^e + n_2 n_e C_{25}^e + n_3 n_e C_{35}^e + n_4 n_e C_{45}^e, \quad (3e)$$

where the subscripts of 1, 2, 3, 4, and 5 stand for the levels of  $2s^2\ ^1S_0$ ,  $2s2p\ ^3P_0$ ,  $2s2p\ ^3P_1$ ,  $2s2p\ ^3P_2$ , and  $2s2p\ ^1P_1$ , respectively. Other notations have the same meanings as in the ArX case. The atomic data of ArXV used in this calculation are given in Table 4.2. The contribution of fast-proton is also ignored here ( $n_{fp} = 0$ ).

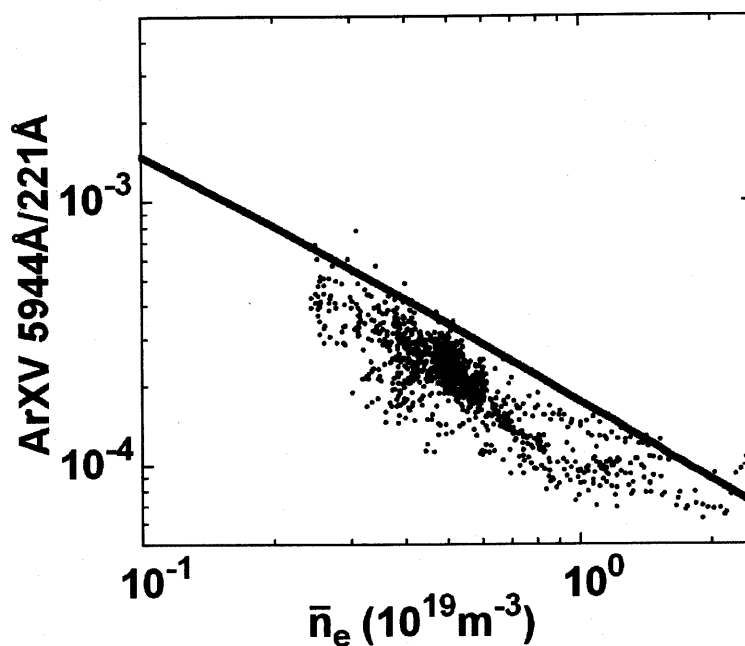


Fig. 4.11 Line ratios of ArXV M1/E1 as a function of line-averaged electron density (dotted circles: experimental data, solid line: calculated result).

Dependence on the line-averaged electron density of the ArXV line intensity ratio can be traced with the experimental data in Fig. 4.11. The calculation result shows a good agreement with the experimental values though the atomic structure of ArXV is more complicated than that of ArX. This means that the rate coefficients used in the calculation are considerably accurate, especially for the electron impact excitation and transition probability of the M1 line, although the proton impact has less contribution to the intensity ratio. This result also indicates that a cascade effect in the population mechanism, which is not included in the calculation, is not so important process and the simple model used in the present work can well explain the experimental data. On the other hand, a clear discrepancy appeared in the ArX and FeXVIII cases. The ArXIII 164.82Å line exists near the ArX 165.53Å line which is used for the ArX ratio. Furthermore, several FeVII lines exist in the same wavelength region as the ArX 165.53Å line, e.g., 164.955Å, 165.087Å, 165.630Å, 165.658Å, 165.724Å, 165.764Å, 165.919Å, 165.996Å and 166.010Å in addition

to the presence of CrXIX 165.45Å line. These lines are possibly blended in the ArX 165.53Å line and could make the ArX ratio smaller, since the intensity of the ArX 165.53Å is relatively weak. In the same sense for FeXVIII, the FeX 94.012Å line is very strong for iron pellet injection. The iron pellet starts ablating at plasma edge and many low ionized stage of iron ion are produced. Therefore, the ArX line blended in the ArXVIII 93.93Å and the ratio of FeXVIII has bigger error. As another candidate for the reason, the accuracy of the cross section becomes generally worse when the number of electrons forming an ion increases to 10%. However, the M1 decay rates of argon have been measured in the EBIT and experimental and calculation values are in a good agreement within accuracy of 10% [21]. Then, if the cross section has a large error, it will be the electron impact excitation.

#### 4.5. Summary

The line intensity ratios of the M1 transition to the allowed (E1) transition were measured for F-like ArX (5533Å/165Å) and Be-like ArXV (5944 Å/221Å) as a function of the electron density and results were analyzed with a simple population level calculation. As a result, the electron density dependence of the ratio was experimentally confirmed and the mechanism was well understood by the model calculation. The contribution of fast ions due to 180keV neutral beam injection to the excitation of the M1 transition was also studied for F-like ions of ArX (5533Å/165Å), TiXIV (2118Å/122Å) and FeXVIII (975 Å /94Å) using the calculation. The contribution of the fast proton impact could not be made clear in this study.

**Table 4.1** Atomic data of F I isoelectronic sequence ArX, TiXIV and FeXVIII

Ion stages	ArX	TiXIV	FeXVIII
$\lambda_{31}$ (Å)	165.53	121.986	93.93
$\lambda_{32}$ (Å)	170.63	129.440	103.95
$\lambda_{21}$ (Å)	5533	2218.15	974.85
$A_{31}$ (s <sup>-1</sup> )	$3.26 \times 10^{10}$	$6.27 \times 10^{10}$	$7.88 \times 10^{10}$
$A_{32}$ (s <sup>-1</sup> )	$1.49 \times 10^{10}$	$2.59 \times 10^{10}$	$2.91 \times 10^{10}$
$A_{21}$ (s <sup>-1</sup> )	$1.06 \times 10^2$	$1.89 \times 10^3$	$1.93 \times 10^4$
$T_e$ (eV)	376	650 <sup>a</sup>	1000 <sup>a</sup>
$C^e_{13}$ (m <sup>3</sup> s <sup>-1</sup> )	$1.10 \times 10^{-15}$	$2.27 \times 10^{-16}$	$3.21 \times 10^{-16}$
$C^e_{23}$ (m <sup>3</sup> s <sup>-1</sup> )	$1.09 \times 10^{-15}$	$2.25 \times 10^{-16}$	$3.28 \times 10^{-16}$
$C^e_{12}$ (m <sup>3</sup> s <sup>-1</sup> )	$1.38 \times 10^{-16}$	$1.45 \times 10^{-17}$	$3.13 \times 10^{-17}$
$T_i = T_p$ (eV)	557	1060 <sup>a</sup>	1700 <sup>a</sup>
$C^p_{12}$ (m <sup>3</sup> s <sup>-1</sup> )	$6.90 \times 10^{-16}$ [16]	$1.93 \times 10^{-17}$ [10]	$8.21 \times 10^{-17}$ [11]
$T_{fp}$ (keV)	100	100	100
$C^{fp}_{12}$ (m <sup>3</sup> s <sup>-1</sup> )	$4.66 \times 10^{-16}$	$1.46 \times 10^{-16}$	$2.92 \times 10^{-17}$
$S_2$ (m <sup>3</sup> s <sup>-1</sup> )	$1.70 \times 10^{-16}$	$6.89 \times 10^{-17}$	$3.45 \times 10^{-17}$
$S_3$ (m <sup>3</sup> s <sup>-1</sup> )	$1.92 \times 10^{-16}$	$7.47 \times 10^{-17}$	$3.67 \times 10^{-17}$

<sup>a</sup> extrapolation using Ar ions data.

**Table 4.2** Atomic data of Be I isoelectronic sequence ArXV

$\lambda_{51}$ (Å)	221.15	$S_2$ ( $m^3 s^{-1}$ )	$2.40 \times 10^{-17}$
$\lambda_{43}$ (Å)	5944	$S_3$ ( $m^3 s^{-1}$ )	$2.39 \times 10^{-17}$
$\lambda_{31}$ (Å)	424.01	$S_4$ ( $m^3 s^{-1}$ )	$2.42 \times 10^{-17}$
$A_{51}$ ( $s^{-1}$ )	$9.32 \times 10^9$	$S_5$ ( $m^3 s^{-1}$ )	$2.69 \times 10^{-17}$
$A_{52}$ ( $s^{-1}$ )		$5.55 \times 10^2$	
$A_{53}$ ( $s^{-1}$ )		$3.75 \times 10^2$	
$A_{54}$ ( $s^{-1}$ )		$4.93 \times 10^2$	
$A_{43}$ ( $s^{-1}$ )		62	
$A_{31}$ ( $s^{-1}$ )		$2.74 \times 10^6$ [22]	
$A_{32}$ ( $s^{-1}$ )		$7.34 \times 10^2$	
$T_e$ (eV)		646	
$C^e_{15}$ ( $m^3 s^{-1}$ )		$5.15 \times 10^{-15}$	
$C^e_{14}$ ( $m^3 s^{-1}$ )		$4.07 \times 10^{-17}$	
$C^e_{13}$ ( $m^3 s^{-1}$ )		$3.99 \times 10^{-17}$	
$C^e_{12}$ ( $m^3 s^{-1}$ )		$8.17 \times 10^{-18}$	
$C^e_{25}$ ( $m^3 s^{-1}$ )		$2.15 \times 10^{-17}$	
$C^e_{24}$ ( $m^3 s^{-1}$ )		$8.92 \times 10^{-17}$	
$C^e_{23}$ ( $m^3 s^{-1}$ )		$9.48 \times 10^{-17}$	
$C^e_{35}$ ( $m^3 s^{-1}$ )		$2.18 \times 10^{-17}$	
$C^e_{34}$ ( $m^3 s^{-1}$ )		$1.06 \times 10^{-16}$	
$C^e_{45}$ ( $m^3 s^{-1}$ )		$2.20 \times 10^{-17}$	
$T_i = T_p$ (eV)		1050	
$C^p_{24}$ ( $m^3 s^{-1}$ )		$6.15 \times 10^{-16}$ [15]	
$C^p_{23}$ ( $m^3 s^{-1}$ )		$1.51 \times 10^{-16}$ [15]	
$C^p_{34}$ ( $m^3 s^{-1}$ )		$5.27 \times 10^{-16}$ [15]	
$T_{fp}$ (keV)		100	
$C^{fp}_{24}$ ( $m^3 s^{-1}$ )		$2.03 \times 10^{-16}$	
$C^{fp}_{23}$ ( $m^3 s^{-1}$ )		$3.11 \times 10^{-17}$	
$C^{fp}_{34}$ ( $m^3 s^{-1}$ )		$1.69 \times 10^{-16}$	

## References

- [1] G. A. Doschek and U. Feldman, *J. Appl. Phys.* **47**, 3083-3087 (1976).
- [2] U. Feldman and G. A. Doschek, *J. Opt. Soc. Am.* **67**, 726-734 (1977).
- [3] M. J. Seaton, *Mon. Not. R. Astron. Soc.* **127**, 191-194 (1964).
- [4] S. Suckewer and E. Hinnov, *Phys. Rev. A* **20**, 578-585 (1979).
- [5] K. Sato, *et al.*, *Phys. Rev. Lett.* **56**, 151-154 (1986).
- [6] F. P. Keenan, *et al.*, *Phys. Lett. A.* **122**, 170-172 (1987).
- [7] K. Sato, S. Suckewer and A. Wouters, *Phys. Rev. A* **36**, 3312-3321 (1987).
- [8] F. P. Keenan and R. H. G. Reid, *J. Phys. B* **20**, L753-L757 (1987).
- [9] F. P. Keenan and R. H. G. Reid, *J. Phys. B* **22**, L295-L302 (1989).
- [10] F. P. Keenan and R. H. G. Reid, *Phys. Scr.* **39**, 314-316 (1989).
- [11] V. J. Foster, F. P. Keenan and R. H. G. Reid, *Phys. Rev. A* **49**, 3092-3095 (1994).
- [12] S. Morita and M. Goto, *Rev. Sci. Instrum.* **74**, 2375-2387 (2003).
- [13] M. F. Gu, *et al.*, *Astrophys. J.* **627**, 1066-1071 (2005).
- [14] H. L. Zhang and D. H. Sampson, *At. Data Nucl. Data Tables* **52**, 143-173 (1992).
- [15] J. G. Doyle, *At. Data Nucl. Data Tables* **37**, 441-453 (1987).
- [16] O. Bely and P. Faucher, *Astron. Astrophys.* **6**, 88-92 (1970).
- [17] V. Kaufman and J. Suger, *J. Phys. Chem. Ref. Data.* **15**, 321-387 (1986).
- [18] D. A. Verner, E. M. Verner and G. J. Ferland, *At. Data Nucl. Data Tables* **64**, 1-180 (1996).
- [19] M. B. Chowdhuri, S. Morita, M. Goto, H. Nishimura, K. Nagai and S. Fujioka, *Rev. Sci. Instrum.* to be published.
- [20] J. Z. Klose and W. L. Wiese, *J. Quant. Spectrosc. Radiat. Transfer* **42**, 337-353 (1989).
- [21] E. Träbert, *et al.*, *Astrophys. J.* **541**, 506-511 (2000).
- [22] K. T. Cheng and Y-K. Kim, *At. Data Nucl. Data tables* **24**, 111-189 (1979).

## Chapter 5

### Summary and conclusions

The magnetic forbidden dipole (M1) transitions from Al ( $Z=13$ ) to Xe ( $Z=54$ ) have been extensively studied in Large Helical Device (LHD) using visible, vacuum ultraviolet (VUV) and extreme ultraviolet (EUV) spectrometers. The wavelengths of the M1 transitions are determined with high accuracy. The intensities of the M1 transitions are analyzed with level population equation and the profiles are also examined with Doppler broadening. The main results obtained in this thesis are summarized in the following.

1. A space-resolved 3m VUV spectrometer has been developed for the observation of the M1 transitions. A space-resolved slit, an optics system with flat and cylindrical mirrors and a toroidal slit are well optimized with careful adjustment of a grating position. As a result, the space-resolved VUV spectra from carbon, neon and argon have been successfully observed.
2. In order to observe spectral emissions from heavy (high- $Z$ ) elements, which do not exist in the LHD plasma, two double-structure impurity pellets are newly designed and developed since the impurity pellet made of pure metallic heavy element terminates the discharge. One is a carbon pellet coated with the heavy element and the other is a coaxial plastic pellet inserted a heavy element fine wire into the center. These pellets, which much reduce the

amount of the heavy elements, are injected in the LHD plasma without collapse and the spectra are successfully observed from such heavy elements.

3. The M1 transitions of highly charged Al, Ar, Ti and Fe ions in visible and VUV regions have been observed. M1 lines of Al and Ar ions have been measured for the first time in magnetically confined fusion plasmas. The M1 transitions are identified with the wavelengths by measuring the Doppler broadening and the radial profile in addition to the temporal behavior. The highest resolution ( $\pm 0.02\text{\AA}$ ) is achieved by optimizing the focal image of the 3m VUV spectrometer after removing the mirror optics. Therefore, most of the observed line profiles are analyzed with the Doppler broadening. The emission lines of C, Ne and Ar observed in wavelength range of 250 to 2300 $\text{\AA}$  are carefully analyzed and the results are summarized in the table.

4. In order to measure the impurity behavior and ion temperature in the next generation fusion device with D-T burning, the M1 transitions of krypton, molybdenum and xenon are surveyed with impurity pellet injection in LHD. As a result, visible M1 transitions of KrXXIII ( $3841.07\pm 0.05\text{\AA}$ ) and MoXXIX ( $2842.10\pm 0.05\text{\AA}$ ) in silicon-like ionization stage ( $1s^2 2s^2 2p^6 3s^2 3p^2$ ) and XeXXXIII ( $4139.01\pm 0.05\text{\AA}$ ) in titanium-like ionization stage ( $1s^2 2s^2 2p^6 3s^2 3p^6 3d^4$ ) are successfully observed with high accurate wavelength. The theoretically calculated wavelengths are at present only in the accuracy of about 1%. The accuracy of these wavelengths is improved by one order magnitude as compared with the other experiments such as the electron beam ion trap (EBIT).

5. In order to study the physical process emitting M1 transition, the emission line ratio of M1 transition to E1 (allowed) transition is analyzed. It is theoretically predicted that the ratio has unique electron density dependence. However, any experimental proof has not been obtained on the ratio until now. The emission line ratio of ArX ( $5533\text{\AA}/165\text{\AA}$ ), TiXIV ( $2218\text{\AA}/122\text{\AA}$ ) and FeXVIII ( $975\text{\AA}/94\text{\AA}$ ) in fluorine-like ionization stage ( $1s^2 2s^2 2p^5$ ) and ArXV ( $5944\text{\AA}/221\text{\AA}$ ) in the beryllium-like ionization stage ( $1s^2 2s^2$ ) are adopted to examine

the density dependence of the ratio. The data are then obtained as a function of the line-averaged electron density using absolutely calibrated visible, VUV and EUV spectrometers. As a result, the M1/E1 line ratios have experimentally proved the density dependence for the first time. In order to clarify why the M1 transitions have the density dependence, the physical mechanism is analyzed using the level population equation in which three states for the fluorine-like ions and five states for the beryllium-like ions are taken into account. Excitation and de-excitation by electron impact and proton collision among fine-structure states in the ground state are included in the calculation model in addition to radiative decay. The upper level population of the M1 transition is saturated at densities above some critical density because of small transition probability of the M1 transition and the emission rate of the M1 transition becomes constant. The density dependence of the M1/E1 line ratio can be thus explained by the collisional de-excitation by the electron and the proton among the fine-structure levels of the M1 transitions. A small difference (10-50%) appears between the experiment and calculation. It possibly originates in uncertainties of the sensitivity calibration of the spectrometers and the atomic data used in the calculation.

The study of spectroscopy has developed with the progress of fusion research. According to the growth of plasma parameters in fusion plasmas the materials for plasma spectroscopy have moved to higher Z elements, especially in the plasma core. The ITER project has now started towards the D-T burning operation, where the use of high-Z elements like molybdenum or tungsten as plasma facing component and argon or krypton as diagnostic purpose is planned. The usefulness of the M1 transition will increase in such next generation fusion research, because the transition probability of the M1 transition drastically increases with increase in the nuclear number and the visible intensity becomes much bright in high-Z elements. This possibly leads to other new diagnostics in a combination of polarization spectroscopy, i.e., energetic ion measurement like  $\alpha$  particles. On the other hand, the study of atomic physics on the M1 transition is now delayed, especially the theoretical work is very few, because of the difficulty related to the interaction among spin,

orbit and nuclear charge in high-Z elements. The development of this field is really desired synchronizing with the fusion research progress.

## Acknowledgements

This doctoral thesis is completed through a study of plasma spectroscopy in the Large Helical Device (LHD) at National Institute for Fusion Science (NIFS). I am satisfied with my research life, because I have really enjoyed with this theme for three years.

In concluding my study I would like to express my sincerest gratitude to Prof. Shigeru Morita for his outstanding scientific and technical supports and supervision on the present my work. He also gave me a very nice education for these three years including educational training on experiment, presentation and paper work in addition to continuous encouragement.

I am deeply grateful to Dr. Motoshi Goto for his professional support and advice on the spectroscopy.

I also wish to express my gratitude Dr. Daiji Kato for helpful discussion and advice of the atomic physics and Dr. Atsushi Iwamae at Kyoto University for his discussion on the polarization spectroscopy. I would also like to thank Dr. Keiji Sawada at Shinsyu University for his advice, Dr. Ikuya Sakurai at Nagoya University for his support in USA trip and Mr. Chowdhuri Malay Bikas for upgrading my English conversation skill. It is a pleasure to acknowledge Dr. Chihiro Suzuki, Dr. Hiroyuki Sakaue, Dr. Izumi Murakami, Dr. Masaki Nishiura, Dr. Masahiro Kobayashi, Dr. Tsuyoshi Akiyama, Dr. Sadatsugu Muto, Prof. Kazuo Toi and Prof. Takako Kato.

Finally, I wish to express my appreciation to all members of LHD experimental group and NIFS staff for their supports and also wish to especially thank Prof. Keisuke Matsuoka and director general, Prof. Osamu Motojima for their encouragements.

## List of publications

**1. Observation of forbidden magnetic dipole transitions emitted from highly charged argon in LHD discharges**

R.Katai, S.Morita and M.Goto

Journal of Plasma and Fusion Research Series 7 (2006) 9.

**2. Radial profile measurement of impurity line emissions using space-resolved 3m vacuum ultraviolet spectrometer in LHD**

R.Katai, S.Morita and M.Goto

Review of Scientific Instruments 77 (2006) 10F307.

**3. Identification and intensity analysis on forbidden magnetic dipole emission lines of highly charged Al, Ar, Ti and Fe in LHD**

R.Katai, S.Morita and M.Goto

Journal of Quantitative Spectroscopy and Radiative Transfer (in press).

**4. High-resolution VUV spectra of carbon, neon and argon in a wavelength range of 250 to 2300Å for plasma diagnostics observed with a 3m normal incidence spectrometer in LHD**

R. Katai, S. Morita and M. Goto

Plasma and Fusion Research (in press)

**5. Development of double-structure heavy element impurity pellet for active spectroscopy of high-temperature plasmas**

R. Katai, S. Morita, M. Goto, H. Nishimura, K. Nagai and S. Fujioka  
Japanese Journal of Applied Physics (in press).

**6. Observation of visible and near-UV M1 transitions from highly charged Kr, Mo and Xe ions in LHD and its prospect to impurity spectroscopy for D-T burning plasmas**

R. Katai, S. Morita and M. Goto  
Plasma and Fusion Research (in press).

**7. Proposal of alpha particle measurement using M1/E1 line intensity ratio for D-T burning plasmas**

R. Katai, S. Morita and M. Goto  
submitted to Plasma and Fusion Research.